

ICE GENESIS

Creating the next generation of 3D simulation means for icing

Type of action: Research and Innovation Action

Call identifier: H2020-MG-2018-SingleStage

Topic: MG-2-5-2018 Innovative technologies for improving aviation safety and certification in icing conditions

Deliverable D4.3

Report on the review, assessment and selection of instrumentation/model for droplet temperature measurement

EC Grant Agreement number: 824310

Start date of project: 1 January 2019

Duration: 60 months

Lead beneficiary of this deliverable:

RV

Due date of deliverable: 31/05/2022

Actual submission date: 03/08/2022

Version #: R5.0

Project funded by the European Commission within the H2020 Programme (2014-2020)		
Type		
R	Document, report excluding the periodic and final reports	X
DEM	Demonstrator, pilot, prototype	
DEC	Websites, patents filing, press & media actions, videos, etc.	
OTHER	Software, technical diagram, etc.	
ETHICS	Ethics requirement	
ORDP	Open Research Data Pilot	
Dissemination level		
PU	PUBLIC, fully open, no embargo e.g. web	
PU*	PUBLIC after embargo of 12 months	
RE	RESTRICTED, only for certain members of the consortium (including the Commission Services): specify here which consortium members have access to the document	
CO	CONFIDENTIAL, only for members of the consortium (including the Commission Services)	X
CO+IGAB	CONFIDENTIAL, only for members of the consortium (including the Commission Services) and for the ICE GENESIS Advisory Board	

Revision History

V #	Date	Description / Reason of change	Author
1.0	12/12/2020	First Draft	Sawitree Saengkaew
2.0	23/12/2020	Input from TUBS	Venkateshwar Reddy Bora
3.0	18/01/2021	Second draft	Sawitree Saengkaew, Gerard Grehan
4.0	26/4/2021	Third draft (after revision)	Sawitree Saengkaew, Gerard Grehan
5.0	31/5/2022	Final version for release (with CIRA measurement)	Sawitree Saengkaew, Gerard Grehan

Deliverable Contributors

Authors

Organisation	Authors' name
RV	Sawitree Saengkaew, Gerard Grehan
TUBS	Venkateshwar Reddy Bora

Contributors

Organisation	Contributors' name
RV	Sawitree Saengkaew, Gerard Grehan
TUBS	Bansmer, S., Bora, V., Botelho e Souza, AC., Sattler, S.

Internal Reviewers

Organisation	Contributors' name
	Cameron Tropea
DLR	Christiane Voigt, Valerian Hahn, Mireia Papke

Table of Contents

1	Executive Summary.....	9
2	Introduction	10
3	Review on droplet temperature measurement methods	12
3.1	Inelastic techniques:	12
3.1.1	Raman spectroscopy.....	12
3.1.2	Morphological dependent resonances (MDR).....	13
3.1.3	Fluorescence/Phosphorescence:	13
3.1.4	Thermal radiation:	14
3.1.5	Thermochromism:.....	14
3.2	Elastic scattering (Rainbow Techniques):	14
3.3	Intrusive Measurements.....	16
3.4	Conclusion.....	16
4	Droplet temperature measurement by Global Rainbow Technique (GRT)	17
4.1	Rainbow from a single droplet (Rainbow Technique)	17
4.2	Rainbow from a cloud of droplets (Global Rainbow Technique, GRT)	18
4.3	Global Rainbow Instruments by RainbowVision.....	22
4.4	Sensitivity, accuracy and uncertainty of GRT in laboratory scale	25
4.4.1	Refractive index measurement accuracy.....	25
4.4.2	Water refractive index/temperature relationship.....	26
4.4.3	Temperature accuracy	29
4.4.4	Size Accuracy.....	30
4.4.5	Multi-modal Rosin-Rammler distribution	31
4.4.6	Large particle extension	33
4.4.7	GRT laboratory accuracy conclusion.....	39
5	Temperature measurement at TUBS	41
5.1	Braunschweig Icing Wind Tunnel (BIWT) Description	41
5.2	IWT measurement conditions and GRT-XL installation	42
5.3	Results overview	43
5.3.1	Temperature measurement.....	43
5.3.2	Size measurement.....	56
5.3.3	Large droplets	60
5.4	Limitation and Uncertainty of measurement in BIWT	61
5.5	Temperature Measurement in BIWT Conclusions.....	63
6	Droplet temperature Model	64
6.1	Simplified Euler-Lagrangian Model.....	64

6.2	Inverse Heat Conduction.....	64
6.3	Estimation of atomizer exit conditions with maximum entropy principle	67
6.4	Improved Euler-Lagrangian Model	70
7	Result	72
7.1	Simplified Eulerian Lagrangian Model Results.....	72
7.2	Inverse Heat Conduction Simulated Experiments	74
8	Temperature measurement inside large IWT (at RTA).....	76
9	Temperature measurement inside large IWT (at CIRA).....	79
9.1	SLD size measurement:.....	83
9.2	SLD temperature measurement	86
	Conclusions	89
	Bibliography	90

Table of Figures

Figure 1: Water/Ice Raman exemplifying spectra. a) difference between ice and water Raman spectra. b) Liquid water Raman spectra for different temperatures	12
Figure 2: Morphological dependent resonances applied to droplet characterization a) Photography and schematic representation of MDR b) Measured and computed MDR spectrum.....	13
Figure 3: A typical absorption and emission fluorescence spectrum with temperature as parameter	14
Figure 4: Light scattered by a droplet around rainbow angle a) a schematic representation of the path of the rays contributing to the first rainbow b) the light distribution around the first rainbow angle computed by using Lorenz-Mie theory for a water droplet of 100 μm	15
Figure 5: Experiment on a chain of monodispersed droplet to quantify the accuracy of rainbow techniques.....	18
<i>Figure 6: Rainbow from one individual droplet computed by using Lorenz-Mie theory.</i>	19
Figure 7: Global rainbow signal.....	21
Figure 8: Global Rainbow devices and processing software by RainbowVision	22
Figure 9: Water spray characterization by using RainbowVision SAS devices GRT-XL and GRT-Mini a) GRT temperature versus thermocouple temperature b) GRT temperature versus time c) size distribution.....	24
Figure 10: Comparison of refractive index measurement between GRT and refractometer for different liquid spray.....	25
Figure 11: Relationship between refractive index and temperature for four different liquids	26
Figure 12: Behavior of the water refractive index versus temperature at 0.6328 μm	26
Figure 13: Comparison between the predictions for positive temperatures	27
Figure 14: Relationship between refractive index values and temperature. a) Comparison between numerical prediction and experimental results at 0.532 μm for positive temperatures b) IAPWS predictions for negative temperature	28
Figure 15: Sensitivity of the refractive index versus temperature for water	29
Figure 16: The profile of water droplet temperature measurement accuracy by GRT	29
Figure 17: Comparison between PDA and GRT for size distribution measurements	30
Figure 18: Size distributions and MVD by GRT	31
Figure 19: Cumulative volumetric distribution fitting by multimodal Rosin-Rammler distributions a) Cumulative volumetric distribution fitting by a monomodal Rosin-Rammler distribution b) The extracted monomodal Rosin-Rammler distribution c) Cumulative volumetric distribution fitting by a tri-modal Rosin-Rammler distribution d) The extracted bimodal Rosin-Rammler distribution.....	32
Figure 20: The initial size distribution for 1005 droplets a) The initial size distribution in number b) The initial size distribution in volume.....	34
Figure 21: The computed global rainbow for 1005 droplets.....	34
Figure 22: Extracted size distribution for 1005 droplets a) Extracted size distribution in number b) Extracted size distribution in volume	34
Figure 23: Comparison between initial light distribution in red and recomputed light distribution in blue for 1005 droplets	35
Figure 24: The initial size distribution for 1001 droplets a) The initial size distribution in number b) The initial size distribution in volume.....	35
Figure 25: The computed global rainbow for 1001 droplets.....	36
Figure 26: Comparison between initial light distribution in red and recomputed light distribution in blue, for 1001 droplets	36

Figure 27: Extracted size distribution for 1001 droplets a) Extracted size distribution in number b) Extracted size distribution in volume	36
Figure 28: Experimental validation on a mixing of small droplets spray with big droplets a) Chain of 250 μm droplets b) Spray of 50 μm droplets c) Spray of 50 μm droplets with chain of 250 μm droplets	37
Figure 29: Two examples of sprays containing large droplets.....	38
Figure 30: Illustration of Braunschweig Icing Wind Tunnel facility	41
Figure 31: GRT-XL probe in the test section of the Braunschweig Icing Wind Tunnel	42
Figure 32: Measured droplet temperature versus the air temperature	43
Figure 33: The difference of temperature between the droplet and the wind tunnel air versus the droplet diameter.....	44
Figure 34: The measured droplet temperature versus the measured droplet MVD, the parameter is the wind tunnel temperature	44
Figure 35: Compilation of droplet temperature measurement for different test conditions (air speed 40 m/s).....	45
Figure 36: Droplet temperature measurement at $T_{\text{air}} = -10\text{ }^{\circ}\text{C}$ and $V = 40\text{ m/s}$ a) Temporal evolution of the measured droplet temperature b) Statistical representation of the measured droplet temperature	47
Figure 37: Long duration droplet temperature measurement at $T_{\text{air}} = -10\text{ }^{\circ}\text{C}$ and $V = 40\text{ m/s}$ a) Temporal evolution of the measured droplet temperature b) Statistical representation of the measured droplet temperature.....	48
Figure 38: Droplet temperature measurement at $T_{\text{air}} = -15\text{ }^{\circ}\text{C}$ and $V = 40\text{ m/s}$ a) Temporal evolution of the measured droplet temperature b) Statistical representation of the measured droplet temperature	50
Figure 39: Droplet temperature measurements in IWT at $-15\text{ }^{\circ}\text{C}$ and 30 m/s , a) Temporal temperature evolution b) Statistical representation	51
Figure 40: Droplet temperature measurement in IWT at $-15\text{ }^{\circ}\text{C}$ and 20 m/s , a) Temporal temperature evolution b) Statistical representation	51
Figure 41: Droplet temperature sensitivity to the air velocity for droplet size of 20 and 60 μm a) Temporal evolution of the measured droplet temperature b) Statistical representation c) Temporal evolution of the measured droplet temperature d) Statistical representation	52
Figure 42: Droplet temperature sensitivity to the liquid water content (LWC) for droplet size of 20 and 40 μm at air velocity 40 m/s a) For 20 microns b) For 40 microns	53
Figure 43: Droplet temperature measurement at $T_{\text{air}} = -20\text{ }^{\circ}\text{C}$ and $V = 40\text{ m/s}$ a) Temporal evolution of droplet temperature at $-20\text{ }^{\circ}\text{C}$ b) Statistical representation of the measured droplet temperature at $-20\text{ }^{\circ}\text{C}$	55
Figure 44: An example of size distribution measurement.....	57
Figure 45: Measured MVD versus ordered diameter	57
Figure 46: The measured droplet temperature versus the measured MVD	58
Figure 47: The Rosin-Rammler analysis of the size distribution	59
Figure 48: Droplet temperature measurement for droplet MVD larger than 100 μm a) Temporal evolution of temperature for large droplets at $-20\text{ }^{\circ}\text{C}$, b) Statistical droplet temperature evolution at $-20\text{ }^{\circ}\text{C}$	60
Figure 49: Series of images displaying the change of direction of the laser beam due to a water/ice film	61
Figure 50: Examples of a measurement result perturbed by an ice deposition on the inside face of the window	62
Figure 51: Schematic of setup for impingement heat transfer estimate	65

Figure 52: Schematic of control volume around the atomizer	68
Figure 53: Influence of droplet injection velocity	72
Figure 54: Droplet Temperature for tunnel conditions 40m/s at -20°C	73
Figure 55: Improvement in droplet temperature by shifting spray bar upstream	73
Figure 56: Inverse Heat Conduction applied to case-1	74
Figure 57: Heat Flux estimation with transient profiles	75
Figure 58: GRT-Mini Installation in RTA's IWT a) Before run the measurement b) After run the measurement.....	76
Figure 59: Illustration of fog on the collecting lens	77
Figure 60: Examples of rejected signals at RTA a) Droplet on the emission window b) Fog on the collecting window c) Scattering diagram including at least one highly deformed droplet	77
Figure 61: Example of validated measurement at RTA (for air temperature = -5°C, air velocity = 60 m/s and LWC = 0.65 g/m ³) a) Recorded image b) Associated measured size distribution and temperature	78
Figure 62: GRT-Mini inside CIRA facility	79
Figure 63: Example of a global rainbow image with the associated angular light distribution for a spray created by an ultrasonic nozzle.	79
Figure 64: GRT-Mini after run the experiment	80
Figure 65: Examples of recorded rainbow images.....	82
Figure 66: Some examples of images and processing to extract SLD size.	84
Figure 67: The measured diameter from 'individual droplet' versus the image number	85
Figure 68: Visual representation of the numerical global rainbow construction from selected individual images.....	86
Figure 69: Comparison between the global rainbow directly obtained from a large number of droplet (left) and the numerically reconstructed global rainbow obtained from individual droplets.....	87
Figure 70: SLD characterization by GRT: (a) Average droplet temperature and (b) Average droplet diameter.....	88

Glossary

Abbreviation / Acronym	Description/meaning
CS25	Certification Specification
FAR25	Federal Aviation Regulation
FZDZ	Freezing Drizzle
FZRA	Freezing Rain
GRT	Global Rainbow Technique
IRT	Infrared Thermography
IWT	Icing Wind Tunnel
LWC	Liquid Water Content [g/m ³]
MVD	Median Volume Diameter (μm)
n	Refractive index
Nu	Nusselt number
PDF	Probability Density Function
Re	Reynolds number
RTA	Rail Tec Arsenal
Sc	Schmidt number
SLD	Supercooled Large Droplets
Sh	Sherwood number
TWC	Total Water Content [g/m ³]
T _{air}	Air temperature in wind tunnel (°C)
T _{measured}	Measured droplet temperature by Global Rainbow Technique (°C)
T _{water}	Temperature of water in reservoir (°C)
V	Air velocity in wind tunnel (m/s)
W/T	Wind tunnel
WP	Work Package

1 Executive Summary

Droplet temperature is one of the critical parameters which determine ice accretion on aircraft components. Recreating natural icing conditions in a wind tunnel still pose a challenge. A major difficulty is the determination of the water droplet temperature. Unlike naturally formed liquid droplets in the troposphere, where the droplet temperature can be assumed to be equal to the surrounding air temperature, the water injection in icing wind tunnels demands positive temperatures, limiting the residence time and thus the heat exchange with ambient air in the free flow. Therefore, in-situ measurements of droplets temperature and size distribution is crucial for characterization of conditions in the tunnel.

The aim of task 4.3 in WP4 is to evaluate droplet temperature measurements by using the Global Rainbow Technique (GRT) in Icing Wind Tunnel (IWT) as well as to simulate the droplet temperature behavior during its short resident time. GRT is a non-intrusive technique based on the analysis of the light scattered by droplets around the rainbow angle. By using a rigorous theory, the average droplet temperature and size distribution can be extracted simultaneously. According to the IWT dimension, GRT-XL is developed to measure from outside of small IWT while GRT-Mini is developed to measure directly inside large IWT. A simulation code has been developed to quantify the effect of few large droplets in a cloud of smallest one on the temperature and size measurement, especially when the large and small droplet are at different temperature.

This report describes the first droplet temperature measurements carried out a small IWT at the Technical University of Braunschweig (TUBS) for small and large droplets, under Appendix C conditions. Additionally, the preliminary computational work carried out at TU Braunschweig to estimate the droplet temperature in the icing wind tunnel will be summarized in this report. The influence of the injection temperature, injection velocity and spray bar axial position are studied, to estimate droplet velocities and temperatures for different size distributions for supercooled droplets in the IWT test section. Furthermore, the preliminary temperature measurements of large droplets under FZDZ conditions inside RTA's large IWT are evaluated.

Over the course of one week, the droplet temperatures have been successfully measured in the icing wind tunnel at TUBS. Real time measurements have been realized under adjustment of IWT settings in order to vary spray parameters such as: MVD, LWC, air temperature and velocity. The results show that the droplet temperature is a complex function of all these parameters. The measurements have been essentially focused on droplets with a MVD between 20 μm and 60 μm , permitting comparisons with numerical simulations. Moreover, some measurements have been carried out for SLD with MVD larger than 100 μm .

FZDZ studies, which have been performed during a two-day measurement period at RTA, IWT (Vienna, Austria) have been strongly perturbed by water condensation on the GRT recording lens. Nevertheless, measurements have been successfully carried out for one case.

These results demonstrate that droplet temperature measurements under application of GRT in IWTs are possible, showing that the main limitations are mainly related to technical issues due to water/ice deposition on the optical surface. To remove these difficulties, dedicated accessories have to be used to locally ventilate and warm the optical surfaces. An upgrade to the instrument might involve a heated optical inlet and the application of a covering sheath-flow above the optics, in order to prevent and remove any deposition. Adjustments to the proposed instrument accessories have to be tested for the employed test environments in each wind tunnel, specifically.

2 Introduction

The ICE GENESIS project objective is to provide the European aeronautical industry with a validated new generation of 3D icing numerical tools and test capabilities. Special attention is drawn to the new icing conditions described in Appendix-O SLD conditions. The Appendix-O of EASA CS 25 [1] describes the supercooled large droplet icing conditions consisting of freezing drizzle (FZDZ) and freezing rain (FZRA) occurring in and/or below stratiform clouds. The FZDZ and FZRA clouds contain a wide spectra and distribution of droplets, therefore they are further classified into two classes based on a MVD less than or greater than 40 μm . The FZDZ with $\text{MVD} < 40$ includes droplets as large as 388 μm and FZRA with $\text{MVD} > 40$ contains droplets as large as 2280 μm .

In Icing Wind Tunnels (IWT), these large droplets will not be in thermal equilibrium with the air. The measurement of the droplet temperature is crucial for experimental studies in icing wind tunnels as well as for the validation of numerical icing simulations. Due to the long period of time water droplets in the troposphere remain under ambient conditions, their temperature is assumed to be the same as of the ambient air. Water droplets in IWT facilities however are injected into the tunnel at positive water temperatures not allowing the necessary time to reach a thermal equilibrium with the ambient air temperature in the tunnel. Therefore, the measurement of droplet temperatures in an IWT proves to be a challenge.

The aim of task 4.3 in WP4 is to evaluate the droplet temperature measurement using the Global Rainbow Technique (GRT) in Icing Wind Tunnels (IWT), as well as to simulate the droplet temperature behavior.

The measurement device is provided by *RainbowVision S.A.S* to measure the temperature of supercooled water droplets inside IWT. In these studies, various parameters such as droplet size, air temperature, flow velocity, Liquid Water Content (LWC) and liquid water temperature before atomization are being varied. The measurements in a small IWT have been carried out at the experimental IWT at TUBS, whereas the measurements in a large IWT have been conducted at the commercially used RTA facility.

Besides the measurement of droplet temperatures, the development of a numerical droplet temperature simulation code at TUBS is accompanying the measurement activities. A series of numerical simulations are being developed using a decoupled Eulerian-Lagrangian approach, assuming that a droplet has an uniform temperature and experiences no evaporation at its surface, since the relative humidity in the tunnel is above 90%. In a Lagrangian approach, particle trajectories and properties are obtained from the integration of the initial conditions, thus successful comparisons of GRT and the numerical results are based on the quality of the spray conditions specified as input for the Lagrangian solver. The unsteadiness and complex physics of the spray are not very well understood; rendering a deterministic modelling of the nozzle exit conditions as impossible. Therefore, a maximum entropy principle is employed to generate a joint probability density function of the spray in terms of velocity, size and temperature from the available nozzle operating conditions. The joint pdf serves as an input to the Lagrangian solver to obtain conditions at the test section. Furthermore, to validate the maximum entropy principle, experiments with a spray impingement on a hot plate are planned. An inverse heat transfer code is being developed to retrieve the heat flux resulting from a spray wetting a test plate, by means of a measuring the plate's temperature change. Simulated experiments are successful in retrieving discontinuous heat flux in space and time resulting from the spray impingement.

The present document provides a comprehensive overview of the results obtained during the first 24 months of the ICE GENESIS program in Task 4.3. The report is organized as follows:

- A review of droplet temperature measurement techniques
- Measurement of temperature using the Global Rainbow Technique (GRT)
- Temperature measurements in a small IWT (TUBS)
- Numerical simulation of droplet behavior
- Temperature measurements in a large IWT (RTA)
- Temperature measurements in a large IWT (CIRA)

3 Review on droplet temperature measurement methods

Sprays have extensive applications in a wide domain of industrial activities, including spray drying in food and pharmaceutical activities or the mixing of liquid fuel in combustion systems. In the aeronautics industry, sprays are essential for the development of performant propulsors as well as to understand the icing process and develop de-icing technology for aircraft.

The droplets of a spray interact with the surrounding medium, creating complex heat and mass transfer processes which include heating, cooling, condensation, evaporation, freezing, etc.,. In order to gain a comprehensive understanding of the droplet dynamics, measurements of the transient droplet properties such as size and temperature, as well as their changes during these dynamic processes are essential.

Accordingly, to be able to measure these properties non-intrusively, a large range of optical methods have been proposed.

For the measurement of the geometrical properties of sprays as droplet size and velocity the following approaches and devices are used:

- Direct imaging for size measurement: photography, holography
- Devices based on light diffraction and interferometry, such as: diffractometry, Phase Doppler Analyzer (PDA), Interferometric Particle Imaging (IPI).

A large number of these techniques are commercially available.

To measure the temperature of droplets several approaches are just under development, based on different physical concepts, basically using the principles of non-elastic and elastic scattering. However, no commercial devices are available, yet.

3.1 Inelastic techniques:

In inelastic light scattering, the information on the temperature is coded by the frequency (wavelength) of the emitted light by the droplets. The following techniques are based on non-elastic techniques:

3.1.1 Raman spectroscopy

Raman is a non-destructive, non-intrusive optical technique based on the detection of photons emitted inelastically following the interaction of the sample with a monochromatic laser beam. The difference in frequency between incident photons and emitted photons encodes information about the chemical nature of the molecule that caused the emission, in terms of composition and temperature.

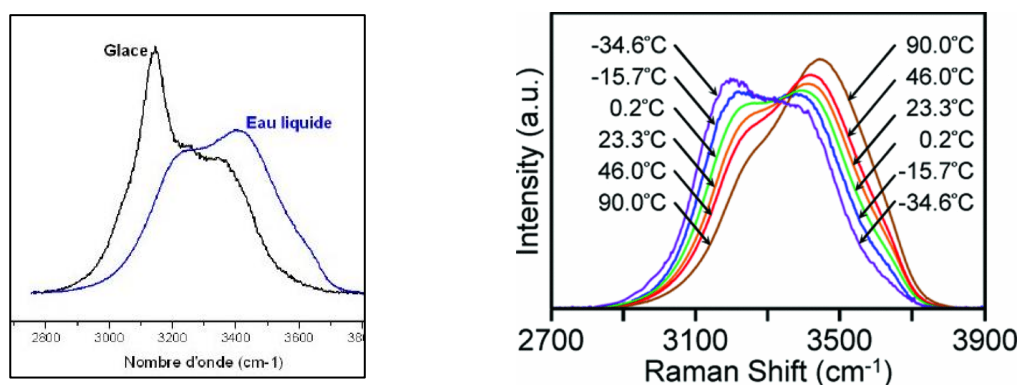


Figure 1: Water/Ice Raman exemplifying spectra. a) difference between ice and water Raman spectra. b) Liquid water Raman spectra for different temperatures

This technique has been used on levitated supercooled water droplets [2] [3] and on sprays at lab scale [4].

3.1.2 Morphological dependent resonances (MDR).

Resonances can be found in certain types of optical cavities that are cylindrical, spherical, and ellipsoidal in shape. Conditions under which the resonances occur depend on shape as well as refractive index of material within the optical cavity, and is normally characterized by the two integers order number and mode number.

MDR have been used to characterize droplet chains, single droplets as well as droplets in sprays [5].

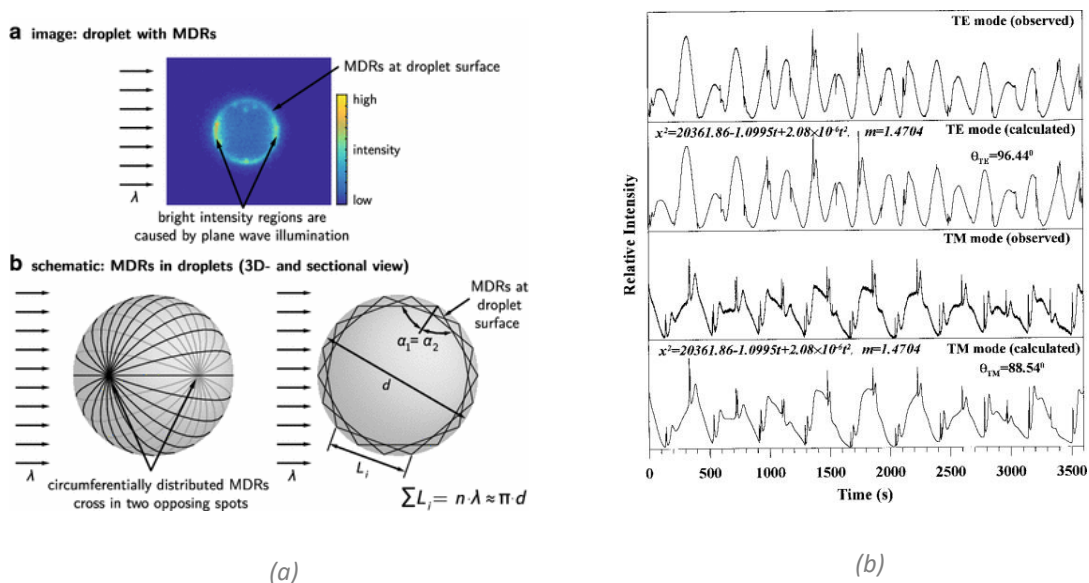


Figure 2: Morphological dependent resonances applied to droplet characterization a) Photography and schematic representation of MDR b) Measured and computed MDR spectrum.

3.1.3 Fluorescence/Phosphorescence:

Fluorescence is the emission of light by a substance that has absorbed light or other electromagnetic radiation. Phosphorescence is a type of photoluminescence related to fluorescence. Unlike fluorescence, a phosphorescent material does not immediately re-emit the radiation it absorbs. In both cases, the emitted light is at a longer wavelength than the incident light. Fluorescence and phosphorescence have been used to obtain information on droplet temperature. Different strategies combining different dyes, different emitted wavelengths as well as collection of the light at different wavelengths have been developed [6]. Recently, it has been demonstrated the possibility to distinguish between ice and water in drop by using fluorescence [7] [8].

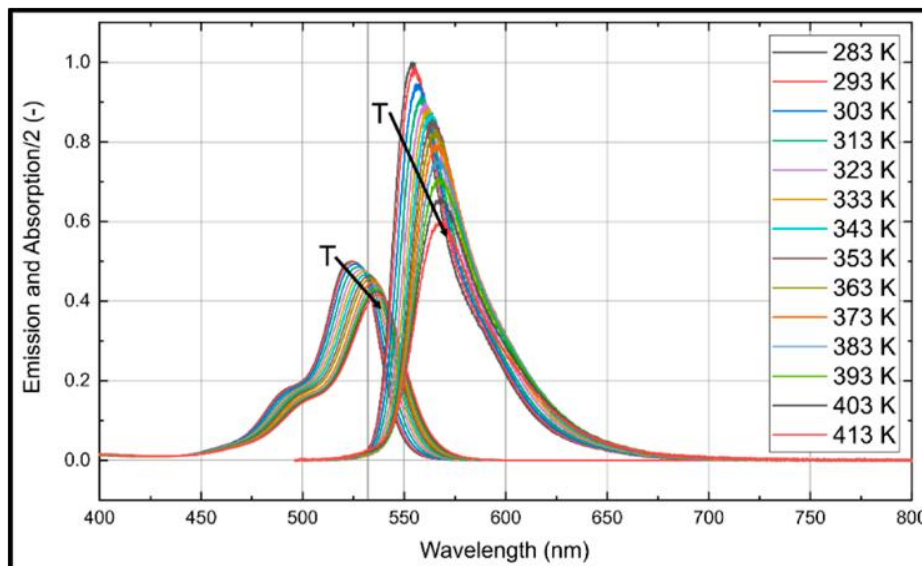


Figure 3: A typical absorption and emission fluorescence spectrum with temperature as parameter

3.1.4 Thermal radiation:

Planck's law describes the spectral density of electromagnetic radiation emitted by a black body in thermal equilibrium at a given temperature T , when there is no net flow of matter or energy between the body and its environment. That radiation can be collected and analyzed by using an infrared camera to extract information on the temperature of a spray [9] [10].

3.1.5 Thermochromism:

Thermochromism is the property of individual substances to change their color upon heating or cooling. Thermochromic particles can be added in the droplets to obtain information on their temperature [11].

3.2 Elastic scattering (Rainbow Techniques):

Light incidence on a spherical droplet is scattered in space, according to the Lorenz-Mie theory. The scattering phase function is a complex function depending on the droplet size, the droplet refractive index and the incident wavelength.

Among the different possible elastic scattering measurement strategies, a particularly interesting configuration is based on the analysis of the light scattered around the rainbow angle. The rainbow angular location of a certain wavelength is a function of the refractive index and therefore also a function of the droplet temperature. Accordingly, the evaluation of light scattered around the rainbow angle ($\sim 138^\circ$, for water) enables a measurement of the droplet temperature. Moreover, the shape of the light scattered around the rainbow angle depends on the droplet size. Therefore, by analyzing the light scattered around the rainbow angle, both the temperature and size of the droplets are simultaneously measured.

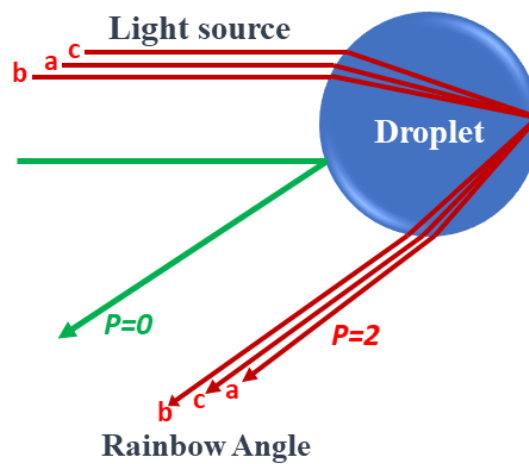
Using this principle, different configurations have been developed:

Rainbow technique: very accurate but very sensitive to any departure from perfect sphericity

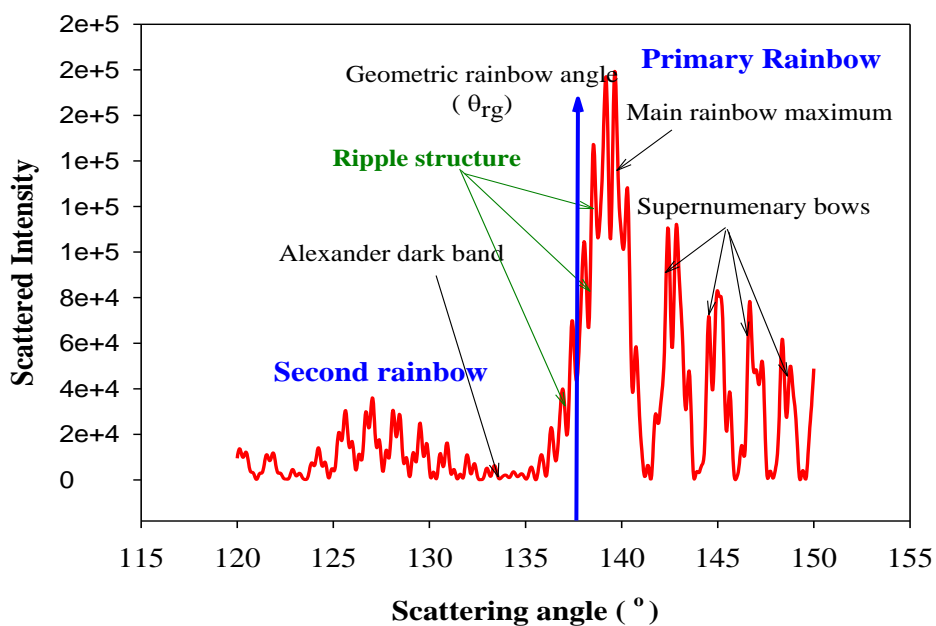
- Measurement of individual droplets with pulsed laser light
- Measurement of monodispersed droplet chain with continuous laser light

Global rainbow technique: less sensitive to sphericity, but yields averaged information over an ensemble of droplets

- Measurement in spray with continuous laser light



a)



b)

Figure 4: Light scattered by a droplet around rainbow angle a) a schematic representation of the path of the rays contributing to the first rainbow b) the light distribution around the first rainbow angle computed by using Lorenz-Mie theory for a water droplet of 100 μm .

3.3 Intrusive Measurements

While the previous measurement principles are non-intrusive, measurement with thermoelectric sondes such as Type T, J, E and K thermocouples which are reliable sensors in the low temperature range with a high response rate in the temperature range of interest are intrusive. Measurements that are more accurate can be obtained by resistance thermal devices; however, they have a relatively slow response compared to thermocouples.

These techniques are of limited relevance for this application of measuring droplet temperature of spray in IWT and hence are not elaborated further in detail.

3.4 Conclusion

Table 1 summarize the advantages and limitation of the droplet temperature measurement techniques discussed before.

Principle	Laser power	Recording device	Pure water	Intrusive
MDR	very high	Spectroscopy	yes	no
Fluorescence/phophorescence	high	PM/diode/filters	requires additives	yes
Thermochromic	N/A	Camera	requires additives	yes
Infrared radiation	N/A	IR camera	yes	no
Raman	very high	Spectroscopy	yes	no
Elastic scattering/ (Rainbow/Global Rainbow)	low	Camera	yes	no

Table 1: Main characteristics of the different techniques for measuring droplet temperature.

In the Ice-Genesis project, the global rainbow technique has been selected to measure the average droplet temperature in Icing Wind Tunnels. The advantages of the global rainbow techniques are:

1. Non-intrusive technique
2. Accurate measurement
3. Can be used over wide range of temperature and pressure
4. No need for additives in the liquid under study

However, when applied to water droplets the following difficulties must be underlined:

1. The low sensitivity of the refractive index with the temperature
2. Ambiguity in the curve refractive index / temperature, which exhibits an extremum at about 0°C (non-monotonic relation)
3. Sensitivity to the shape for large droplets

4 Droplet temperature measurement by Global Rainbow Technique (GRT)

A rainbow is a very well-known natural phenomenon characterized by a very colored and bright diffusion of the sunlight by rain water droplets. The explanation of the rainbow has been at the origin of legends. Later the scientific explanation of the rainbow has followed the progress in mathematics and physics (Maxwell's equations, geometrical optics, diffraction theory, etc.). Nowadays, by using the Maxwell's equations, the rainbow characteristics can be rigorously computed using the Lorenz-Mie theory. The high sensitivity of the rainbow to the droplet refractive index value and size is very attractive to develop measurement techniques.

4.1 Rainbow from a single droplet (Rainbow Technique)

For a single droplet, the rainbow is created by the fact that an extremum of deviation exists for rays experiencing internal reflection(s) at the curved droplet interface with the surrounding medium. The main rainbow, or first order rainbow, is created by rays undergoing one internal reflection inside the droplet, a secondary rainbow is created by rays after two internal reflections, and so on.

Accordingly, the absolute angular location of the rainbow depends primarily on the refractive index of the droplet, while the rainbow shape depends primarily on the droplet size. Figure 4 displays the rainbow for one water droplet with a diameter of 100 μm on which impinges a laser beam at a wavelength of 0.532 μm . In 4(b), the continuous vertical blue line represents the geometrical rainbow location. The light scattered between 135° and 150° represents the main rainbow while the secondary rainbow is located between 120° and 132°.

The scattering diagram in figure 4 can be explained as follows:

- The primary rainbow location is defined by the extremum of deviation of 'rays' with one internal reflection ($p=2$)
- The second rainbow, displayed in (b), is defined by the extremum of deviation of 'rays' with two internal reflections ($p=3$)
- The low frequency oscillations are created by interference between rays of the same kind (rays with one internal reflection ($p=2$) for the primary rainbow, rays with two internal ($p=3$) reflections for the second rainbow).
- The high frequency oscillations, called ripple structure, are created:
 - For the main rainbow, by interference between rays with one internal reflection ($p=2$) with all the other kind of rays (externally reflected ($p=0$), x times internally reflected, MDR, ..)
 - For the second rainbow, by interference between rays with two internal reflections ($p=3$) with all the other kind of rays.

The analysis of the rainbow patterns created by a single droplet, including the ripple structure, provides the possibility to measure the droplet refractive index and therefore its temperature and droplet size with a very high accuracy [12]. However, this approach is extremely sensitive to any deviation from perfect sphericity.

In practice, experiments on one single droplet are very rare and are extremely difficult to perform. The solution is to experimentally work on a continuous chain of identical droplets and use the one droplet theory to process the experimentally recorded scattering diagrams.

Such configurations (as shown in Figure 5) permit to reach an accuracy of 0.01 μm on the droplet diameter with an accuracy on the fourth digit for the refractive index (about 1°C for ethanol). This approach has been extensively used to study the evaporation of droplets [12] [13] [14] and the effect

of non-sphericity [15] [16], to quantify composition gradients in the case of CO₂ capture by a MEA spray [17] [18], i.e., the behaviour of ethane droplet at the vicinity of critical pressure [19].

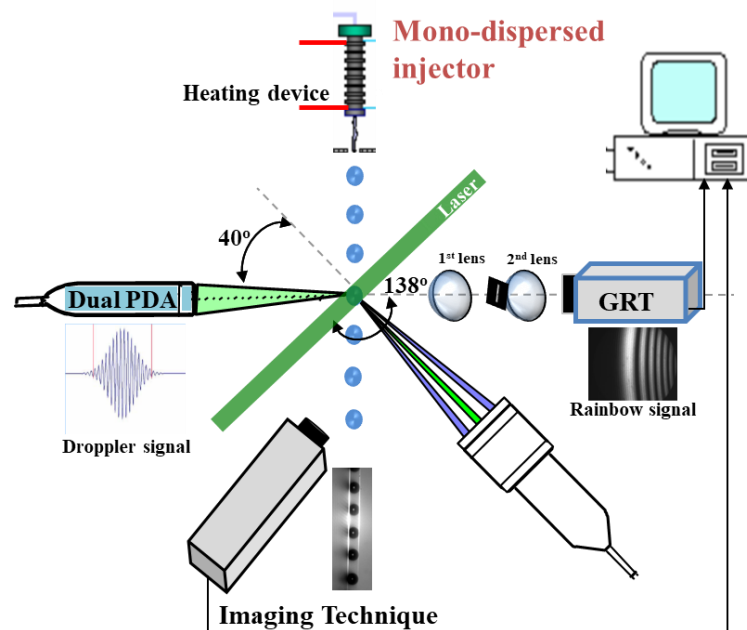
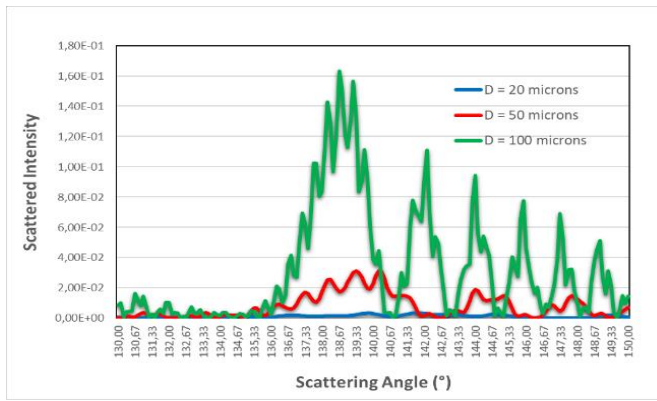


Figure 5: Experiment on a chain of monodispersed droplet to quantify the accuracy of rainbow techniques

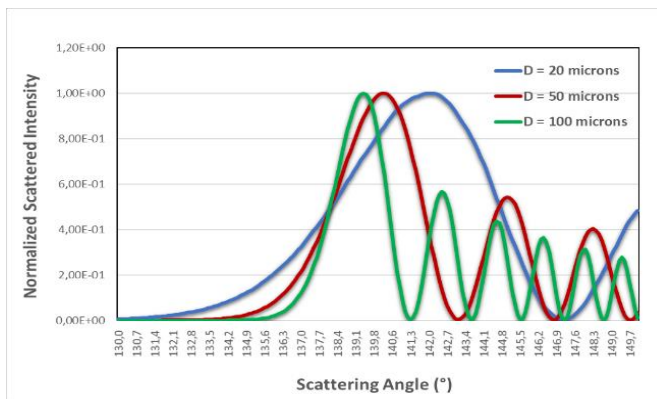
4.2 Rainbow from a cloud of droplets (Global Rainbow Technique, GRT)

To be able to apply the rainbow technique in realistic sprays, the rainbow technique has been further developed to the Global Rainbow Technique (GRT) [20]. This technique is based on the recording and analysis of the synthetic rainbow created by a large number of droplets with different sizes, orientations and locations for a sufficient long exposure time. It has been demonstrated that GRT is less sensitive to the droplet shape than the single rainbow technique.

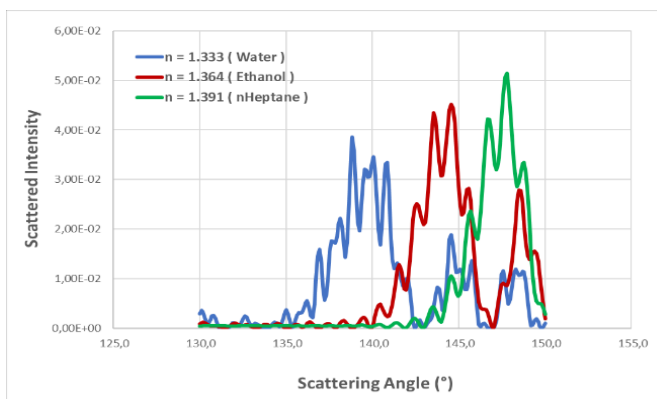
Figure 6(a) compares three rainbow signals, computed using the rigorous Lorenz-Mie theory, for three individual droplet sizes with constant refractive index of 1.333. The dependence of the signal intensity with the droplet size is underlined. Moreover, the signal shape depends also on the droplet size. This is evidenced in Figure 6(b), which displays the normalized scattered intensity for only the rays with one internal reflection ($p=2$). The three rainbows intersect at the same angular emission angle, which is the geometrical optics rainbow angle having the same refractive index value. When the droplets have different refractive index values, the rainbow angles are shifted, as illustrated in figure 6(c). For water, the variation of the refractive index with temperature is low. Consequently, the shift of the rainbow angular position with the temperature will be small, as displayed in figure 6(d). Nevertheless, the ripple structure complicates the analysis by obscuring the angular displacement due to the change of the refractive index.



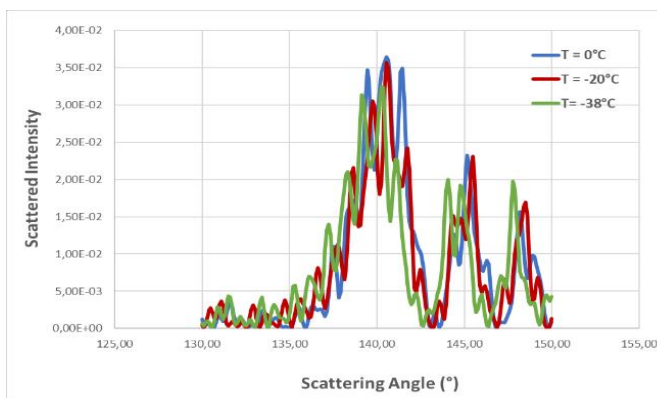
a) Comparison of individual rainbow signals between three different droplet sizes



b) Comparison of normalized scattering diagram for three different droplet sizes (computed from only the one time internally reflected rays, $p=2$)



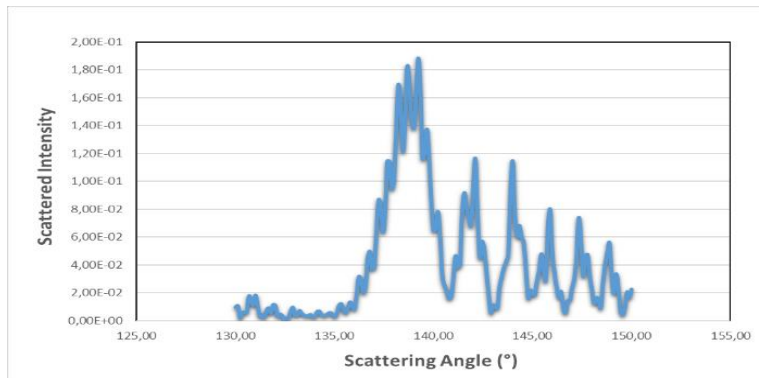
c) Comparison of individual rainbow signals between three different liquids



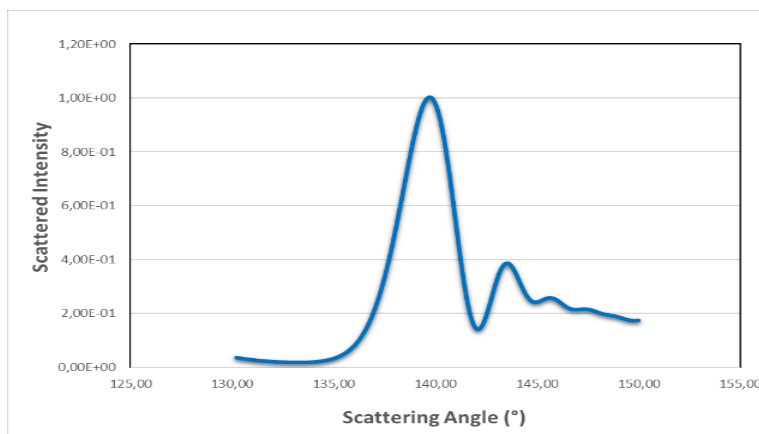
d) Comparison of individual rainbow signals for a water droplet at three different temperatures

Figure 6: Rainbow from one individual droplet computed by using Lorenz-Mie theory.

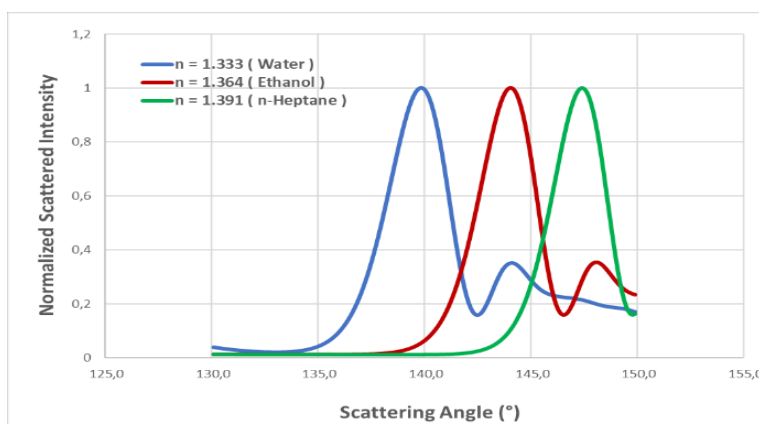
To reduce the influence of the ripple structure, the light scattered from an ensemble of droplets can be summed up, creating a global rainbow signal. Figure 7 illustrates the creation of a global rainbow signal. Figure 7(a) is the global rainbow signal obtained by considering only three particles. In this case, the ripple structure is modified but still existing. The ripple structures will completely disappear when a large number of droplets contribute to the signal as displayed in figure 7(b), where they are smoothed due to the summation of a large number of different rainbows. Moreover, such a global rainbow signal is less sensitive to the shape of the droplet. As for the rainbow signal, its absolute angular position is a measure of the average refractive index value, therefore average temperature, while its shape is a measure of the size distribution shown in figure 7(c) and 7(d) respectively.



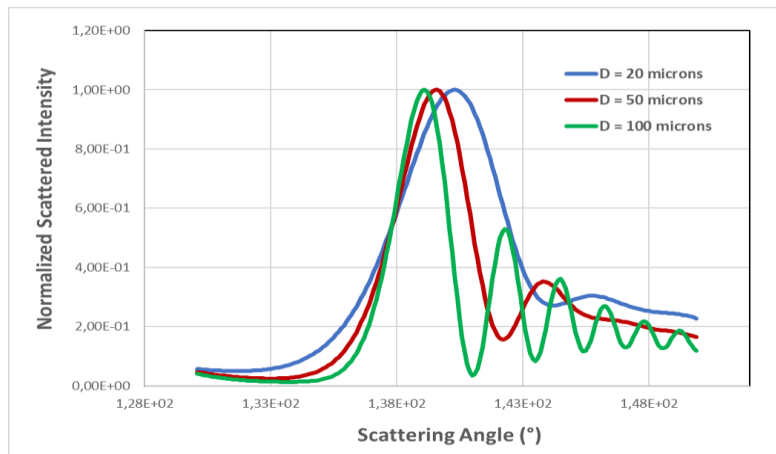
a) *The global rainbow created by three droplets from figure 6(a)*



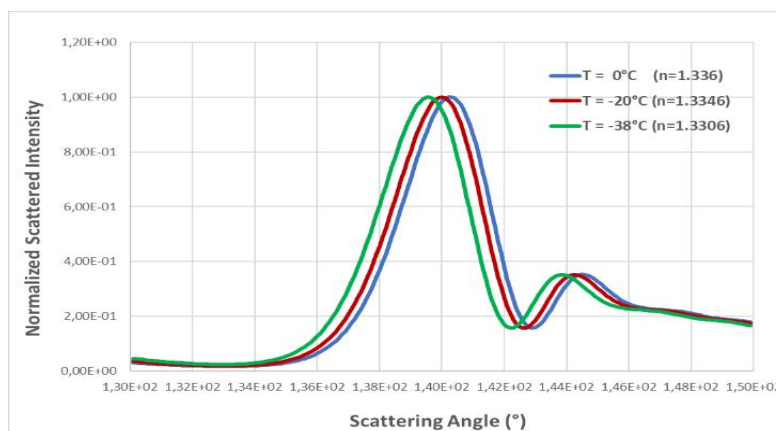
b) *A typical GRT created by a continuous size distribution*



c) *Comparison of global rainbow signals between three different liquids*



d) Comparison of global rainbow signal for three different size distributions ($n=1.333$)



e) Comparison of global rainbow signals for water at three different temperatures

Figure 7: Global rainbow signal

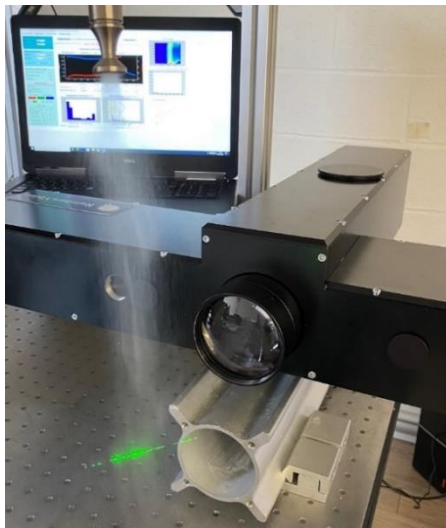
When studying supercooled water droplets, as the sensitivity of the refractive index with temperature is small, the global rainbow signal angular shift will also be small as displayed in 7(e). Then an accurate measurement is desired.

The efficient processing of global rainbow signals implies the need to calculate a large number of single rainbow signal accurately and as quickly as possible. To reach this objective, it has been demonstrated that the Nussenzveig's theory is a suitable solution [21] [22] [23] [24]. For water droplets, Nussenzveig's theory is nearly as accurate as the Lorenz-Mie's theory, but as fast as Airy's theory [22] [24]. Moreover, the Lorenz-Mie theory is highly non-linear and Nussenzveig's theory is linear. The linearity of the Nussenzveig theory is a necessary condition to develop fast and accurate inversion schemes [25].

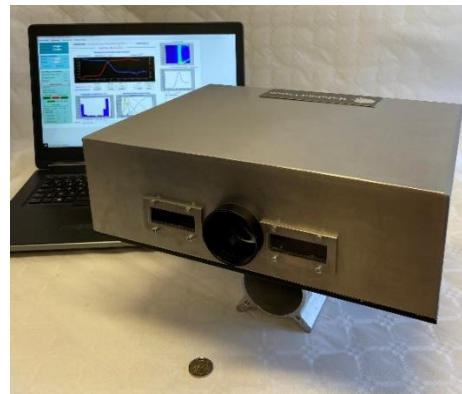
4.3 Global Rainbow Instruments by RainbowVision

Initially, *RainbowVision SAS* devices have been developed and optimised to study fuel evaporation in combustion systems [13] [14] [17] [18] [26]. This promising technique is applied for the first time to study icing in IWT within the scope of the ICE-Genesis project. The measurement of the water droplets temperature for icing characterization is similar to the measurement of the fuel droplet temperature in combustion processes. Nevertheless, special attention will be devoted to the singularities of the water properties. As the GRT measures the droplet temperature via its refractive index value, the low dependence of the refractive index of water with the temperature and its non-linearity must be taken into account. Accordingly, to reach the same temperature accuracy on water droplets as for fuel droplets, the accuracy of the measured refractive index value of water must be to the fourth decimal, that is to say about 10 times better than for combustion studies.

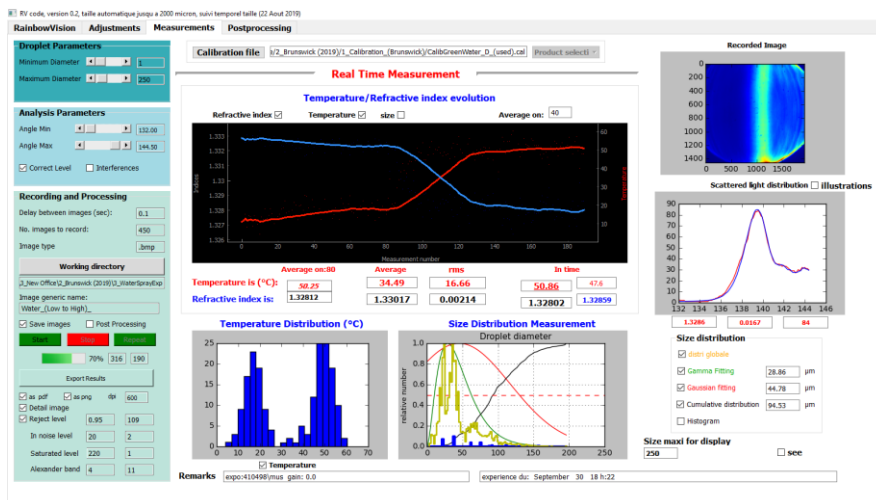
RainbowVision (SAS) provides two mobile GRT instruments to measure water droplet temperature. A first model, called GRT-XL in figure 8 (a), has been designed to measure the droplets from outside of a wind tunnel, through an optical window. A second model, called GRT-mini in figure 8(b), has been designed to measure the droplets directly inside a wind tunnel.



a) GRT-XL Model



b) GRT-Mini Model



c) Real time signal processing code

Figure 8: Global Rainbow devices and processing software by RainbowVision

To be able to efficiently characterize water sprays in terms of temperature and size inside an IWT, both hardware and inversion software have been upgraded to take into account:

- Low LWC condition (from 3 g/m³ down to 0.1 g/m³)
- The possibility to have a signal with few droplets at low LWC
- The importance of few big droplets in terms of mass
- The extremely large domain of the droplet size range for icing studies
- The singular behavior of the dependence of water refractive index with temperature
- The capability of measuring a multi-modal-size distribution

Therefore, the GRT-XL and GRT-Mini instruments feature:

1. System mobility
2. Real-time measurement
3. Non-intrusive technique
4. Usable over a large range of temperature and pressure environments
5. Additive free
6. Able to measure at low LWC under low laser light intensity

The automatic signal processing software has been written to extract both the average refractive index and therefore the average droplet temperature and the size distribution from light scattered around rainbow angle. The inversion code is based on extensive computations of rainbows in the framework of Nussenzweig's theory, combined with Non-Negative Least Square (NNLS) approach [27] and curve minimization, permitting an accurately real time measurement of the spray characteristics. The same software is used for both GRT devices.

To evaluate the accuracy of the developed devices, a series of experiments has been carried out in the laboratory on gravitationally sedimenting droplet clouds. Quasi-monodispersed sprays have been created by using ultrasonic droplet generators. Droplets within the so generated sprays, with a MVD of about 80 microns, traversed the instruments' optics at a terminal velocity of about 2 m/sec.

In these series of experiments, the temperature of the droplets has been measured using GRT-XL and GRT-Mini and simultaneously been compared with thermocouple temperature measurements.

The results are shown in figure 9. Figure 9 (a) displays the temperature measured by GRT versus the temperature measured by thermocouple between 10°C and 60°C. The agreement between GRT and the thermocouple measurement is good for both GRT devices. Moreover, it can be underlined that the temperature measurement dispersion by GRT is about 5-10 times smaller than by thermocouple. Figure 9 (b) represents the continuous measurement in time of the spray temperature evolution. In the liquid reservoir at room temperature, hot water has been added, allowing measurements of the droplet heating up in real time. These results demonstrate that both the GRT-XL and the GRT-Mini devices yield similar results and are able to quantify the water droplet temperature evolution.

The next point is to quantify the accuracy and sensitivity of the GRT devices.

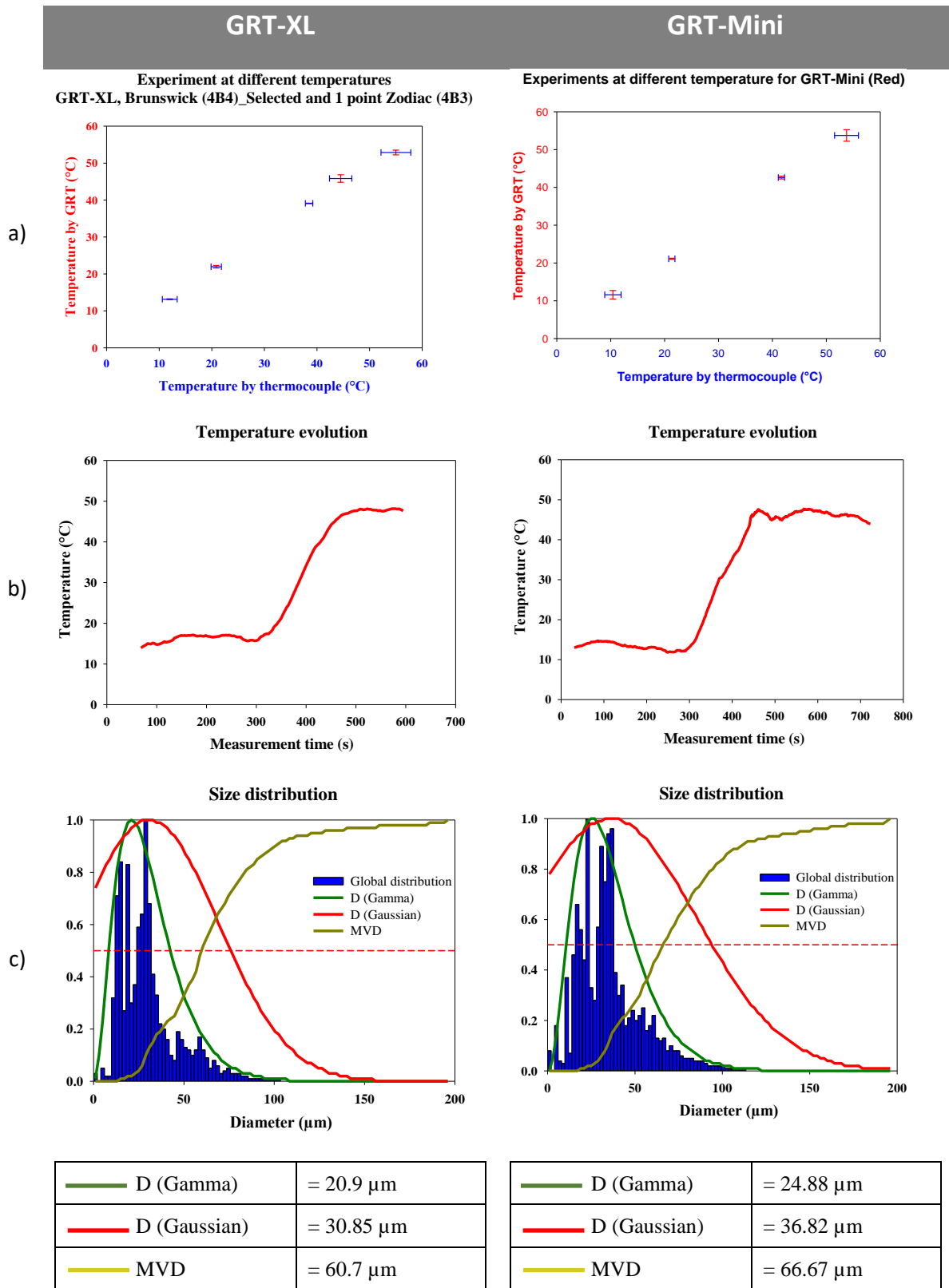


Figure 9: Water spray characterization by using RainbowVision SAS devices GRT-XL and GRT-Mini a) GRT temperature versus thermocouple temperature b) GRT temperature versus time c) size distribution

4.4 Sensitivity, accuracy and uncertainty of GRT in laboratory scale

There are two main steps to extract the droplet temperature by using GRT. First, the average refractive index is extracted from the global rainbow images. Second, the average refractive index is transformed to average temperature by using the appropriate relationship. These two steps must be independently evaluated.

4.4.1 Refractive index measurement accuracy

To validate the quality of refractive index measurements, standard solutions of water and ethanol at different concentrations have been used. Figure 10 shows the index of refraction of sprays measured by GRT (red squares) and the index of refraction measured by a classical refractometer [28] [29] on the bulk liquid (green triangles) versus the concentration of ethanol. The result demonstrates that the GRT measurements have an accuracy equivalent to classical refractometer. The GRT accuracy on the measurement of the refractive index value is to the fourth decimal. It will be noted that a change as small as 0.0001 on the average refractive index is measurable.

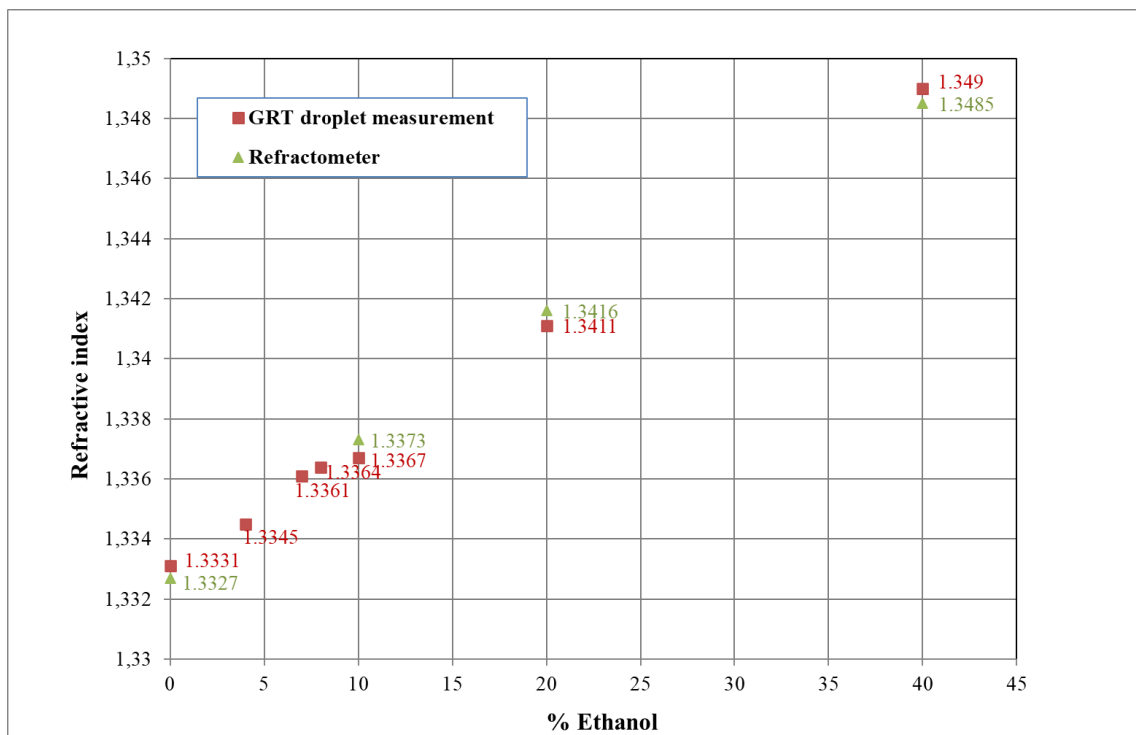


Figure 10: Comparison of refractive index measurement between GRT and refractometer for different liquid spray

4.4.2 Water refractive index/temperature relationship

The temperature measurement accuracy is a function of the dependence the refractive index with the temperature. Accordingly, the temperature measurement accuracy will depend on the particular liquid involved. As shown in figure 11, the dependency of the refractive is rather pronounced among different substances than temperature related. The relationship between temperature and refractive index is linear for ethanol, N-heptane and dodecane. However, for water, the behaviour is more complex with a change of slope at about 20°C.

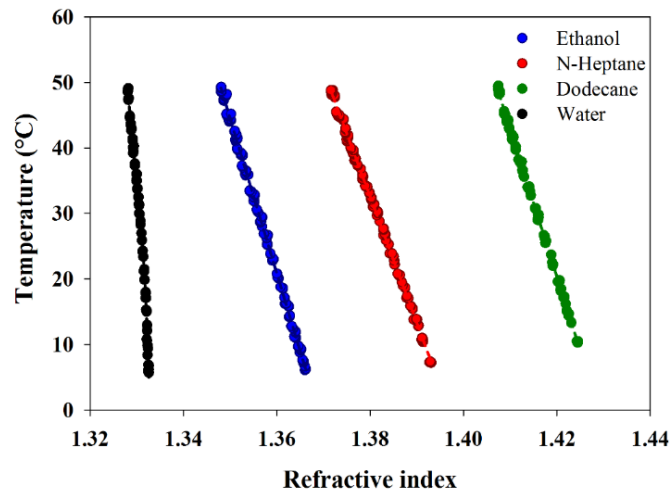


Figure 11: Relationship between refractive index and temperature for four different liquids

This nonlinearity of the relationship between refractive index and temperature for water is clearly visible in Figure 12 where the refractive index values for negative temperature are introduced. At 0°C corresponds a maximum of the refractive index value. Moreover, measurements of liquid water refractive index for negative temperatures are rare in the literature and can be found only for a few wavelengths.

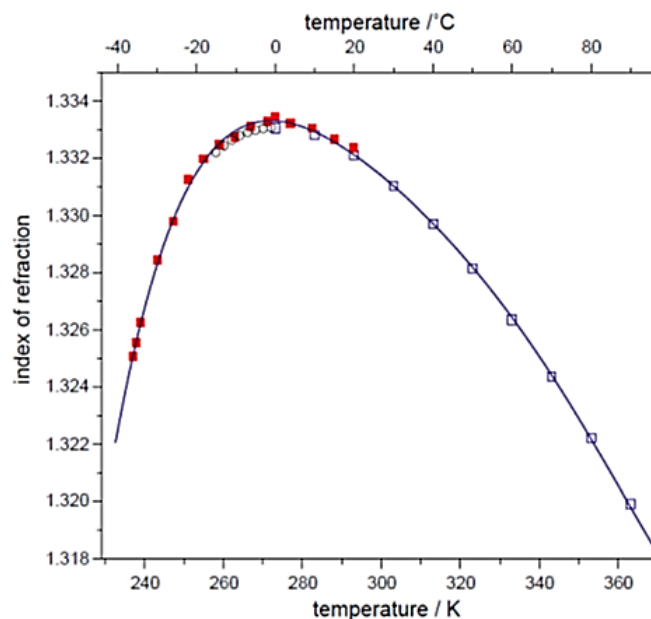


Figure 12: Behavior of the water refractive index versus temperature at 0.6328 μm

The main publications on water refractive index versus temperature are:

- C. Saubade, Indice de refraction de l'eau pure aux basses temperature pour la longueur d'onde de 5893 Å., J. Physique, 359-366 (1981)
- D. Duft and T. Leisner, the index of refraction of supercooled solutions determined by the analysis of optical rainbow scattering from levitated droplets, International Journal of Mass Spectroscopy, 233, 61-65, (2004). Measurements carried out at 0.6328 μm
- A.N. Bashkatov and E.A. Genina, Water refractive index in dependence on temperature and wavelength: a simple approximation, Proc. Of SPIE, vol 5068 (2003)
- IAPWS R9-97: The international association for the properties of water and steam, Release on the refractive index of ordinary water substance as function of wavelength, temperature and pressure, September 1997.
- I. Thormählen, J. Straub and U. Grigull, Refractive index of water and its dependence on wavelength, temperature and density, J. Phys. Chem. Ref. Data, 14, 4 933-945, 1985.

The first two publications correspond to experimental results obtained by the authors, while the last three publications correspond to results obtained from the compilation and statistical treatment of a large number of results obtained by many authors.

The results of C. Saubade were obtained using a refractometer at the wavelength of 0.589 μm , for temperatures between -12 °C and +20 °C.

The results of D. Duft and T. Leisner were obtained from rainbows recorded on levitating water drops at the wavelength of 0.6328 μm , for temperatures between -33 °C and +24 °C.

A.N. Bashkatov and E.A. Genina proposes a formula for calculating the water refraction index at an arbitrary wavelength for temperatures between 0 °C and +100 °C.

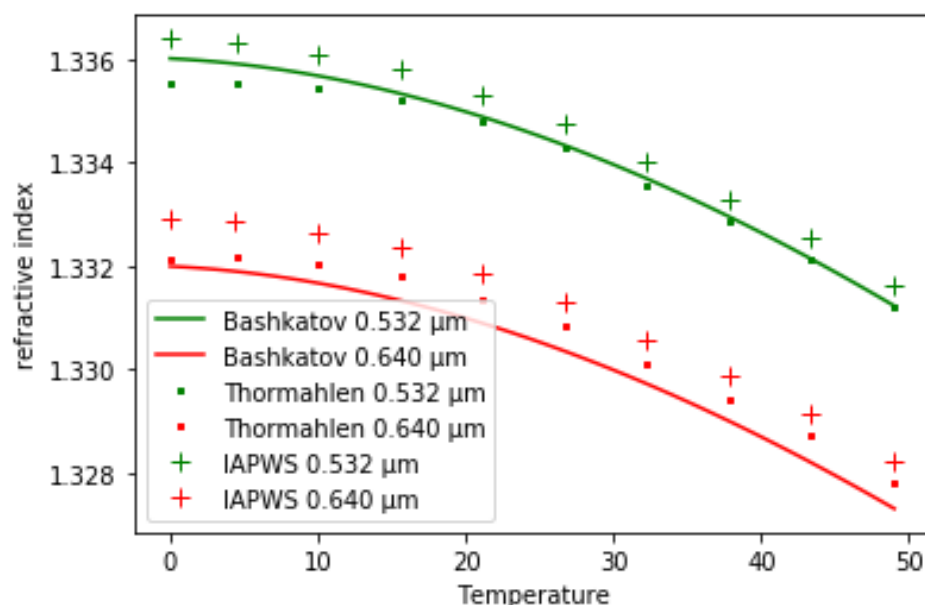


Figure 13: Comparison between the predictions for positive temperatures

The international Association for the properties of Water and Steam (IAPWS) proposes a formula to compute the refractive index of water for wavelengths between 0.2 and 1.1 μm and temperature between -12°C and +500°C with an uncertainty smaller than 6.0×10^{-5} .

Thormählen et al, using an approach close of IAPWS, propose an alternative formula with nearly the same range of application.

Figure 13 compares the evolution of the refractive index at 0.532 μm and 0.640 μm computed with the formulae of Bashkatov, IAPWS and Thormählen for positive temperatures. The three formulae show the same tendency but the values are different.

In Figure 14-a, the predictions at 0.532 μm for a positive temperature are compared to *RainbowVision SAS's* experimental refractometer measurements at 0.532 μm . The three curves converge for the high temperature but diverge for the lowest temperature. Moreover, it can be seen that the *RainbowVision SAS* measurements with a refractometer are in a better agreement with the IAPWS predictions.

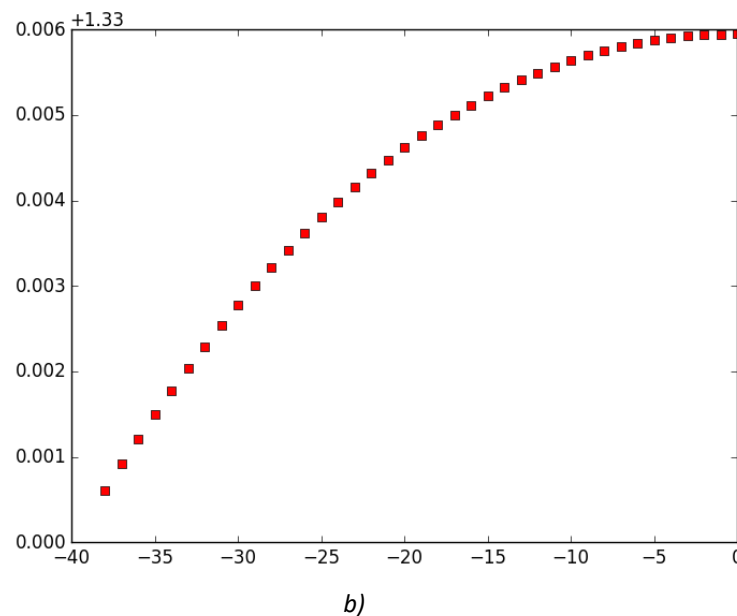
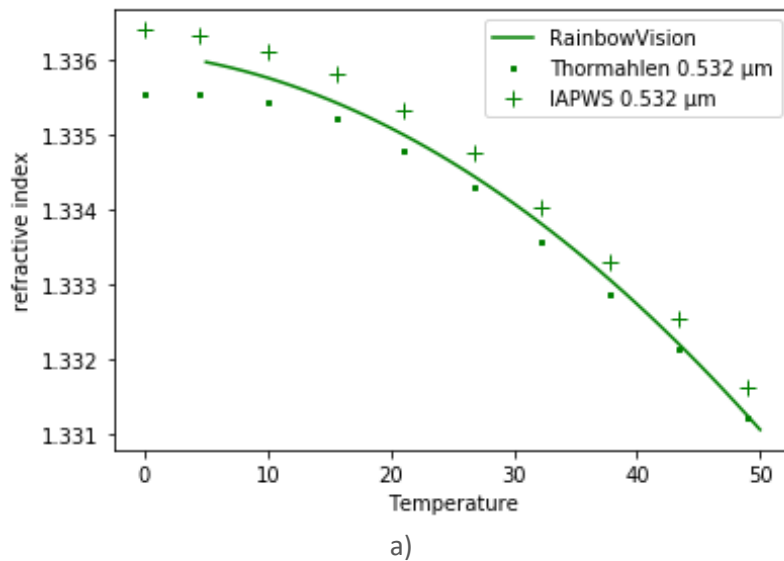


Figure 14: Relationship between refractive index values and temperature. a) Comparison between numerical prediction and experimental results at 0.532 μm for positive temperatures b) IAPWS predictions for negative temperature

Accordingly, we select the couple IAPWS/*RainbowVision SAS* measurements to be the relationship between refractive index measurements and temperature for on the positive temperature scale.

For negative temperatures, we select the IAPWS relationship between refractive index and temperature which is displayed in figure 14-b. As the maximum of the refractive index values is equal to 1.33595 for a wavelength of 0.532 μm , all processed measurements with a refractive index value larger than this limit will be rejected.

4.4.3 Temperature accuracy

The temperature measurement accuracy can be obtained by combining the results of sections 4.4.1 (refractive index accuracy on droplet spray with 80 μm MVD diameter) and 4.4.2 (relationship between refractive index and temperature).

First, the sensitivity of the refractive index to the temperature is obtained from the derivative of the relation refractive index/temperature (section 4.4.2). This relationship exhibits an extremum: the refractive index sensitivity to temperature depends on the temperature. The sensitivity will be worst close to 0°C, but increases rapidly for lower or higher temperatures, as exemplified in Figure 15.

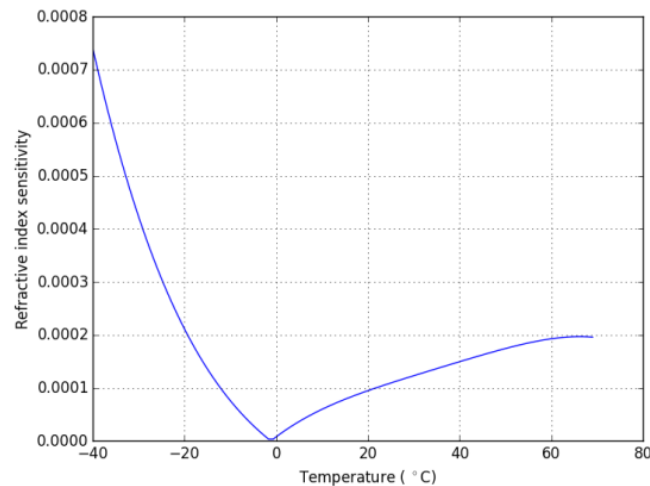


Figure 15: Sensitivity of the refractive index versus temperature for water

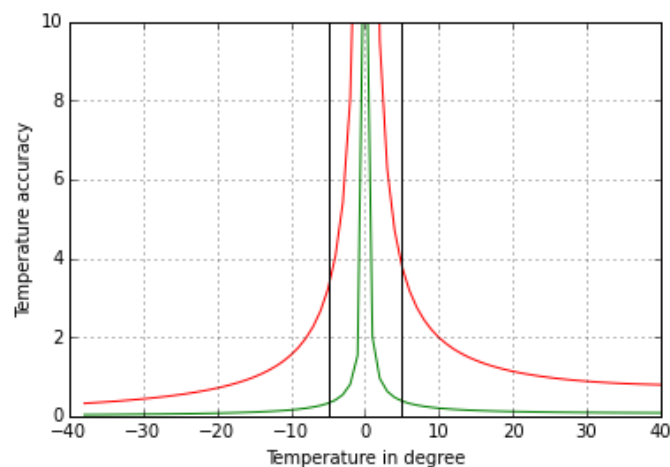


Figure 16: The profile of water droplet temperature measurement accuracy by GRT

As mentioned in section 4.4.1 the refractive index accuracy of GRT is about 0.0001. The associated temperature accuracy is plotted in red in Figure 16. To increase the temperature accuracy, a statistical analysis of the refractive index measurement must be carried out. For a sufficient number of measurements (typically 200 images), the refractive index measurement accuracy is increased up to about 0.00001. In this case, the temperature accuracy measurement is increased as plotted in the green line.

Accordingly, in the laboratory the water temperature measurement accuracy is about 1°C.

4.4.4 Size Accuracy

To validate the size measurement by GRT technique, Phase Doppler Analyzer (PDA) in the Dual mode configuration from DANTEC is used. Standard sprays created by an ultrasonic injector (Sonics, VCX 130, 45 kHz) with different liquid flow rates are investigated. The measurements are carried out along the spray axis, at about 5 cm from the nozzle orifice. The PDA and GRT measurements have been carried out simultaneously.

However, the measurement positions of these two techniques are shifted by 4 mm along the spray longitudinal axis. Each PDA measurement corresponds to 50,000 droplets while each GRT measurement corresponds to an average size distribution over 100 images (one image corresponds an exposure time of 100 ms). The measured size distributions by PDA and GRT have been fitted by a gamma function. Then, the normalized volume distributions have been computed from the gamma fitted size distributions.

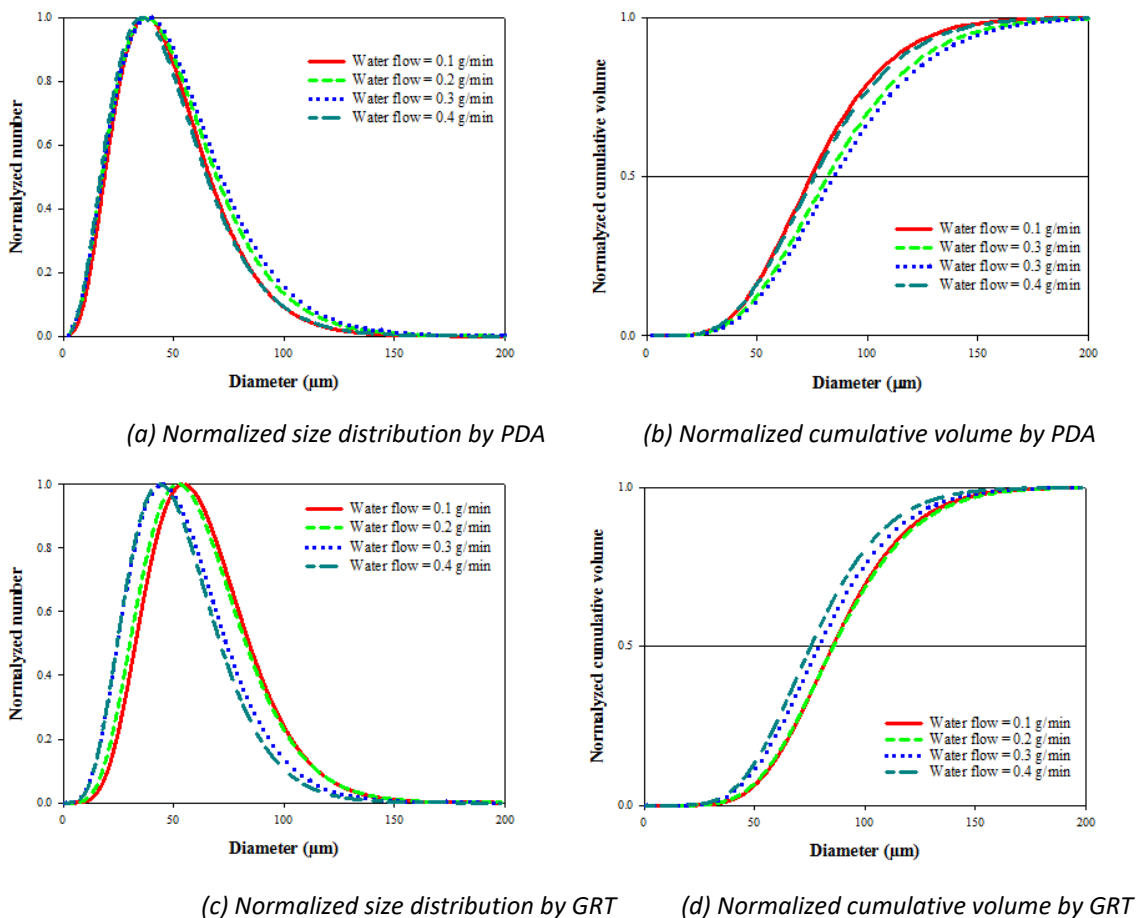


Figure 17: Comparison between PDA and GRT for size distribution measurements

Figure 17 compiles the obtained size distribution as well as the associated volume distribution for the PDA and GRT measurements. The curves are not identical but the obtained behaviors are close. The comparison of the size measurement between two techniques for different liquid flow rates is presented in Table 2. Table 2 compiles the maximum of the fitted size distribution (D_{max}) and the MVD, as a key parameter in IWT, obtained from the fitted distribution (MVD_g). This study shows that MVD_g measurements by PDA and GRT are in agreement with a deviation smaller than 15%.

Flowrate (g/s)	PDA Measurements		GRT Measurements	
	D_{max} (μm)	MVD_g (μm)	D_{max} (μm)	MVD_g (μm)
0.1	37.43	75.20	54.78	85.10
0.2	37.06	82.14	52.26	85.10
0.3	36.49	84.90	45.27	79.10
0.4	35.48	76.03	44.01	75.26

Table 2: Comparisons between PDA and GRT measurements for maximum diameter (D_{max}) and MVD_g .

4.4.5 Multi-modal Rosin-Rammler distribution

Initially, our GRT inversion processing software extracts the size distribution without any assumption on its shape. The measured droplet size is displayed as a size histogram in number. Then, the extracted size distribution is fitted by a Gaussian and Gamma functions, assuming a monomodal distribution. These representations are complemented by a cumulative distribution in volume, directly computed from the size distribution in number. The cumulative distribution in volume permits to determine the MVD of the spray as shown in Figure 18.

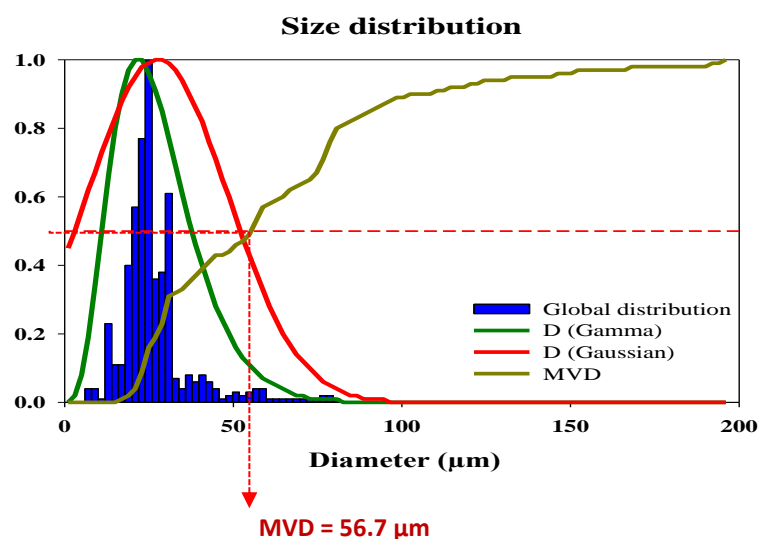


Figure 18: Size distributions and MVD by GRT

To refine this quantification of the droplet size and to facilitate comparisons with numerical simulations, it is important to be able to quantify spray modality. For this purpose, the Rosin-Rammler distribution is used to represent the cumulative volumetric distribution:

$$RR_v = (1.0 - \exp(-(x/a)^b))$$

where “ a ” can be seen as the mean diameter, “ b ” defines the width of the distribution and “ x ” is the diameter as the independent variable in this function.

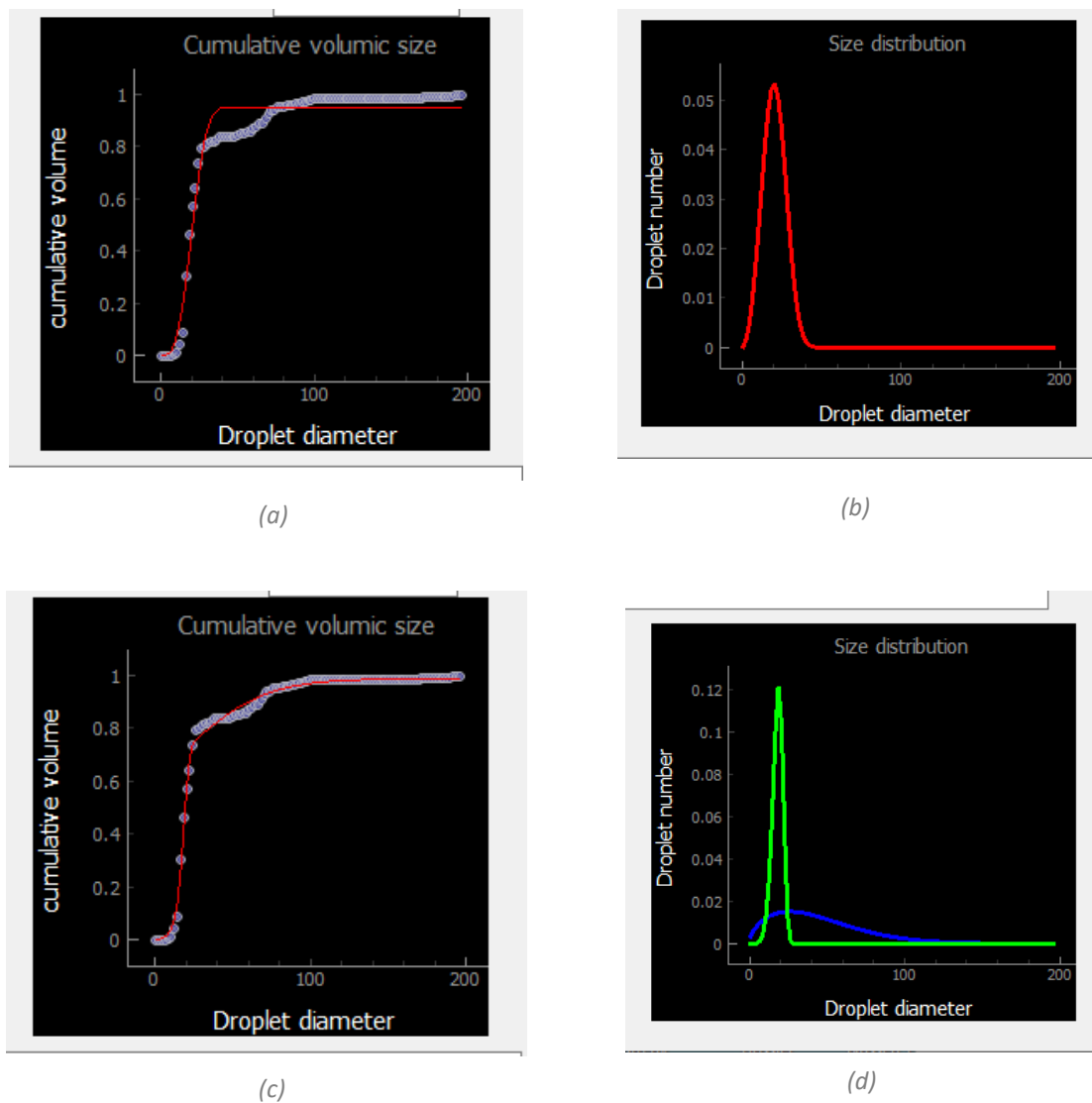


Figure 19: Cumulative volumetric distribution fitting by multimodal Rosin-Rammler distributions a) Cumulative volumetric distribution fitting by a monomodal Rosin-Rammler distribution b) The extracted monomodal Rosin-Rammler distribution c) Cumulative volumetric distribution fitting by a tri-modal Rosin-Rammler distribution d) The extracted bimodal Rosin-Rammler distribution

Accordingly, the fitting of the cumulative size distribution in volume by a Rosin-Rammler distribution, possibly tri-modal, has been added. This new information permits to identify easily and quantify the level of modality of the spray.

Figure 19 compares the Rosin-Rammler distributions extracted from the same measurement, represented by light blue circles in Figure 19(a) and Figure 19(c). When the fitting imposes a monomodal Rosin-Rammler distribution, the extracted distribution is characterized by diameter of 23.2 μm , at a width of 3.2 for 95% of the mass as displayed as a red line in Figure 19(b). The reconstructed cumulative volumetric distribution from these parameters is represented by the red line in Figure 19:(a)

When the fitting accepts up to three Rosin-Rammler distributions, a bimodal distribution is obtained characterized by: diameter₁ = 19.7 μm , width₁ = 6.5 for 65.8 % of the mass (green line in Figure 19(d)) and diameter₂ = 50 μm , width₂ = 1.57 for 33 % of the mass, blue line in Figure 19(d). The reconstructed Rosin-Rammler cumulative volumetric distribution with these parameters is represented by the red line in Figure 19(c), which fits perfectly the measured blue circles.

4.4.6 Large particle extension

For SLD study, one of the challenges is the fact that the occurrence of a few large droplets with in a cloud of small droplets might be statistically smaller. Moreover, the temperature of the small and large droplets can be different.

To be able to quantify the effect of such configurations in a measurement, to define the limits of our devices as well as to explore possible strategies to be able to separate SLD contributions from small droplets contributions, a simulation code has been written and experiments have been carried out, accordingly.

4.4.6.1 Numerical contribution

The main points of the developed code are now briefly described:

- The size distribution is assumed to be bimodal and each component of the size distribution is assumed to be described by a Gaussian law
- For each component of the size distribution, the user introduces the mean diameter, the width of distribution, the refractive index as well as a number of particles
- The diameter of the droplet is determined by a random process weighted by the Gaussian law.
- The size distribution in number and in volume are plotted
- Then, the global rainbow light distribution is computed and plotted by summing the individual contribution of each particle.
- The next step is to inverse this light distribution to obtain an average refractive index and a size distribution. The extracted size distribution and refractive index are compared to the initial values as well as the initial and reconstructed light distribution.

The use of the code is now exemplified:

Assuming a cloud of 1000 droplets at -21.5°C ($n = 1.3344$) with a mean diameter of 50 μm and a width of 10 μm . Inside this cloud, we assume the presence of five big droplets at 0°C ($n = 1.33595$) with a mean diameter of 300 μm and a width of 20 μm .

The first step is to compute the size distribution, which is plotted in Figure 20:

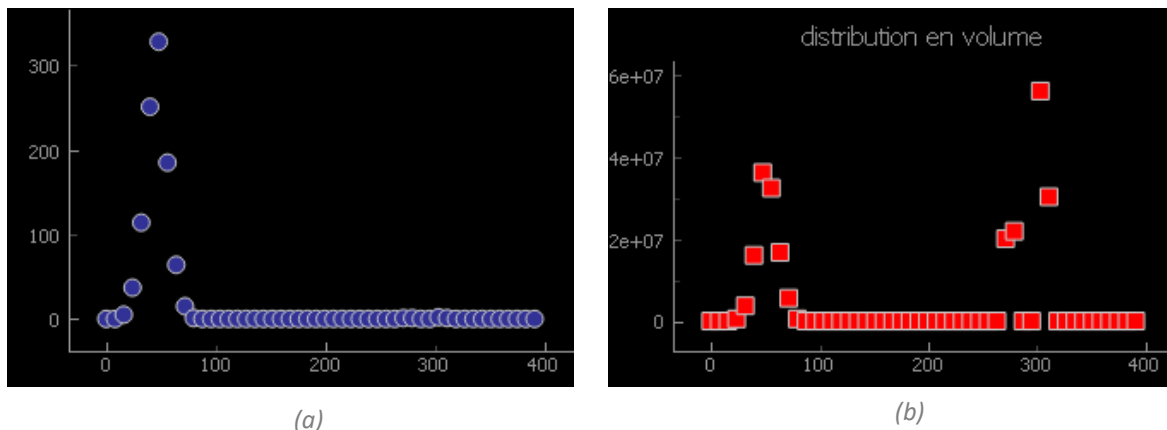


Figure 20: The initial size distribution for 1005 droplets a) The initial size distribution in number b) The initial size distribution in volume

The second step is to compute the global rainbow signal created by these 1005 droplets which is displayed in 1.

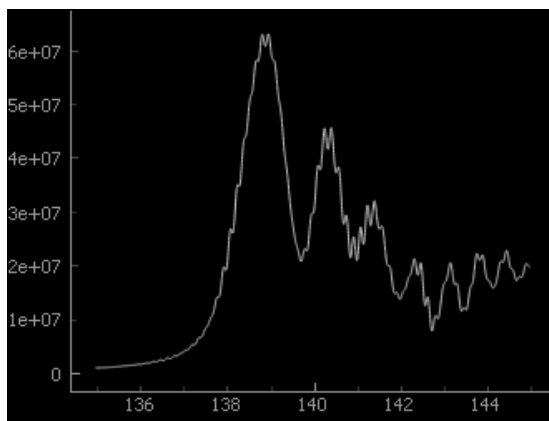


Figure 21: The computed global rainbow for 1005 droplets

Finally, this global rainbow signal is inverted with our code. Figure 22 displays the extracted size distributions in number (Figure 22 (a)) and in volume (FIGURE 22 (b)). The extracted size distributions are in good agreement with the initial size distribution displayed in Figure 20.

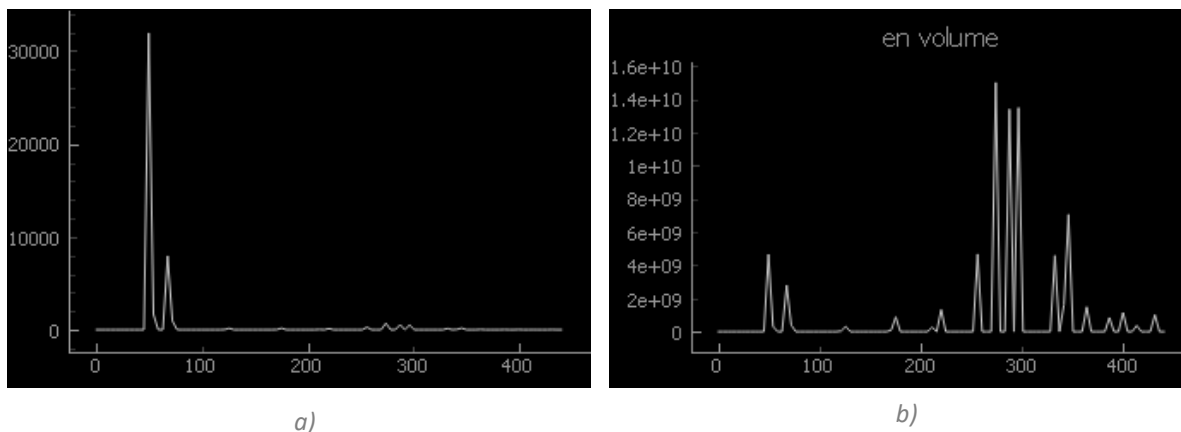


Figure 22: Extracted size distribution for 1005 droplets a) Extracted size distribution in number b) Extracted size distribution in volume

Figure 23 compares the initial light distribution in red to the reconstructed light distribution in blue. The agreement is excellent.

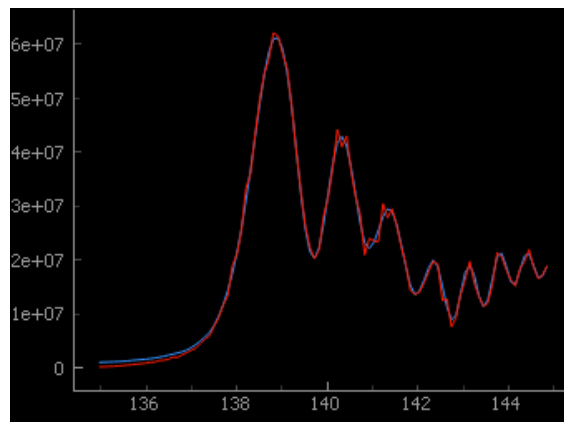


Figure 23: Comparison between initial light distribution in red and recomputed light distribution in blue for 1005 droplets

In this case, the extracted average refractive index value is equal to 1.33500, corresponding to an average temperature of about -17°C.

If the number of big droplets is reduced to only one droplet, the following size distribution is obtained shown in Figure 24:

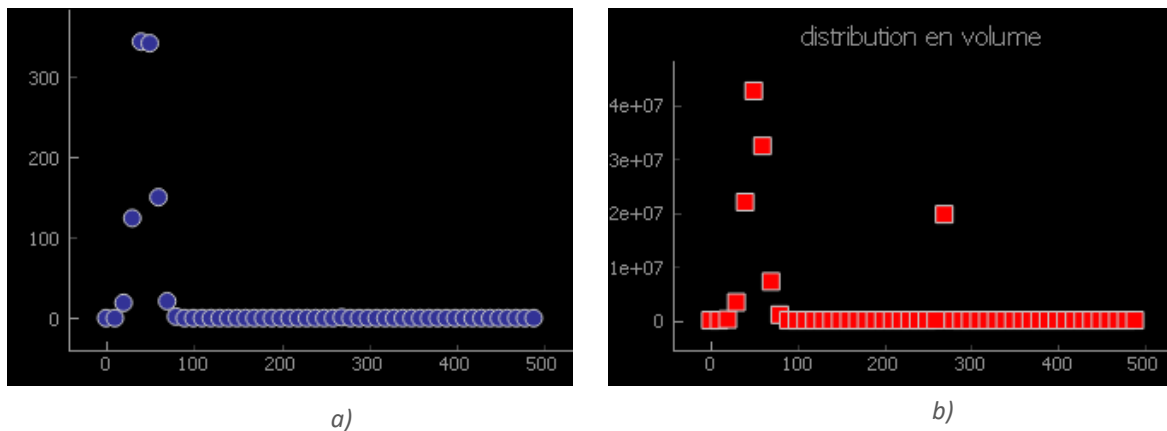


Figure 24: The initial size distribution for 1001 droplets a) The initial size distribution in number b) The initial size distribution in volume

Figure 25 represents the computed global rainbow signal by 1001 droplets. Then the signal is processed. The good agreement between reconstructed signal in blue and the initial signal in red is evidenced as shown in Figure 26.

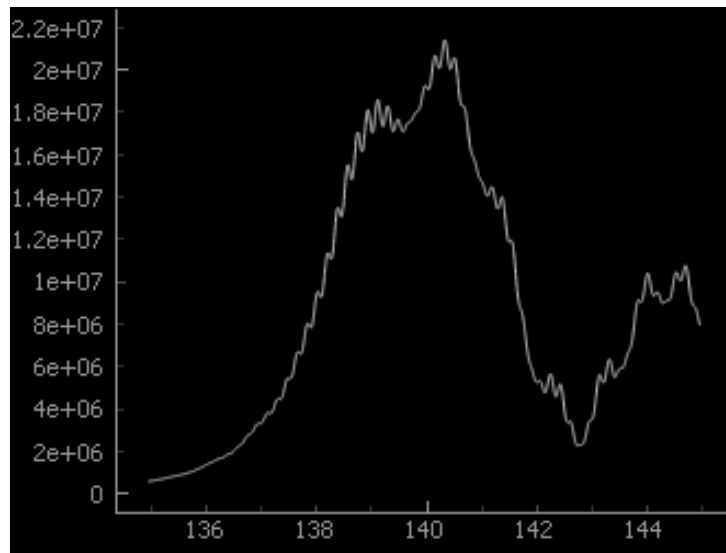


Figure 25: The computed global rainbow for 1001 droplets

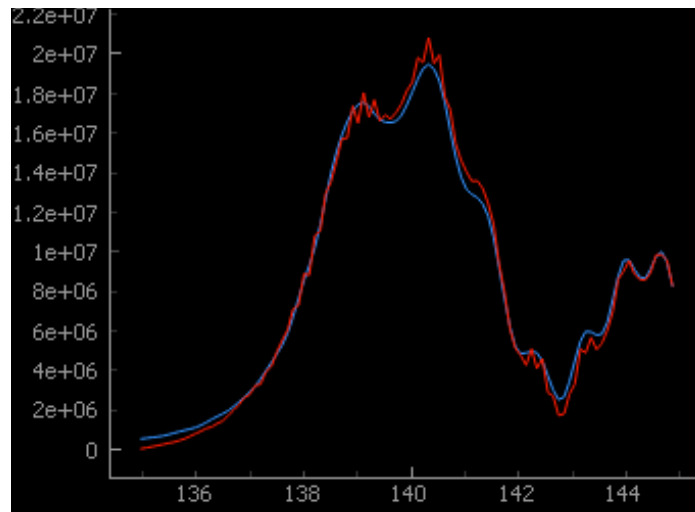


Figure 26: Comparison between initial light distribution in red and recomputed light distribution in blue, for 1001 droplets

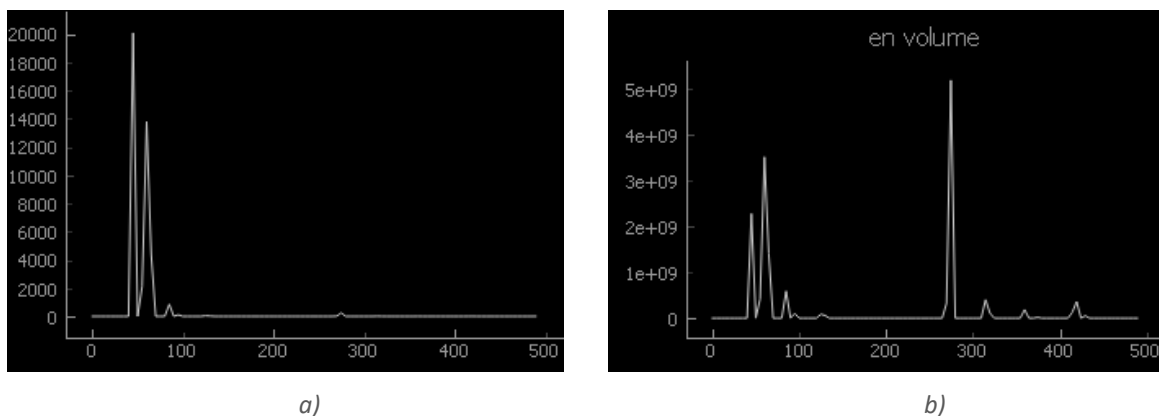


Figure 27: Extracted size distribution for 1001 droplets a) Extracted size distribution in number b) Extracted size distribution in volume

In this case, the extracted average refractive index is equal to 1.33479, corresponding to an average temperature of about $-18.7\text{ }^{\circ}\text{C}$

These two example results demonstrate and quantify the effect of only a few large droplets inside a cloud of small droplets, possibly with a different temperature. These results show that the new algorithm is able to extract from the complex global rainbow pattern a reliable size and temperature distribution. The size distribution is well described and the “measured” average temperature is between the hottest and colder, as expected.

Moreover, this approach is a necessary step to propose and develop a processing strategy to be able to extract both the large droplet temperature and the small droplet temperature simultaneously.

4.4.6.2 Experimental contribution

Complementing of the numerical approach where the main assumption is that the droplets are assumed to be spherical, an experimental study has been carried out.

This experiment is based on the use of a monodispersed generator from *FMP technology* with orifice plates in the range of 100 to 500 μm , permitting create chain of water droplets in the range of 200 to 1000 μm to be generated. The droplet generator is located with the orifice at the bottom, so that the ejected droplets are falling down.

The experiments have been carried out for several orifice sizes, flow rates and frequencies excitations. Example of results are displayed below.

At first, large droplets have been generated with an orifice of 125 μm , a flow rate of 11.46 ml/min and an excitation frequency of about 3.4 kHz creating a chain of droplets with diameters in the range of 250-300 microns.

Figure 28 displays three typical global rainbows for a spray corresponding to:

- the global rainbow recorded from a line of droplets from a 125 μm orifice, (a)
- the global rainbow recorded from a spray from an ultrasonic droplet generator, (b)
- the global rainbow recorded superposing the spray and the line of droplets, (c)

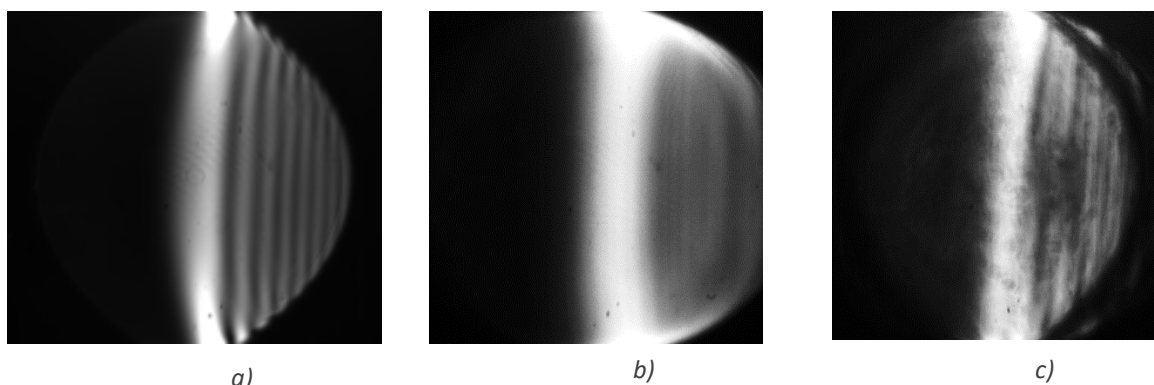
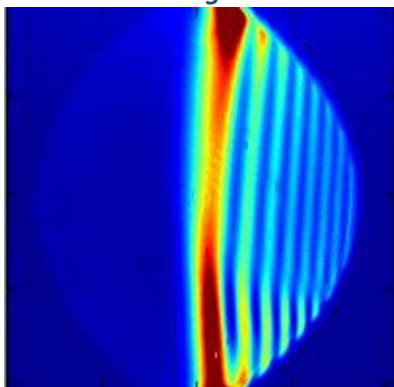


Figure 28: Experimental validation on a mixing of small droplets spray with big droplets a) Chain of 250 μm droplets b) Spray of 50 μm droplets c) Spray of 50 μm droplets with chain of 250 μm droplets

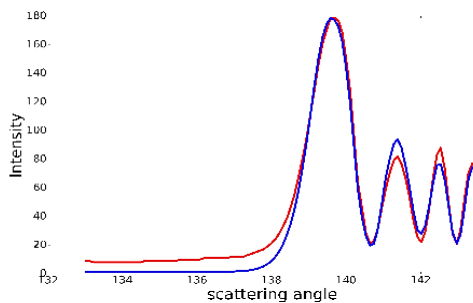
To be able to process such a large range of droplet sizes efficiently and accurately, the software has been modified as follows:

1. A first inversion is carried out with a maximum size of about 200 μm (size step of 2 μm). The quality of the inversion is quantified from the distance between the original light distribution and the recomputed light distribution
2. Then the maximum size is increased by a step of 50 or 100 μm , and the inversion quality is quantified
3. This procedure is carried out up to minimize the distance between the original light distribution and the recomputed light distribution

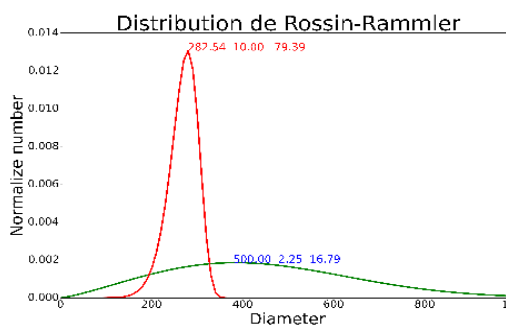
Case1: Quasi monodispersed chain of large droplet
Images



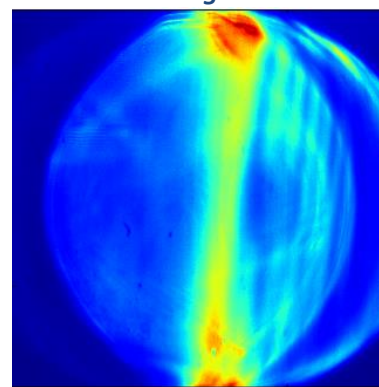
The light distribution



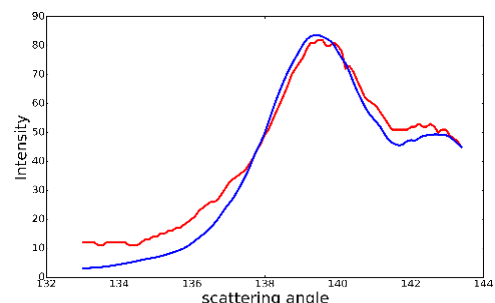
The extracted size distribution



Case2: Quasi monodispersed chain of large droplet + small droplet
Images



The light distribution



The extracted size distribution

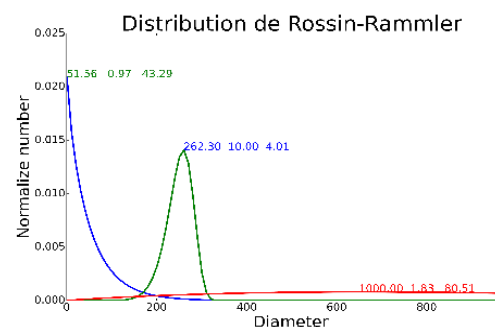


Figure 29: Two examples of sprays containing large droplets

Figure 29 displays typical signals recorded from sprays with large droplets. The first column in Figure 29 corresponds to the global rainbow image collected from a chain of large monodispersed droplets and the associated processing results. In that column, the second row compares the extracted and recomputed scattering diagram while the last diagram displays the extracted Rosin-Rammler distributions. The size distribution is essentially monodispersed with a size of about 290 microns for 80% of the mass (red line)

The second column in the figure corresponds to the global rainbow images from the mixing of a chain of large droplets with a spray of small droplets. In that column, the second row compares the extracted and recomputed scattering diagram while the last diagram displays the extracted Rosin-Rammler distribution. The green curve corresponds to the contribution of droplets with a size of about 260 μm for 40% of the mass, while the blue line corresponds to the contribution of small droplets for 45%. The presence of the large droplets in the cloud of small droplets is well perceived. Nevertheless, in this representation the peak of small droplets is not well described due to the histogram step (10 μm) selected to also capture the large droplets peak.

Simultaneously, the droplet temperature has been estimated via the measurement of the droplet refractive index. The challenge is that the rainbow angular position is also dependent on the droplet shape. A departure of the droplet sphericity creates an angular shift of the rainbow which is a function of the droplet ellipticity and droplet 3D orientation. Accordingly, the GRT provides access to the droplet temperature only if the droplet orientations are fully random [20] [15] [16]. As the aim of monodispersed droplet generator is to produce a chain of identical droplets with the same trajectory, the random aspect is obtained by randomly changing the excitation frequency. Accordingly, this procedure creates a series of droplets with different shapes and orientations at the measurement point, with the selected exposure time to be long enough to assure good statistics. In this case the droplet temperature is measured to be equal to about 21°C but with an accuracy of about 4°C. This accuracy can be improved by selecting only the rainbow images with a strong symmetry i.e., the rainbow created by the less deformed large droplets [30] [31].

4.4.7 GRT laboratory accuracy conclusion

As previously described, the global rainbow technique measures the droplet temperature via the refractive index value. It has been demonstrated that GRT devices exhibit high performance to measure droplet refractive index value. The accuracy is about 0.0001, independently of the liquid under study. But on the contrary, the relationship between refractive index value and temperature is strongly dependent on the liquid. The majority of liquids have an essentially linear relationship between refractive index and temperature. However, the refractive index curve for water for instance reveals a non-linear and non-monotonic behavior with temperature. Hence, for water the GRT temperature measurement accuracy becomes a function of the temperature (see Figures 15 and 16).

Accordingly, the calibration of the GRT devices is carried out with pure water. The generation of a standardized droplet size, number concentration and temperature for calibration is not a trivial task. Despite this difficulty, it has been shown that such an effort is worthwhile. Such a task can be carried out in the laboratory conditions by using a chain of perfectly monodispersed droplets as well as a quasi-monodispersed spray created by an ultrasonic nozzle to calibrate GRT systems. Under such conditions, it has been shown that the GRT accuracy for the droplet temperature is equal to about 1°C, except close to 0°C (shown in table 3) while the size accuracy is comparable to PDA accuracy.

Liquid	Size range	Temperature range	GRT Measurement Accuracy		
			Temperature accuracy		Size resolution
			1 image	200 images	(μm)
Water	20-300 μm	-5°C to 5°C	3°C	2°C	3
		-5°C to -10°C and 5°C to 10°C	2°C	1°C	3
		-10°C to -38°C and 10°C to 100°C	1°C	<1°C	3
Ethanol	20-300 μm	-114°C to 78 °C	< 1°C	<1°C	3
N-Heptane	20-300 μm	-90°C to 98 °C	< 1°C	<1°C	3

Table 3: GRT droplet temperature and size measurement accuracy under laboratory conditions

The next step is to measure the droplet temperature under real IWT conditions.

5 Temperature measurement at TUBS

5.1 Braunschweig Icing Wind Tunnel (BIWT) Description

TU Braunschweig is equipped with a state-of-the-art icing wind tunnel shown in Figure 30. BIWT is a closed loop wind tunnel with a 1.5 m long test section of 0.5m X 0.5m cross section [32] capable of both liquid and ice crystal icing. The tunnel can operate between 5m/s to 40 m/s while maintaining a temperature up to -20°C. The tunnel is fully calibrated as per SAE ARP 5905 standard for the Appendix-C icing conditions and several inter-instrumentation comparisons are made.

A wide range of droplets can be generated in the TUBS IWT with its two stand-alone sets of atomizers, the first set of atomizers (A) can produce MVD up to 80 μm and liquid water content between 1.1 – 3 g/m^3 . The second set of spray nozzles (B) can produce small droplets with a MVD between 8-60 μm with LWC between 0.1 – 2 g/m^3 . The size distribution is measured with PDI (Phase Doppler Interferometer), HIS (High Speed Imaging) and 2D-S probes, the corresponding LWC water content is derived, the LWC of the cloud is also measured with Cranfield IKP. The BIWT was recently upgraded with a new set of nozzles (C) that in combination with nozzles (B) is capable of providing sprays that meet Appendix O FZDZ conditions. The size distribution is measured with PDI, Shadowgraphy and CCP in collaboration with DLR.

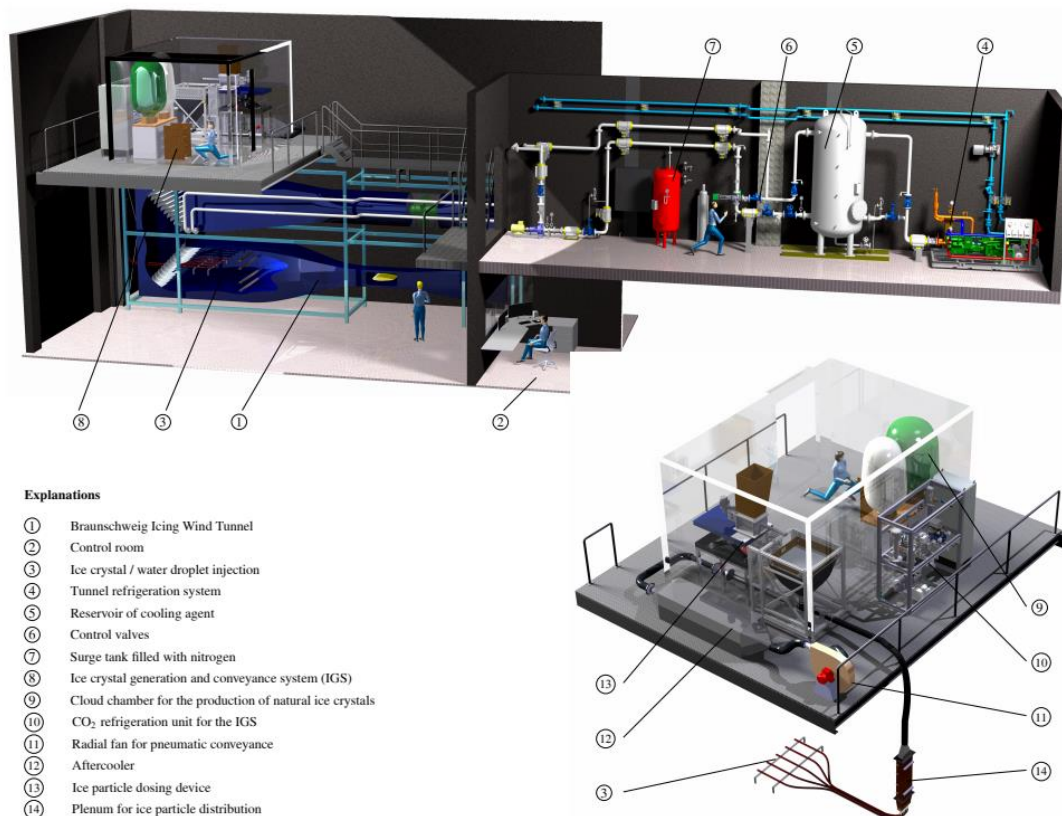


Figure 30: Illustration of Braunschweig Icing Wind Tunnel facility

The water reservoir of the spray system can be coupled to an external heat exchanger that facilitates a wide choice of droplet injection temperatures in the range +2 °C to 55 °C. The warm droplets emitted from the nozzle will be cooled down to the test section temperature during their short transit between the nozzle and the test section. The simulation results in the internal deliverable ID 4.5 show that

droplets up to 100 μm will essentially attain the tunnel temperature irrespective of the injection velocities and temperatures.

5.2 IWT measurement conditions and GRT-XL installation

RainbowVision SAS provided the GRT-XL instrument to measurement of the droplet temperature in the Braunschweig IWT. The GRT-XL model was installed vertically as shown in Figure 31. An in-house software is used to control the device remotely, as well as record and process rainbow images. The working distance for GRT-XL is limited to 15.5 cm. The device comprises a laser emitting at 0.532 μm and a CCD camera to record the global rainbow produced between 132° to 159°. For better results, the windows are coated with board band anti-reflexion (BBAR) coatings (0.425-0.700 μm).

The GRT probe has already been validated to measure spray temperature and size distribution with droplet MVDs in the range 20-300 μm and in the LWC range 1-3 g/m^3 . A new processing method is developed to measure droplets up to a few millimetres, the validation will be made at a later stage when the project IWTs are upgraded to generate large droplets. A series of measurements are also made at TUBS to test GRT performance at very low LWC of 0.36 g/m^3 .

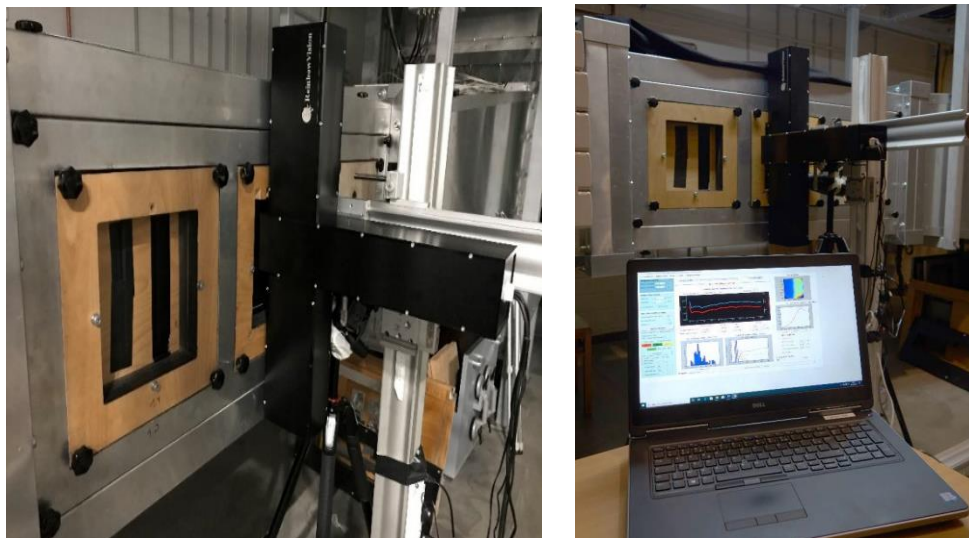


Figure 31: GRT-XL probe in the test section of the Braunschweig Icing Wind Tunnel

Several performance aspects of GRT were tested in the campaign at TUBS IWT in the 44th week of 2019. Primarily, tests were made to evaluate the performance using small droplets with MVD of 20 μm , 40 μm and 60 μm at different tunnel temperatures and velocities. Numerical simulations confirmed that the droplets temperature of the aforementioned droplet sizes would be cooled to the tunnel air flow temperature as they reach the test section for the entire range of velocities and injection temperatures feasible with the BIWT. As the GRT deduces the information of spray's mean temperature, the influence of droplet number density is studied by varying the LWC for the same size. As in the previous chapter already discussed, the refractive index (n) curve as a function of temperature has a maximum near 0°C, n decreases monotonically with increasing or decreasing temperature from the maximum value, thus the GRT measurements are ambiguous in the range -5°C to +5°C; coincidentally the range is critical for the SLD icing conditions. Thus, an emphasis is placed on the performance in this regime. Also, the ability of the GRT in identifying small ice crystals is studied. Additional measurements were conducted with 250 μm spray nozzles at various injection and tunnel temperatures. A second phase of testing is intended when the IWT is upgraded to SLD conditions. The second phase will enable calibrations of the tunnel for tests planned for the development and validation of tools to be developed in WP9.

5.3 Results overview

- The GRT-XL has been adjusted and calibrated at the *RainbowVision* laboratory. So, the first step has been to verify the quality of the GRT-XL measurement capability by measuring the droplet size and temperature on a calibration spray, created by using an ultrasonic injector (Sonics, VCX 130, 45 kHz), at TUBS. This verification has initially been carried out outside and later inside the IWT, through the optical window. Measurement in the BIWT followed, after ensuring that both methods yield to similar results.

During this one-week measurement campaign, a series of measurements have been carried out for following conditions:

- Air temperature (-10°C, -15°C, and -20°C)
- Droplet size (20 μm, 30 μm, 40 μm, and 60 μm)
- Liquid water content (0.36 g/m³ to 1.14 g/m³)
- Air velocity (20 m/s, 30 m/s and 40 m/s)

5.3.1 Temperature measurement

5.3.1.1 Droplet temperature measurement behavior: Overview

All of the measurements carried out at Braunschweig are compiled in Figure 32. The measured droplet temperatures are plotted versus the air temperature inside the IWT, independent of the droplet size and air velocity. This overview underlines the dependence between the droplet temperature and the wind tunnel air temperature. The colder the air stream temperature in the wind tunnel is, the lower the droplet temperature gets, at the same water injection temperature in the nozzle. Moreover, the dispersion of the measured droplet temperature is also visible in this figure.

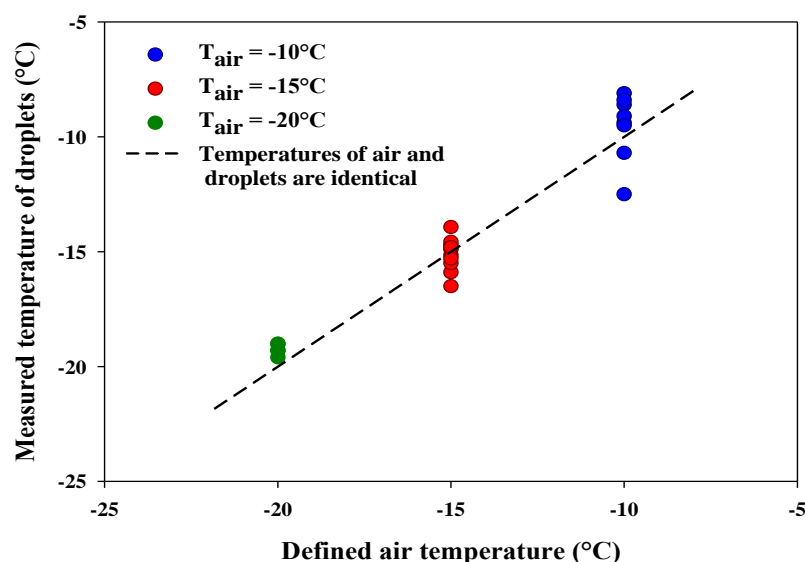


Figure 32: Measured droplet temperature versus the air temperature

This aspect is also exemplified in Figure 33 where the difference between the measured droplet temperature and the wind tunnel air temperature is displayed for different measured MVD. One can see, that:

- The smaller the droplets are, the larger the fluctuations of the droplet temperature from the air wind tunnel temperature are. This effect can be attributed to the fact that the GRT-XL device used at TUBS has been optimized to measure droplets in the range of 20-400 μm . But for smaller droplets (<20 μm), when the collection angle is limited, the maximum intensity of the global rainbow signal is not always recorded, which affects the inversion accuracy.
- For measured droplets smaller than 80 μm , the droplet temperature fluctuations look to be randomly distributed close of the wind tunnel air temperature. On the contrary, for droplets larger than 80 μm , the droplet temperatures look to be higher than the wind tunnel air temperature.

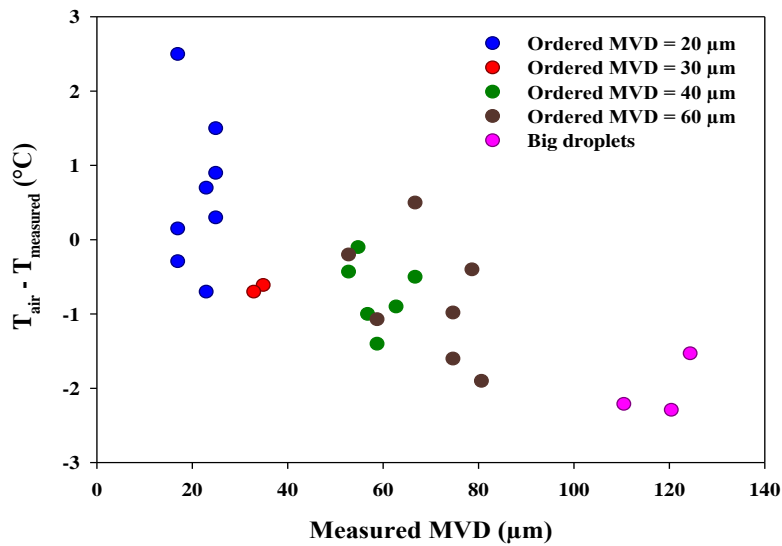


Figure 33: The difference of temperature between the droplet and the wind tunnel air versus the droplet diameter

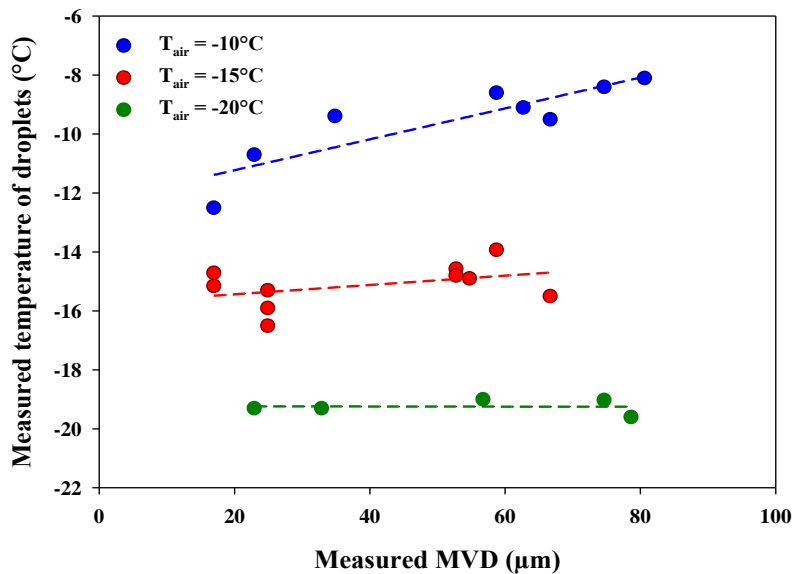


Figure 34: The measured droplet temperature versus the measured droplet MVD, the parameter is the wind tunnel temperature

Figure 34 depicts the measured droplet temperature versus the measured droplet MVD with the air tunnel temperature as a parameter.

For a wind tunnel temperature equal to $-10\text{ }^{\circ}\text{C}$ (in blue), the droplet temperature appears to increase with the droplet size.

For a wind tunnel temperature equal to $-15\text{ }^{\circ}\text{C}$ (in red), the temperature is still larger for the largest droplet, but the slope is smaller than for $-10\text{ }^{\circ}\text{C}$.

For a wind tunnel temperature equal to $-20\text{ }^{\circ}\text{C}$ (in green), the droplet temperature is independent of the droplet size.

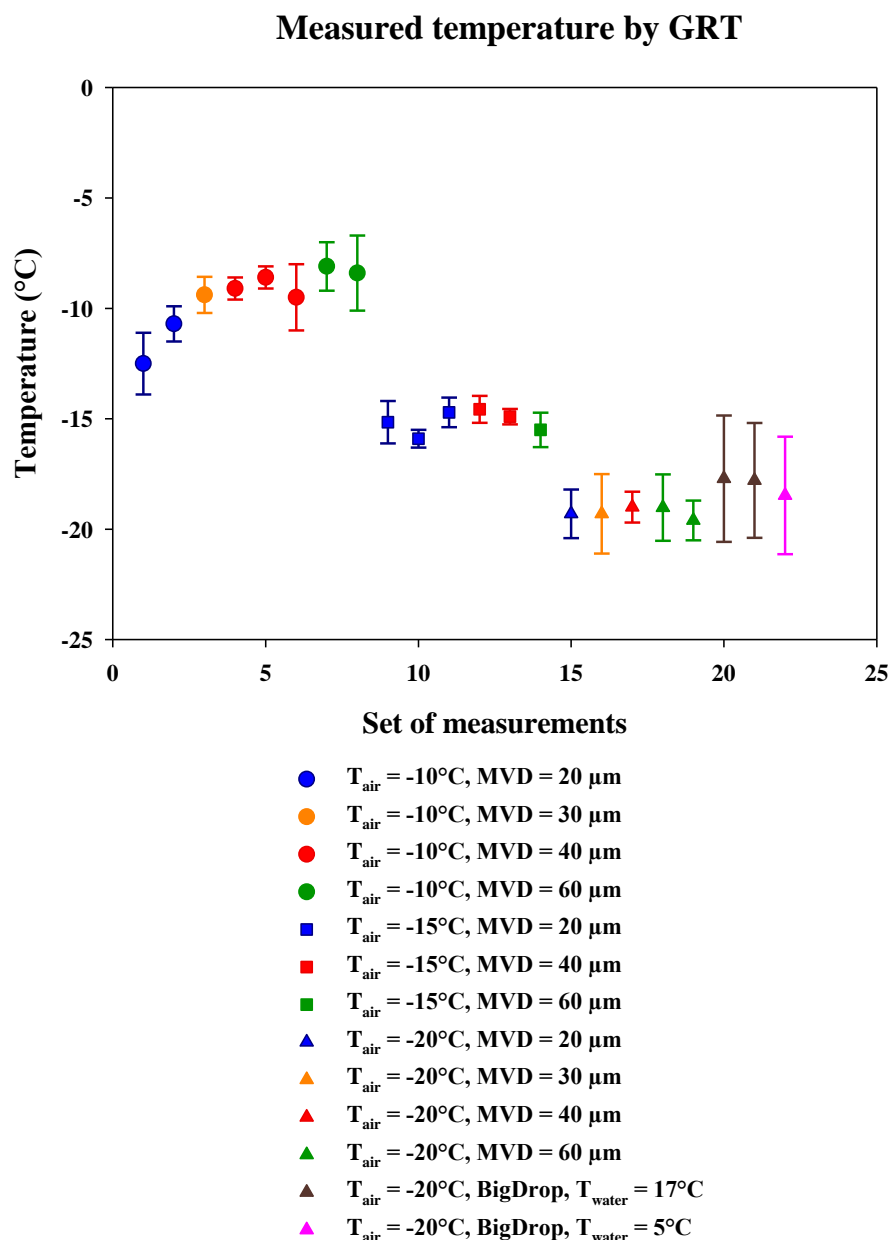


Figure 35: Compilation of droplet temperature measurement for different test conditions (air speed 40 m/s)

Figure 35 compiles all the measurements for an air velocity equal to 40 m/s for the different air wind tunnel temperatures, different droplet sizes and different LWC. The conclusions are essentially identical to the one of Figure 34, except that for the largest droplets (measurements 20th, 21 and 22): the differences between the droplet temperatures and the air temperature inside the wind tunnel are larger as well as the temperature root mean square (RMS). This behaviour is due to the fact that largest droplets in this experiment need the longest time to equalize towards the air temperature, while the RMS values of the temperature are due an in stationary droplet size distribution.

After this overview of the droplet temperature behavior in the BIWT, the next sections will be limited to a range of air tunnel temperatures to focus on the importance of air velocity, droplet size and LWC.

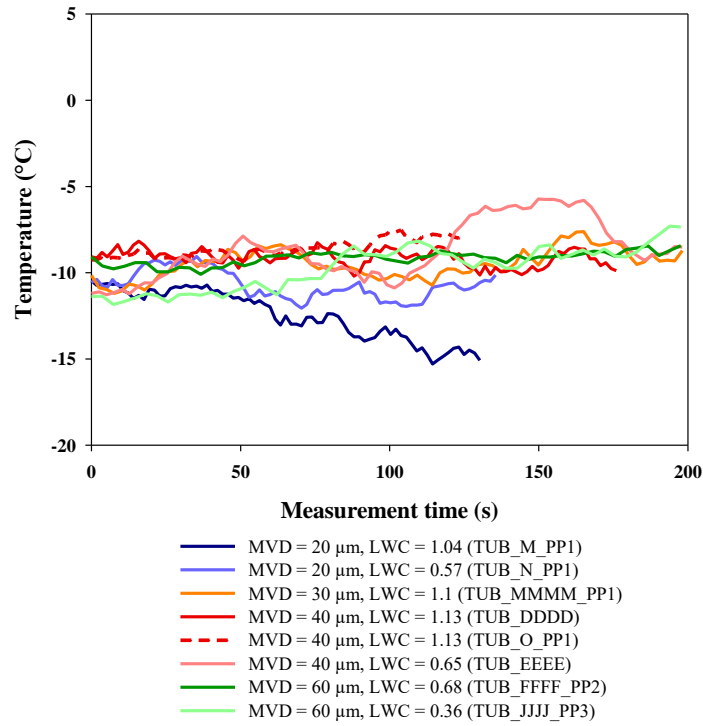
5.3.1.2 Behavior of the droplet temperature for an air tunnel temperature of -10°C

A first series of measurements have been carried out with a wind tunnel air temperature equal to -10 °C. This campaign has been realized on three days: the 28, 29 October 2019 and the 1 Nov 2019. During the measurements in the first two days, it has been observed that the laser beam might oscillates. This unexpected effect will be discussed in more detail in section 5.4. Different strategies have been tested to try to suppress that effect. To this point, it is sufficient to say that this influence has substantially been reduced for the measurement as of 1 November 2019 via heating of the optical window at the laser crossing position combined with a customized post-processing routine.

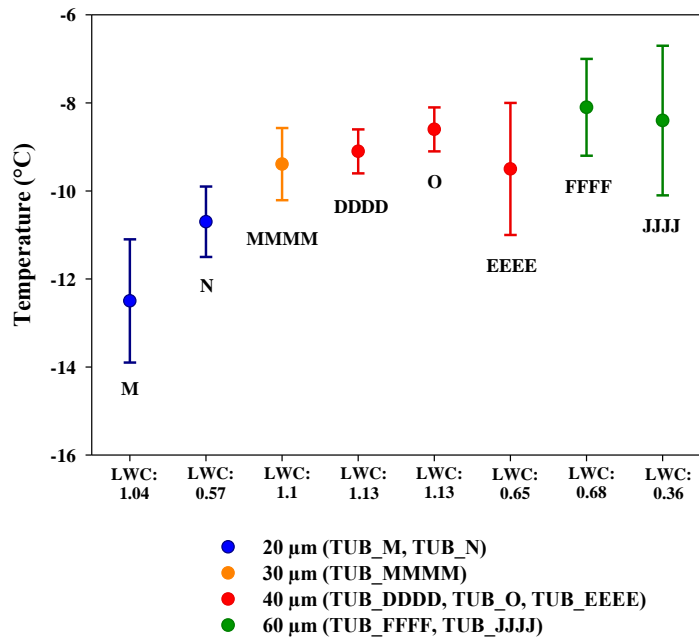
Figure 36 compiles the results obtained for a wind tunnel temperature at -10 °C. Figure 36(a) shows, the temporal temperature evolution, while their statistical behaviour is plotted in Figure 36(b). In Figure 36(b), the central point represents the mean values with the standard deviation as error bars.

The general behaviour is that the temperature deviation between of the droplet temperature and the air stream temperature increases with the droplet size due to an insufficient adaptation time. Nevertheless, the analyses of the signal reveals that for the size of about 20 µm, the signals have a rainbow maximum located at the extremity of the recording region. Accordingly, the inversion process can only be performed inadequately and is very sensitive to any perturbations. This behavior explains the larger RMS of the temperature measurements for the smallest droplets (20 µm ordered).

In extension to Figure 36, Figure 37(a) shows the time series of an expanded measuring. This figure exemplifies the long-time stability of the wind tunnel as well as the measurement reproducibility, with Figure 37(b) depicting the associated statistical representation of the same measurement series.

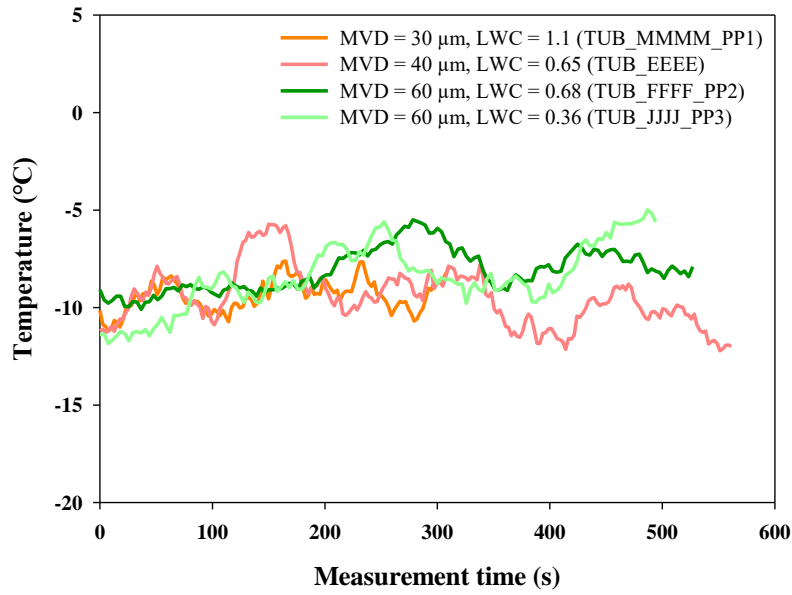


a)

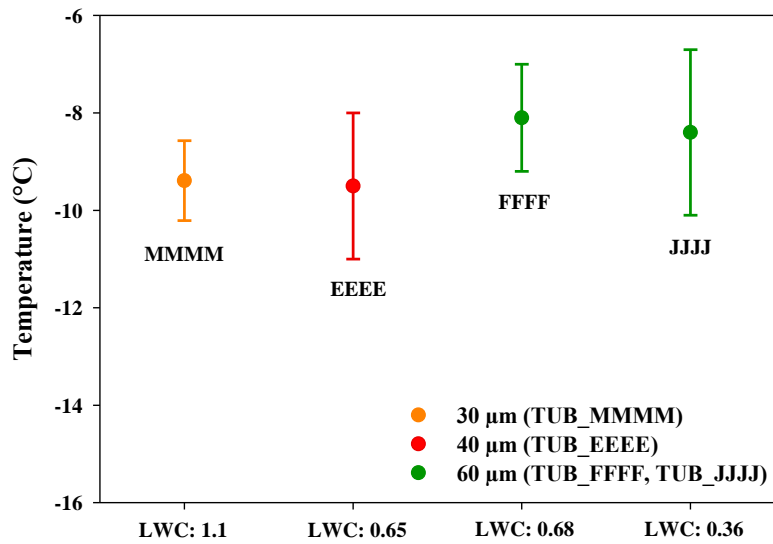


b)

Figure 36: Droplet temperature measurement at $T_{air} = -10$ °C and $V = 40$ m/s a) Temporal evolution of the measured droplet temperature b) Statistical representation of the measured droplet temperature



a)



b)

Figure 37: Long duration droplet temperature measurement at $T_{air} = -10^{\circ}\text{C}$ and $V = 40\text{ m/s}$ a) Temporal evolution of the measured droplet temperature b) Statistical representation of the measured droplet temperature

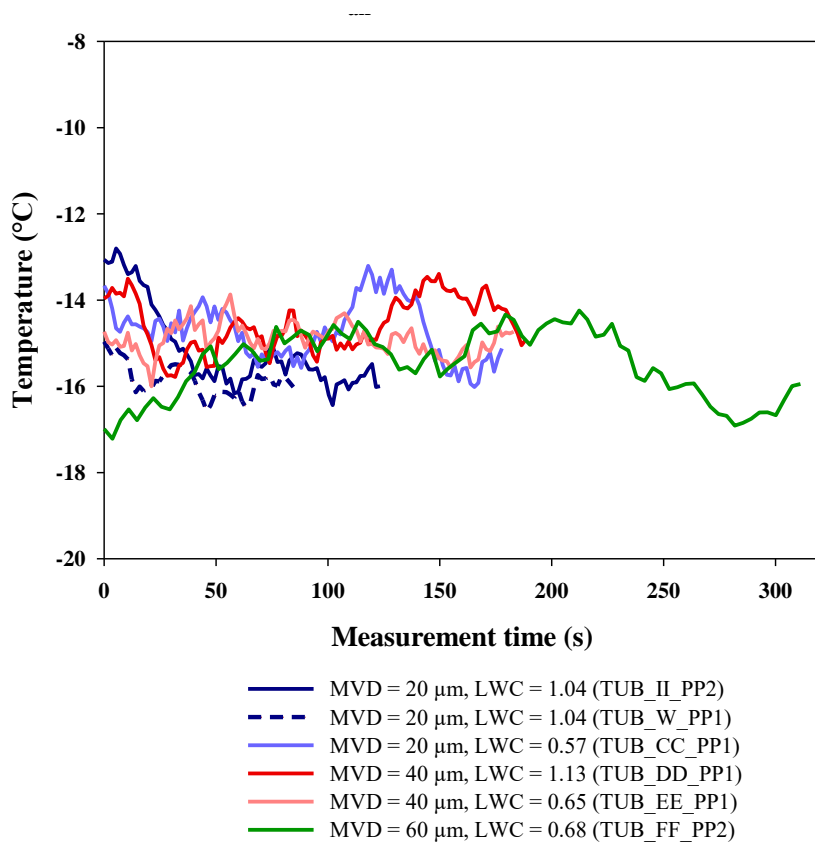
Name	V (m/s)	MVD (μm)	LWC	Exposure time (s)	Number of images	T _{measured} (°C)	MVD _{measured} (μm)
Experimental date: 29 Oct 2019 and 1 Nov 2019							
TUB M (Neg10 D20)	40	20	1.04	1.76	74	-12.5	16.92
TUB N (Neg10 D20 LowLWC)	40	20	0.57	1.76	77	-10.7	22.89
TUB MMMM (Neg10 D30)	40	30	1.10	2.54	122	-9.39	34.83
TUB DDDD (Neg10 D40)	40	40	1.13	1.76	100	-9.1	62.69
TUB O (Neg10 D40)	40	40	1.13	1.76	71	-8.6	58.71
TUB EEEE (Neg10 D40)	40	40	0.65	2.54	221	-9.5	66.67
TUB FFFF (Neg10 D60)	40	60	0.68	3.66	144	-8.1	80.6
TUB JJJJ (Neg10 D60 LowLWC)	40	60	0.36	3.66	135	-8.4	74.63

Table 4: Measurement condition at -10°C

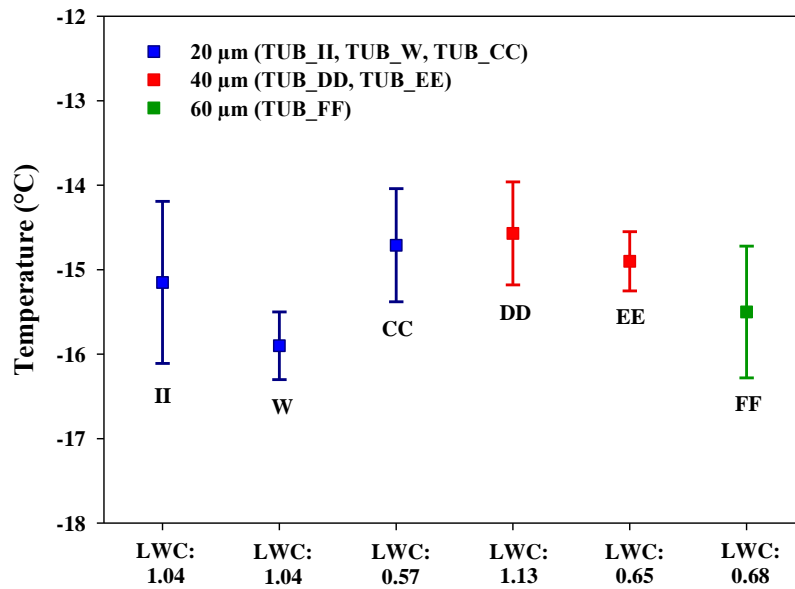
5.3.1.3 Behavior of droplet temperature for an air tunnel temperature of -15 °C

5.3.1.3.1 Droplet temperature sensitivity regarding the droplet size

Figure 38(a) displays the temporal temperature evolutions for different droplet sizes while their associated statistical behavior is displayed in Figure 38: (b) at 40 m/s. The measurements for lower velocities at 30 and 20 m/s are presented in Figure 39 and Figure 40 respectively.



a)



b)

Figure 38: Droplet temperature measurement at $T_{air} = -15^{\circ}C$ and $V = 40$ m/s a) Temporal evolution of the measured droplet temperature b) Statistical representation of the measured droplet temperature

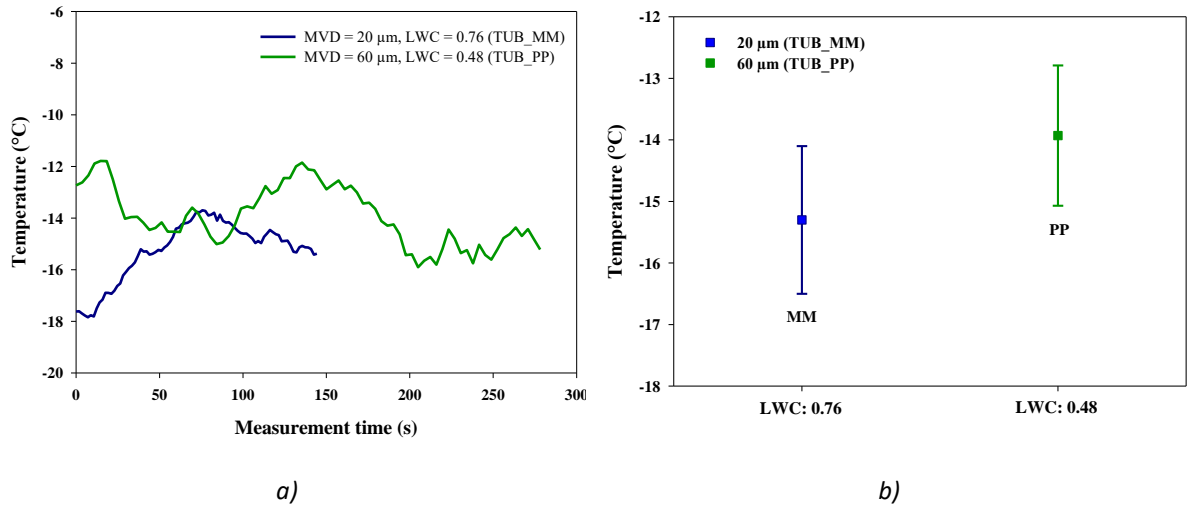


Figure 39: Droplet temperature measurements in IWT at -15°C and 30 m/s , a) Temporal temperature evolution
b) Statistical representation

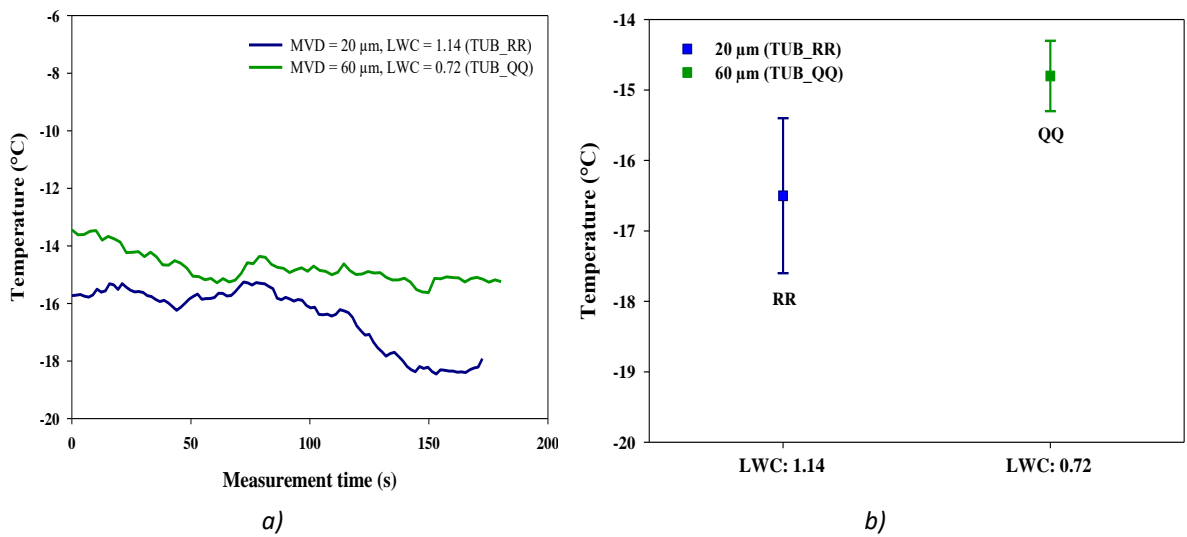
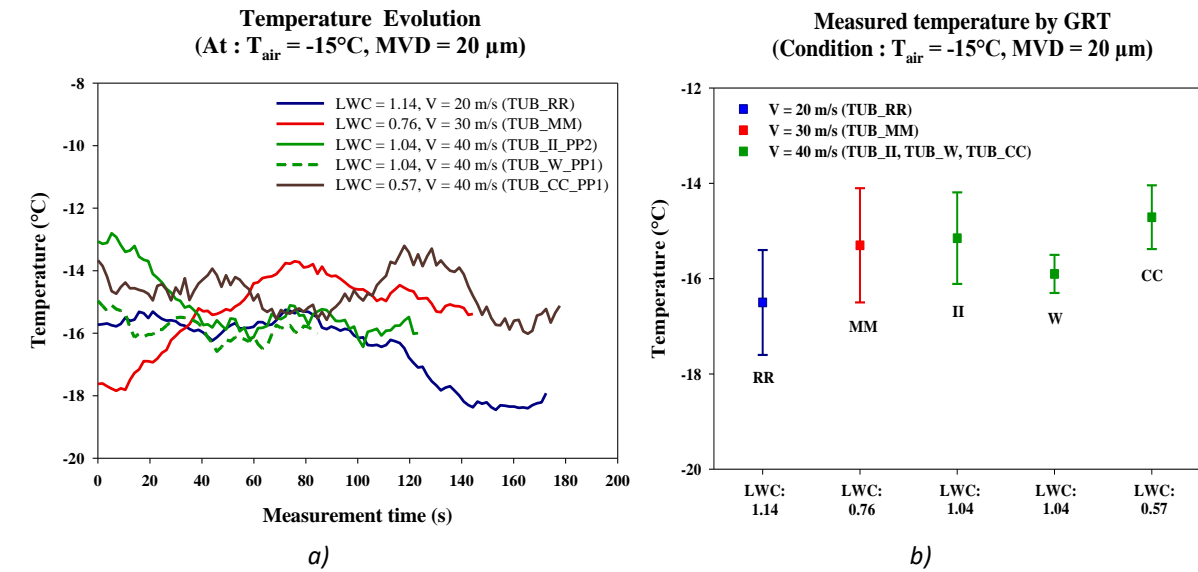


Figure 40: Droplet temperature measurement in IWT at -15°C and 20 m/s , a) Temporal temperature evolution
b) Statistical representation

5.3.1.3.2 Droplet temperature sensitivity to the air velocity

For 20 microns



For 60 microns

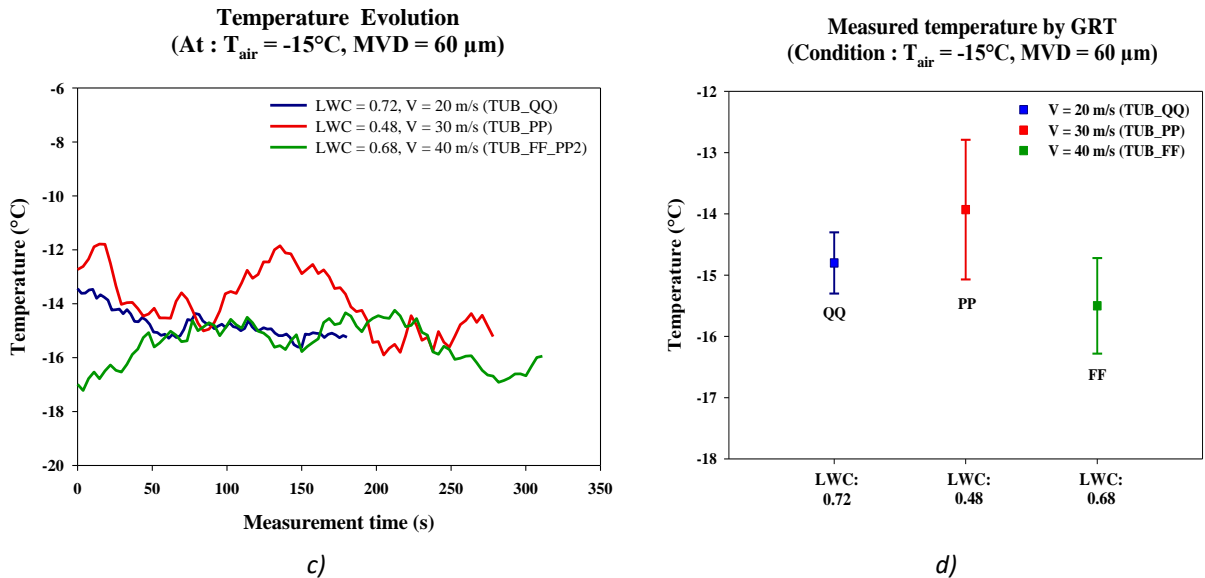


Figure 41: Droplet temperature sensitivity to the air velocity for droplet size of 20 and 60 μm a) Temporal evolution of the measured droplet temperature b) Statistical representation c) Temporal evolution of the measured droplet temperature d) Statistical representation

5.3.1.3.3 Droplet temperature sensitivity to the liquid water content

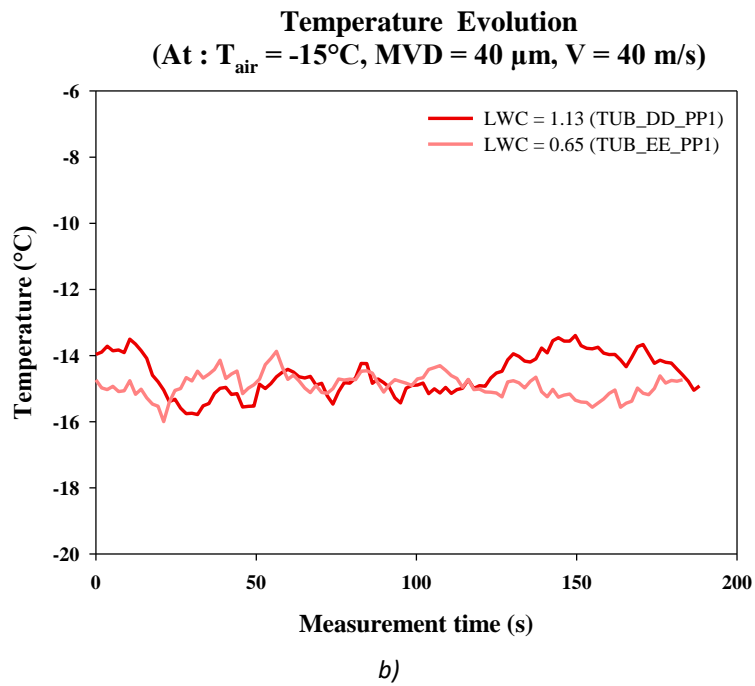
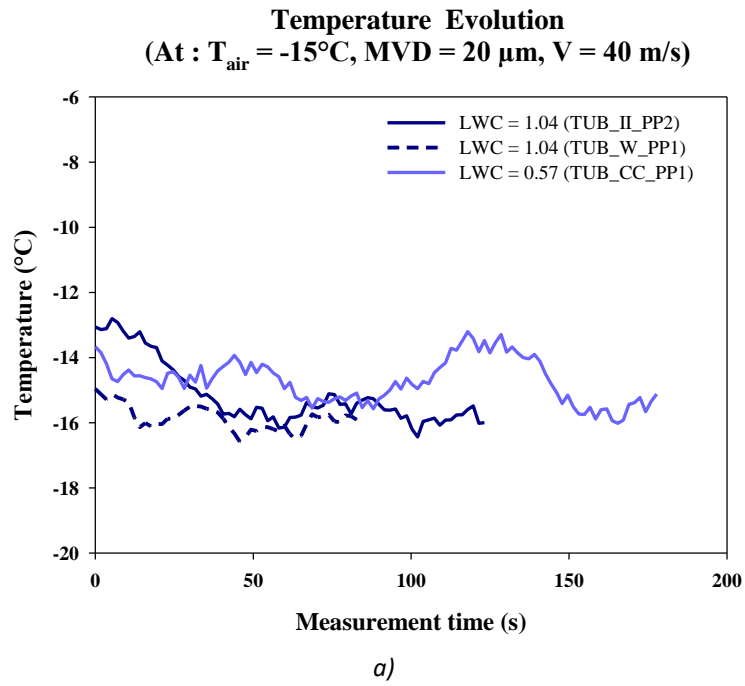


Figure 42: Droplet temperature sensitivity to the liquid water content (LWC) for droplet size of 20 and 40 μm at air velocity 40 m/s a) For 20 microns b) For 40 microns

This series of measurement have been carried out the 30 October 2019.

Name	V (m/s)	MVD (μm)	LWC	Exposure time (s)	Number of images	T _{measured} (°C)	MVD _{measured} (μm)
Experimental date: 29 Oct and 30 Oct 2019							
TUB RR (Neg15 D20 V20)	20	20	1.14	1.76	98	-16.5	24.88
TUB QQ (Neg15 D60 V20)	20	60	0.72	2.54	71	-14.8	52.74
TUB MM (Neg15 D20 V30)	30	20	0.76	1.76	82	-15.3	24.88
TUB PP (Neg15 D60 V30)	30	60	0.48	3.66	76	-13.93	58.71
TUB II (Neg15 D20)	40	20	1.04	1.76	70	-15.15	16.92
TUB W (Neg15 D20)	40	20	1.04	1.76	48	-15.9	24.88
TUB CC (Neg15 D20 LowLWC)	40	20	0.57	1.76	101	-14.71	16.92
TUB DD (Neg15 D40)	40	40	1.13	1.76	107	-14.57	52.74
TUB EE (Neg15 D40 LowLWC)	40	40	0.65	1.76	104	-14.9	54.73
TUB FF (Neg15 D60)	40	60	0.68	3.66	85	-15.5	66.67

Table 5: Measurement condition at -15°C

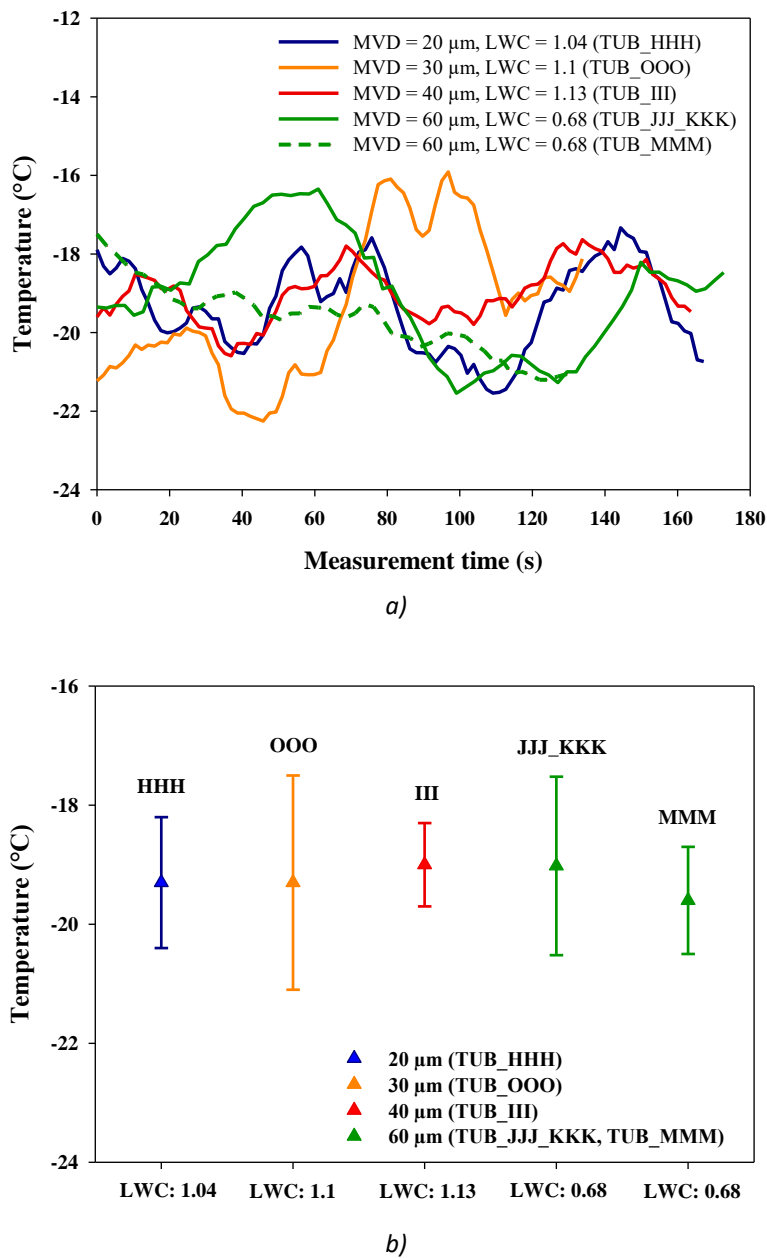
5.3.1.4 Behavior of droplet temperature for an air tunnel temperature of $-20\text{ }^{\circ}\text{C}$ 

Figure 43: Droplet temperature measurement at $T_{air} = -20\text{ }^{\circ}\text{C}$ and $V = 40\text{ m/s}$ a) Temporal evolution of droplet temperature at $-20\text{ }^{\circ}\text{C}$ b) Statistical representation of the measured droplet temperature at $-20\text{ }^{\circ}\text{C}$

Name	V (m/s)	MVD (μm)	LWC	Exposure time (s)	Number of images	T _{measured} (°C)	MVD _{measured} (μm)
Experimental date: 31 Oct 2019							
TUB_HHH_(Neg20_D20)	40	20	1.04	1.76	95	-19.3	22.89
TUB_OOO_(Neg20_D30)	40	30	1.10	1.76	76	-19.3	32.84
TUB_III_(Neg20_D40)	40	40	1.13	1.76	93	-19	56.72
TUB_JJ_KKK_(Neg20_D60)	40	60	0.68	2.54	68	-19.02	74.63
TUB_MMM_(Neg20_D60)	40	60	0.68	2.54	51	-19.6	78.61

Table 6: Measurement condition at -20 °C

5.3.2 Size measurement

During the measurement, the size distribution is continuously evaluated. As illustrated on Figure 44, the following information is displayed:

- The measured size distribution in number extracted from the last image displayed as a blue histogram
- The measured cumulative size distribution in number from all the previously recorded images displayed as a yellow histogram
- Gamma distribution displayed as a green curve fitting of the cumulative size distribution in number
- Gaussian distribution displayed as a red curve fitting of the cumulative size distribution in number
- The cumulative size distribution in volume displayed as a dark green-yellow curve computed from cumulative size distribution. Its intersection with the red dashed line defines the MVD

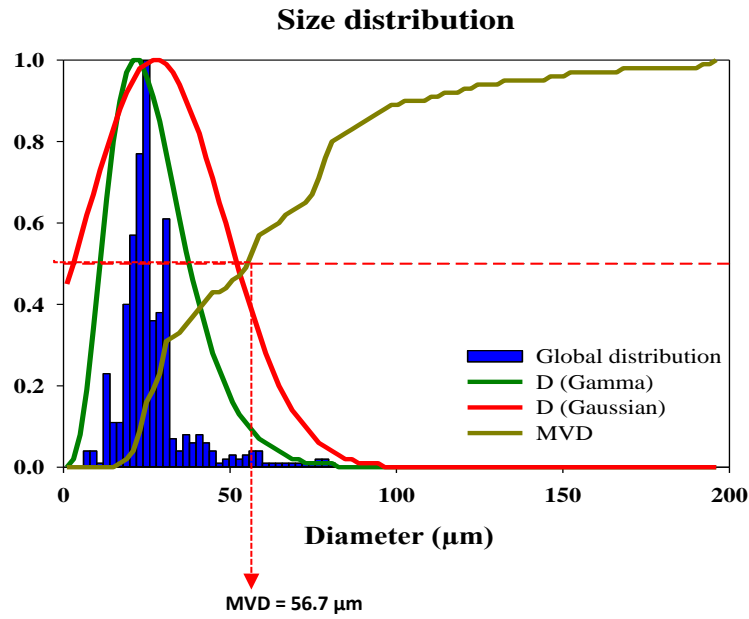


Figure 44: An example of size distribution measurement

In Figure 45, the measured MVD is plotted against the ordered diameter. A general conclusion is that the MVD is relatively well measured by using the Global Rainbow Technique (GRT), independently of Liquid Water Content (LWC), air velocity, air temperature, etc.

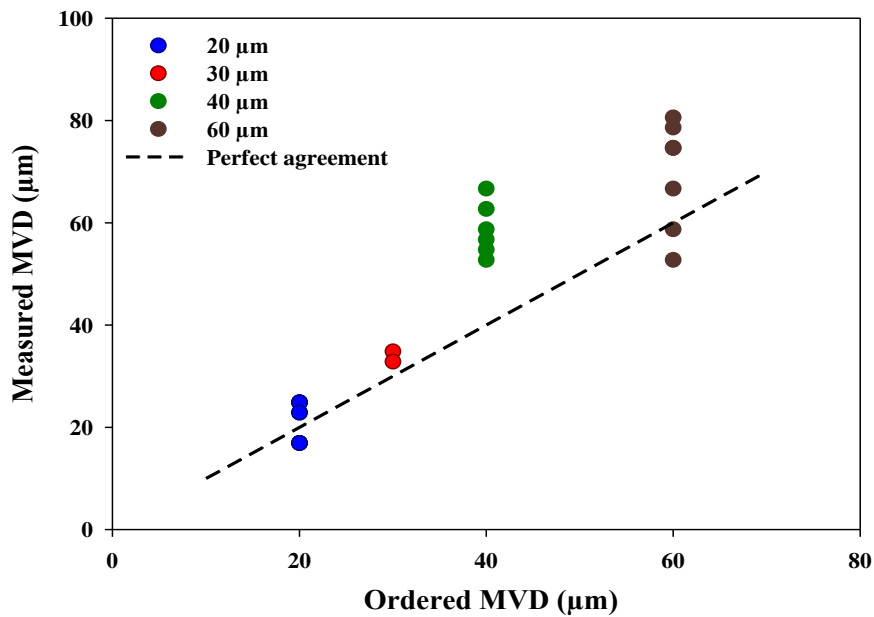


Figure 45: Measured MVD versus ordered diameter

The cumulative size distribution in volume is fitted by a multi-modal Rosin-Rammler distribution (up to three modes), permitting to improve the quantity of information extracted from GRT measurements.

As an example, two measurement points are selected, corresponding to (-15 °C / 19 μm) and (-9 °C / 77 μm), on the plot where the measured temperature is juxtaposed to the MVD (Figure 46 see the points with a green and a red circle).

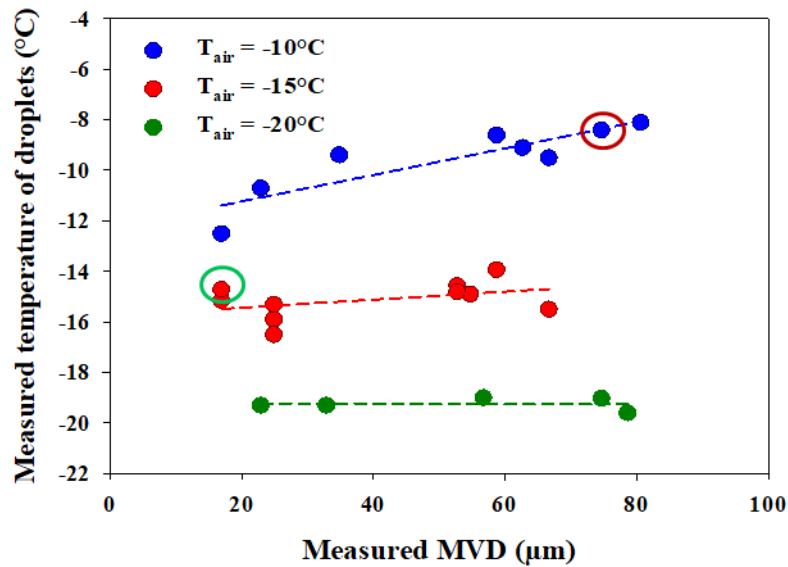
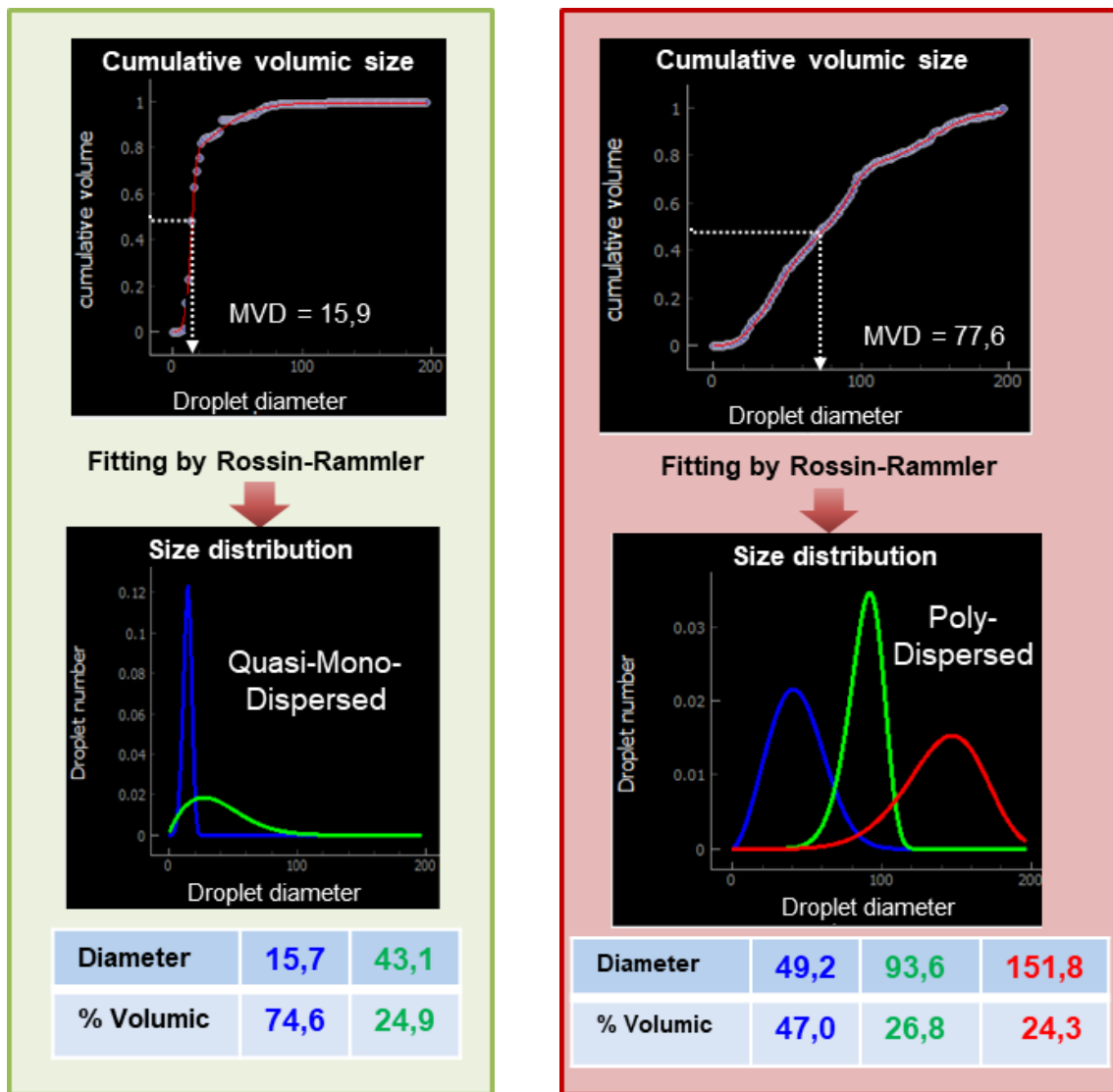


Figure 46: The measured droplet temperature versus the measured MVD

Figure 47 plots the Rosin-Rammler distribution for these two measurement points. For the point inside the green circle (-15 °C / 19 μm), the Rosin-Rammler size distribution is nearly monodispersed with a diameter of 15.7 μm. On the contrary, for the point inside the red circle (-9 °C / 77 μm), the Rosin-Rammler size distribution is not monodispersed. A strong contribution of large droplets (151 μm) can be observed. The presence of such large droplets, possibly at a higher temperature than the smallest ones, can explain the increase of the temperature (see section 5.4.6.1).



(a)

(b)

Figure 47: The Rosin-Rammler analysis of the size distribution

This example demonstrates the importance to simultaneously measure the droplet temperature and size distribution to be able to efficiently analyze the measurement results.

5.3.3 Large droplets

Figure 48 displays the measurement for large droplets. The temporal measurements are characterized by large fluctuations of temperature. However, it will be underlined that for these experimental conditions only very few droplets cross the control volume. Accordingly, the recorded rainbow signals are often issued from a single droplet. A customized signal processing strategy must be developed for such signals. Moreover, to have a good statistic, long time measurements have to be carried out.

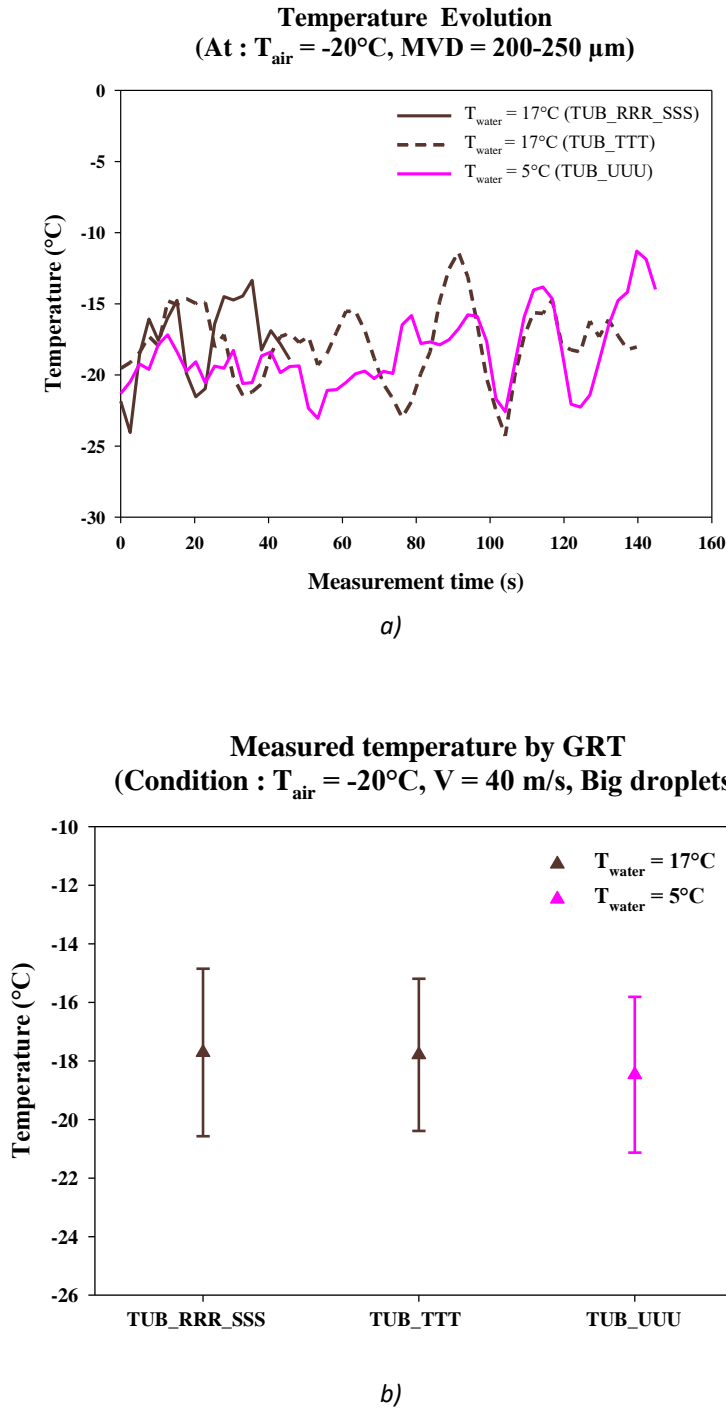


Figure 48: Droplet temperature measurement for droplet MVD larger than $100 \mu m$ a) Temporal evolution of temperature for large droplets at $-20^{\circ}C$, b) Statistical droplet temperature evolution at $-20^{\circ}C$

Name	T _{water} (°C)	V (m/s)	Exposure time (s)	Number of images	T _{measured} (°C)	MVD _{measured} (μm)
Experimental date: 31 Oct 2019						
TUB_RRR_SSS_(Neg20_BigDrop)	17	40	2.54	18	-17.71	120.4
TUB_TTT_(Neg20_BigDrop)	17	40	2.54	55	-17.79	110.45
TUB_UUU_(Neg20_BigDrop_L0degree)	5	40	2.54	57	-18.47	124.38

Table 7: Measurement conditions for large droplets (MVD > 100 μm) at -20°C

5.4 Limitation and Uncertainty of measurement in BIWT

Each IWT has its own particularities: dimensions, optical access, air velocity and temperature, spray characteristics, etc. It is therefore necessary to adapt the measurement instrument to overcome these difficulties in order to obtain accurate measurements under real IWT conditions. Such adaptations cannot be identified only by laboratory experiments. Accordingly, several test measurements can be necessary to perfectly adapt the device to the local situation.

In the case of BIWT, the deposition of an ice film inside the wind tunnel optical window impacted the measurements. A first series of measurements have been carried out with a wind tunnel air temperature equal to -10 °C. This campaign has been realized on three days: 28, 29 October 2019 and the 1 Nov. 2019. During the measurements of the 28 and 29 Oct. it has been observed that the laser beam can oscillates, as exemplified in Figure 49, strongly disturbing the measurements.

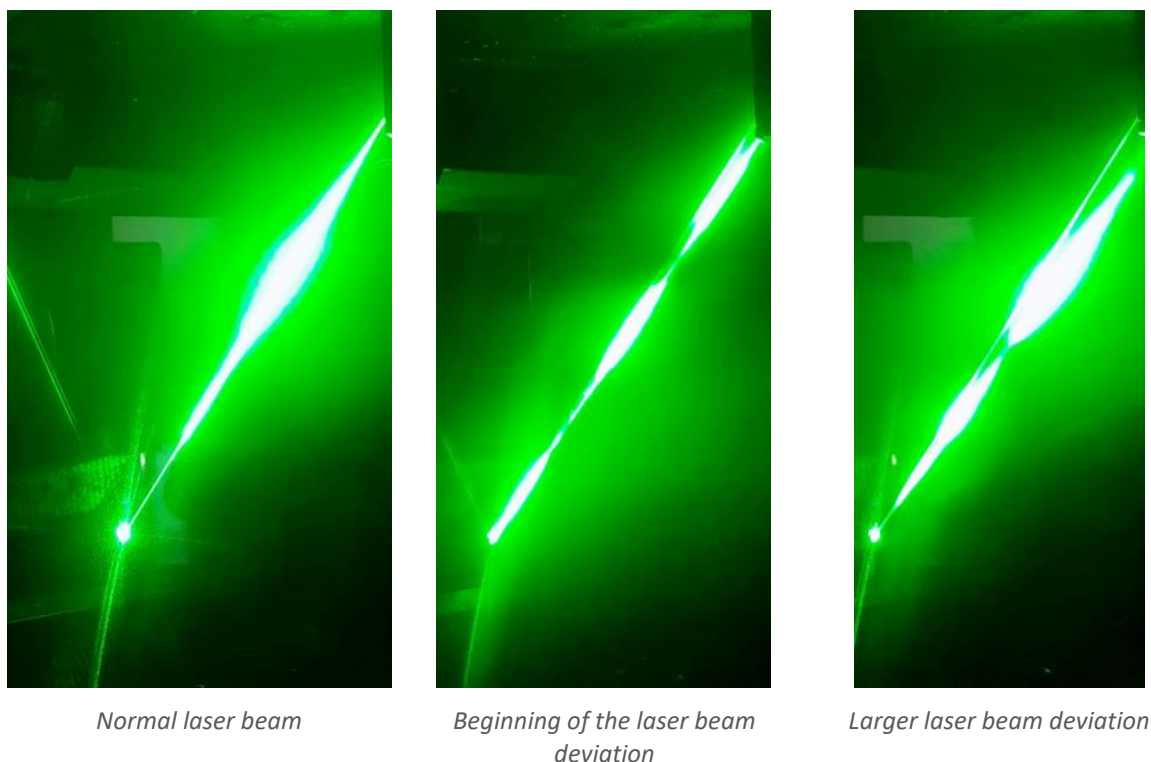


Figure 49: Series of images displaying the change of direction of the laser beam due to a water/ice film

These modifications of the laser direction create false measurements. To reduce this effect a deflection plate was setup inside the wind tunnel, improving significantly the accuracy of the measurement. Nevertheless, modification in the laser beam direction due to refraction by water/ice film, still have been accounted for.

Figure 50 displays the measurement for an air wind tunnel temperature equal to $-15\text{ }^{\circ}\text{C}$. The red curve displays the measured droplet temperature while the yellow curve displays the measured droplet size (defined as the most probable size for a Gaussian distribution). This figure underlines several critical behaviours observed during the measurement campaign:

- The droplet size (green curve) is essentially constant.
- The droplet temperature (red curve) displays strong jumps. For example, between measurements 20 and 80, the measured droplet temperatures are too high (around $+20\text{ }^{\circ}\text{C}$) which is not physically acceptable. After 70 seconds into the measurement the droplet temperature decreases to about $-15\text{ }^{\circ}\text{C}$ between measurements 90 and 210. These unphysical measurements are due to a modification of the laser direction by ice accretion inside the optical window. A strong heating (starting around measurement 70-90), focused on the location where the laser crosses the window, permits to suppress the ice deposit inside the wind tunnel, then to obtain good droplet temperature measurements after measurement 90. This solution has been used for all measurements presented in this report.
- On the contrary, the droplet size measurement is not affected by the window icing. This is because the size measurement is based on relative angular measurements while the temperature is an absolute angular measurement.

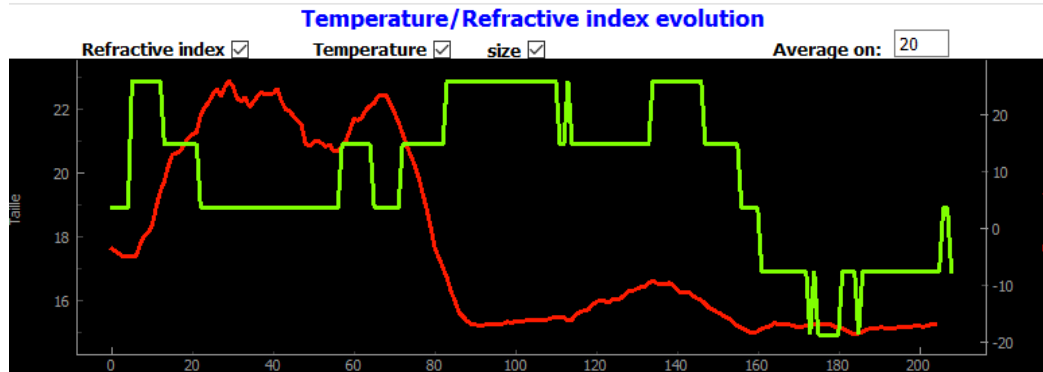


Figure 50: Examples of a measurement result perturbed by an ice deposition on the inside face of the window

5.5 Temperature Measurement in BIWT Conclusions

Pioneering measurements of droplet temperature have been successfully carried out inside the Braunschweig Icing Wind Tunnel. The results prove the capacity of the GRT to measure the average droplet temperature simultaneously with the size distribution inside a real wind tunnel.

The results show that:

- At -20 °C, measured average droplet temperature is equal to IWT temperature independently of droplet size (for MDV smaller than 60 μm)
- At -15 °C and -10 °C, measured average droplet temperature slightly depends on droplet size
- For larger droplets (MVD >100 μm), the average droplet temperature is higher than the wind tunnel temperature of about 1-2 °C, independently of the liquid injection temperature
- The size distribution can be poly-dispersed

Nevertheless, to improve the quality of the droplet temperature measurement we need to be able to prevent the deposition of water or ice on the inner side of the optical window. To reach that objective, a new accessory has been designed. Moreover, to be able to better measure the smaller droplets (MVD \leq 20 μm), the geometry of the GRT-XL must be adapted (increase the collecting angle).

The accuracy of GRT average temperature measurement has been defined at a laboratory scale to be about 1°C (for water). But the difficult environment in a real IWT at Braunschweig provides a first estimation of the GRT temperature uncertainty of about 2-3 °C.

Furthermore, the extension of GRT technique to SLD has been developed, the new inversion code has been validated by numerical simulations, laboratory experiments and preliminary tested in IWT at TUBS. The first numerical results demonstrate that very few large droplets with a different temperature have a non-negligible influence on the average temperature: complicating the result analysis. Accordingly, complementary measurement campaigns are necessary to define the statistical accuracy of GRT measurement in real Icing Wind Tunnel.

6 Droplet temperature Model

6.1 Simplified Euler-Lagrangian Model

As the liquid water content range for Appendix C and Appendix O results in an insignificant volume fraction, the droplet trajectories and temperatures are simulated using a decoupled Eulerian-Lagrangian approach. For a quick turnaround the commercially available software *ANSYS Fluent* is used. The droplet is considered to be inert (no phase change), spherical and has no internal thermal resistance.

The droplet trajectories in the presence of gravity are computed by integrating the force balance equations in the Lagrangian frame. The drag force is computed using the drag coefficient for spherical particle proposed by Morsi and Alexander [33].

The droplet exchanges heat and momentum with the continuous phase. However, in one way coupling the continuous phase properties are not altered. When the droplet temperature is below the evaporation temperature a simple heat balance equation with the convective heat transfer and radiative heat transfer is solved to obtain the droplet temperature. Radiation is not considered in the present problem, thus the last term in equation 1 is zero, thus the particle temperature can be computed if the heat transfer coefficient h is known. The convective heat transfer coefficient h is computed from the dimensionless Nusselt number correlation from Ranz and Marshall [34], equation 2, the non-zero value of Nusselt number at no-flow conditions accounts for pure diffusion at zero Reynolds number ($Nu=2.0$).

$$m_p C_p \frac{dT_p}{dt} = h A_p (T_\infty - T_p) + \varepsilon_p A_p \sigma (\theta_R^4 - T_p^4) \quad 1$$

$$Nu = \frac{h d_p}{k_\infty} = 2.0 + 0.6 Re_d^{0.5} Pr^{0.333} \quad 2$$

$$Re_d = \frac{\rho d_p |u_p - u|}{\mu} \quad 3$$

However, if the droplet is considered as being non-inert and its temperature is above the evaporation temperature and below the boiling temperature it undergoes evaporation. The evaporized mass of the droplet is computed by Ranz and Marshall [34] with an analogy between the heat and mass transfer, with the Sherwood number Sh in equation 4.

$$Sh = \frac{k_c d_p}{D_m} = 2.0 + 0.6 Re_d^{0.5} Sc^{0.333} \quad 4$$

$$N = k_c (C_s - C_\infty) \quad 5$$

The molar flux of the vapour phase N is computed from the mass transfer coefficient k_c , where C_s is the vapour concentration at the droplet surface and C_∞ is the vapor concentration in the bulk.

With the molar vapour flux of the droplet known, the instantaneous mass of the droplet as it vaporizes along its path can be computed. The temperature of the evaporizing droplet can be computed by including the latent heat transfer in equation 1.

$$m_p C_p \frac{dT_p}{dt} = h A_p (T_\infty - T_p) + \frac{dm_p}{dt} h_{fg} \quad 6$$

As the temperature of the droplet is very unlikely to exceed the boiling temperature even at low pressure conditions, droplet boiling becomes irrelevant to the present study.

6.2 Inverse Heat Conduction

In the preview of the challenges and limitations of measurement methods direct measurements except GRT are found to be not practical for sprays. Therefore, an indirect method is being developed to approximate the bulk temperature of the spray. The idea is to compute the heat transfer and

correlate it to the droplet temperature and size distribution. The impingement heat transfer can be computed inversely from the available resultant temperature evolution of the body.

Inverse heat conduction problems are ill-posed and highly sensitive to the noise in the data. Several methods are developed to deal with these challenges, a review can be found elsewhere [35] [36]. Although the predominant heat transfer is normal to plane of impingement, the randomness of the spray does not allow for reducing the problem to 1D and also to assume a functional form for the impinging heat transfer. Therefore, a 3D inverse solver is developed, its benefits can be further exploited in obtaining the heat transfer during the ice accretion. In the present study inverse heat conduction is solved using a Conjugate-Gradient (CG) method coupled with an Adjoint solver to obtain the Jacobian matrix as described in [37]. The solvers are written using the Finite Difference method and to accommodate for large time steps, the solvers are made fully implicit using Altering Direction Implicit Method.

The experiment consists of a hot plate as shown in Figure 51. The spray will impinge on the shaded surface F_1 , due to the temperature difference between the droplets and the plate heat transfer takes place predominantly normal to F_1 . The surface F_3 parallel to the impingement face exchanges heat through free convection, the other faces on the sides (F_2, F_4, F_5 and F_6) of the plate are assumed to be Neumann BCs. The plate is instrumented with 'M' high response thermocouples that measure the temperature evolution (Y_{im}) during the spray interval ($t = 0$ to t_f). The thermocouple output will be utilized to compute the resultant heat transfer on the impingement surface.

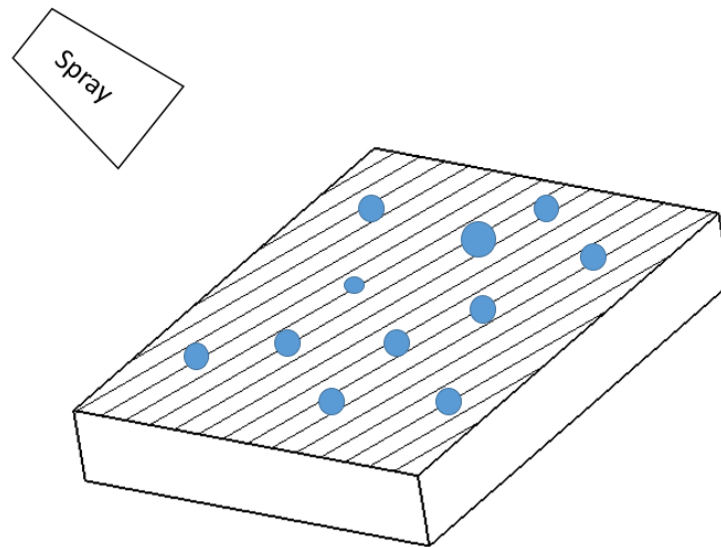


Figure 51: Schematic of setup for impingement heat transfer estimate

The heat transfer in the plate is governed by equation 7 with the associated initial and boundary conditions

$$\alpha \frac{\partial T}{\partial t} = \frac{\partial^2 T}{\partial x^2} + \frac{\partial^2 T}{\partial y^2} + \frac{\partial^2 T}{\partial z^2} \quad 8$$

$$T(x, y, z, 0) = T_0, \frac{\partial T}{\partial n_{F1}} = q_1, \frac{\partial T}{\partial n_{F3}} = h(T - T_\alpha), \frac{\partial T}{\partial n_{F2,4,5,6}} = q$$

The objective of the inverse heat conduction is to determine the unknown boundary conditions on F_1 to minimize the norm S of the measured temperatures Y_{im} and computed temperatures T_{im} (obtained by solving a direct heat transfer problem) subject to the known boundary conditions.

$$S = \sum_{i=1}^I \sum_{m=1}^M (Y_{im} - T_{im})^2 \quad 9$$

Where $i = 0$ to I are discrete sensor measurements during the measurement time $t = 0 - t_f$ and $m = 1 - M$ are the sensors. The minimisation is performed using the conjugate gradient method shown below

$$q_1^{k+1} = q_1^{k+1} - \beta^k d^k \text{ for } k = 0, 1 \dots n \quad 10$$

where β^k is the search step size and d^k is the direction.

$$d^k = \nabla S^k + \gamma^k d^{k-1} \quad 11$$

γ^k is the conjugation coefficient obtained using Fletcher and Reeves method

$$\gamma^k = \frac{\int_0^{t_f} \int_{F_1} \nabla S^{k2} dF_1 dt}{\int_0^{t_f} \int_{F_1} \nabla S^{k-12} dF_1 dt}, \gamma^0 = 0 \quad 12$$

$$\beta^n = \frac{\int_0^{t_f} \sum_{m=1}^M [T-Y] \Delta T dt}{\int_0^{t_f} \sum_{m=1}^M [\Delta T^2] dt} \quad 13$$

To obtain the gradient of the objective function ∇S an adjoint equation is formulated. ΔT is the change induced in the temperature field for a Δq change on the boundary face F_1 . To obtain ΔT a sensitivity equation (14) is solved.

$$\frac{\partial \Delta T}{\partial t} = \frac{\partial^2 \Delta T}{\partial x^2} + \frac{\partial^2 \Delta T}{\partial y^2} + \frac{\partial^2 \Delta T}{\partial z^2}$$

$$\Delta T(x, y, z, 0) = 0, \frac{\partial \Delta T}{\partial n_{F1}} = \Delta q_1, \frac{\partial \Delta T}{\partial n_{F3}} = h \Delta T, \frac{\partial \Delta T}{\partial n_{F2,4,5,6}} = 0 \quad 14$$

The objective function is minimized with the governing heat conduction equation as the constraint enforced through the Lagrangian multiplier λ .

$$S = \sum_{i=1}^I \sum_{m=1}^M (Y_{im} - T_{im})^2 + \lambda \left(\int_0^{t_f} \int_v \left(\frac{\partial^2 T}{\partial x^2} + \frac{\partial^2 T}{\partial y^2} + \frac{\partial^2 T}{\partial z^2} - \alpha \frac{\partial T}{\partial t} \right) dv dt \right) \quad 15$$

The Lagrangian multipliers are obtained by solving

$$\frac{\partial^2 \lambda}{\partial x^2} + \frac{\partial^2 \lambda}{\partial y^2} + \frac{\partial^2 \lambda}{\partial z^2} + \alpha \frac{\partial \lambda}{\partial t} + 2(T - Y) \delta \cdot (x - x_m)(y - y_m)(z - z_m) = 0$$

$$\lambda(x, y, z, t_f) = 0, \frac{\partial \lambda}{\partial n_{F1}} = 0, \frac{\partial \lambda}{\partial n_{F3}} = \frac{\lambda h}{k}, \frac{\partial \lambda}{\partial n_{F2,4,5,6}} = 0 \quad 16$$

The adjoint equation is a final value problem, with a simple transformation $\theta = t_f - t$ the adjoint equation renders the form same as the heat conduction equation and the sensitivity equation. And the directional derivative of the S with the change in Δq_1 .

$$\Delta S = \int_0^{t_f} \int_{F_1} \frac{-\lambda}{k} \Delta q_1 dF_1 dt \quad 17$$

As the directional derivative is the scalar product of the gradient and the direction of the change, the gradient of the objective function is simply the other terms in the integrand.

$$\nabla S = \frac{-\lambda}{k} \quad 18$$

Thus, the gradient of the objective function with the change in the heat flux on the impingement is obtained by solving the adjoint equation.

The inverse method can be used to get a finer resolution of the impingement heat transfer spatially and temporally. The tool will also serve as powerful means to enhance the understanding and validating the ice accretion models especially for SLD conditions.

To validate the Inverse approach, a few numerical experiments are carried out. First, a direct heat transfer is solved with some known heat flux boundary conditions, the evolution of the temperature in the model with the direct solver is recorded. A random noise is added to the recorded temperature and fed into the inverse model as an input. On successful convergence, the inverse code output should be the same as the boundary condition set in the direct model.

In the initial phase of the spray, the impingement can be considered as a case of single droplet impact on a dry surface. Then the process transforms to the impingement of droplet on a film. The heat transfer during the spreading of single droplet impact on dry surface can be determined from the expression of Roisman [38]. The total heat transfer during the impingement can be obtained by integrating equation 19 with the spreading diameter and time. However, an exact analytical integration is not possible, Schremb [39] obtained the solution (20) form that will be similar to the exact integration, the scaling factor is obtained from fitting with experimental data. Breitenbach [40] discusses the increase in complexity of heat transfer with the spray impingement on a film and remarks on the unavailability of models.

$$\dot{q}(t) = \frac{e_d e_w (T_{wo} - T_{do})}{(e_d + e_w \phi(pr)) \sqrt{\pi t}} \quad 19$$

$$Q_{spr} = \frac{2e_d e_w (T_{wo} - T_{do})}{5(e_d + e_w \phi(pr))} d_{wet,max}^2 \sqrt{t_{wet,max}} \quad 20$$

The SLD cloud in IWT has very low LWC with the probability of occurrence of droplets larger than 160 μm decreasing exponentially, thus the SLD spray does not form a droplet train on the hot plate. In addition, during the initial duration of the measurement, the spray does not form a complete film on the plate, it only results in numerous distinguishable dry impacts. Independent of the dry /wet impacts the inverse heat transfer code retrieves the resultant heat transfer map on the hot plate. Another optimizer is being developed to estimate the droplet temperature from equation 20 to match the inverse heat flux of the distinguished dry impacts.

6.3 Estimation of atomizer exit conditions with maximum entropy principle

The ice accretion on the test is highly dependent on the thermodynamic and hydrodynamic states of the spray. It can be understood from the discussion in 6 that nozzle exit conditions determine the properties of the spray as it reaches the test section, thus the outcome of icing. Especially, temperature information at the SLD nozzle is important for icing tests and subsequent numerical tools development and validation, however, this information is not available with most IWTs. The concept of maximum entropy principle is utilized in the present study to estimate the exit distribution.

The fluid injected through the atomizer exists the orifice as a jet or as thin liquid sheet. Due to the instabilities at the injection front and surroundings disturbance start to grow in the bulk fluid. The amplitude of these disturbances grows non-linearly downstream of the nozzle resulting in breaking of the sheet into multiple droplets. The atomization is a highly nonlinear process that is dependent on the mechanisms of initiation of the disturbances and the interaction between the initial disturbances which are impossible to be determined. Thus, no deterministic model could be obtained for the atomization. Several theories and correlations have been developed for spray distribution; however, they have a limited validity and can only estimate bulk quantities or moments like MVD, D_{32} etc. Estimates of the complete spray distribution in terms of size velocity and temperature are practically impossible to obtain.

In order to obtain complete probable distribution of spray from a limited information available at the atomizer inlet, Sellens and Brzustowski [41] pioneered the formalism of using Shannon’s Maximum Entropy Principle (MEP). The MEP can predict the most probable unbiased spray distribution that can result from an atomizer, the specific operating conditions are enforced as constraints in terms of continuity, momentum and energy equations.

Shannon’s expression for the information entropy of a system with ‘l’ discrete events with probabilities of P_i is given in 21

$$e \propto - \sum_{i=1}^l P_i \ln(P_i) \tag{21}$$

A system has the maximum information entropy when all constituting events are unbiased. Accordingly, the information entropy of the spray is maximum when the distribution is unbiased. Therefore, the most likely outcome of spray distribution at the exit of the atomizer is the probability density function (distribution) of size, velocity and temperature can be obtained by maximizing the entropy.

Constraints of the system

$$g(0) = \sum_{i=1}^l P_i = 1 \tag{22}$$

Equation 22, represents the normalization of the system, i.e. the sum of all the probabilities is always one. The other constraints (1 to m) are the moments of the probabilities and other physical quantities of the system expressed in 23, $\langle G_r \rangle$ are the expected values of the moments considered.

$$\sum_{i=1}^l P_i(i)g_r(i) = \langle G_r \rangle \quad r = 1,2, \dots m \tag{23}$$

To enforce the constraints defined by 22 and 23, $m + 1$ Lagrangian multipliers ($\lambda_0 - 1, \lambda_1, \lambda_2 \dots \lambda_m$) are chosen. To find the maximum entropy the first derivative of the modified entropy function is expressed in 24 is set to zero leading to 25 and 26.

$$\Delta e = - \sum_{i=1}^l P_i \ln(P_i) + (\lambda_0 - 1) \sum_{i=1}^l P_i = 1 + \sum_{r=1}^m \lambda_r \sum_{i=1}^l P_i(i)g_r(i) - \langle G_r \rangle \tag{24}$$

$$P_i = \exp (-\lambda_0 - \lambda_1 g_1(i) - \lambda_2 g_2(i) \dots \dots - \lambda_m g_m(i)) \tag{25}$$

$$\lambda_0 = \ln \sum_{i=1}^l \exp (-\lambda_0 - \lambda_1 g_1(i) - \lambda_2 g_2(i) \dots \dots - \lambda_m g_m(i))$$

The P_i in equations 26 and 23 is replaced with P_i in equation 25 and solved simultaneously using a Newton-Raphson method to obtain the Lagrangian multipliers.

The subscript i is not confined to one-dimensional solution space, it can be expanded to n dimensional space to obtain the joint probability density functions in n dimensions.

In most of the publications, MEP is applied to sprays to obtain a joint probability density function (pdf) of size and velocity. Tankin and associates [42] [43] have extended the formulation to the joint pdf in size, velocity and temperature. A few publications further resolve the velocity component to obtain 3D velocity pdf. In this work only the magnitude of the velocity is included with changes from [42] [43]. The conservation equations are formulated to conserve mass, momentum, kinetic energy, surface energy and total temperature in the control volume spanning from the atomizer exit to the plane of formation of the droplets.

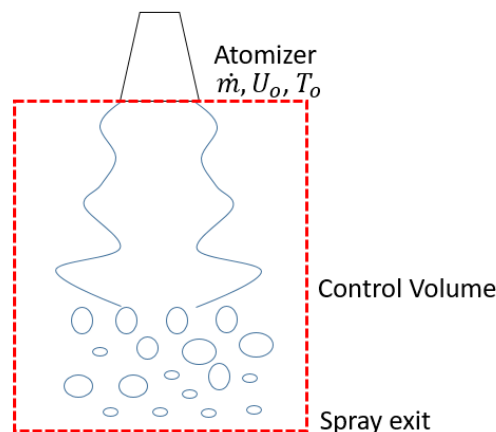


Figure 52: Schematic of control volume around the atomizer

The working fluid flows through the nozzle with a flow rate \dot{m} at temperature T_o and a velocity U_o producing N droplets at the exit of the control volume. During the transit from the exit orifice to the spray front, the jet/film sheet exchanges momentum and energy with the surroundings that should be accounted in the conservation equations. Accordingly, a discrete joint pdf P_{ijk} is assumed to represent the probability of the number of droplets at the exit plane with index i representing volume distribution for the class $d + \Delta d$, j representing velocity distribution for the class $u + \Delta u$ and k representing velocity distribution for the class $T + \Delta T$. The volume distribution spans from v_{min} to v_{max} , velocity distributions spans from 0 to u_{max} and temperature from T_{amb} to T_o . Accordingly, the conservation equations are listed below.

$$\sum_{k=T_{min}}^{T_{max}} \sum_{j=0}^{u_{max}} \sum_{i=v_{min}}^{v_{max}} P_{ijk} = 1 \quad 27$$

$$\rho_l N \sum_{k=T_{min}}^{T_{max}} \sum_{j=0}^{u_{max}} \sum_{i=v_{min}}^{v_{max}} P_{ijk} \rho_l = \dot{m} + S_m \quad 28$$

$$\rho_l N \sum_{k=T_{min}}^{T_{max}} \sum_{j=0}^{u_{max}} \sum_{i=v_{min}}^{v_{max}} P_{ijk} V_i U_j = \dot{m} U_o + S_{mu} \quad 29$$

$$N \sum_{k=T_{min}}^{T_{max}} \sum_{j=0}^{u_{max}} \sum_{i=v_{min}}^{v_{max}} P_{ijk} \left(\frac{\rho_l V_i U_j^2}{2} + \sigma A_i \right) = \frac{\dot{m} U_o^2}{2} + S_e \quad 30$$

$$\rho_l N c_p \sum_{k=T_{min}}^{T_{max}} \sum_{j=0}^{u_{max}} \sum_{i=v_{min}}^{v_{max}} P_{ijk} V_i (T_k - T_o) = S_{conv} \quad 31$$

The relative humidity inside the wind tunnel is usually over 90%, therefore mass loss due to evaporation is negligible, also condensation is also assumed to be zero, this results in no source terms for mass. The mean velocity of the jet U_o can be found from the flow rate and the orifice diameter. Air- assisted atomizer produce finer sprays from the shear breakup, the additional momentum of the air is included through the momentum source S_{mu} .

For convenience, the discrete sums are converted to continuous Riemann integral form and the equations are further normalized by the right-hand terms excluding sources. To account for the convective form of source terms in the thermal energy equation, the temperature is normalized by $(T_\infty - T_o)$.

Where the discrete probabilities P_{ijk} are represented by a pdf $f(\bar{D}, \bar{U}, \bar{T})$

$$\int_{\bar{T}} \int_{\bar{U}} \int_{\bar{D}} f d\bar{D} d\bar{U} d\bar{T} = 1 \quad 32$$

$$\int_{\bar{T}} \int_{\bar{U}} \int_{\bar{D}} f \bar{D}^3 d\bar{D} d\bar{U} d\bar{T} = 1 \quad 33$$

$$\int_{\bar{T}} \int_{\bar{U}} \int_{\bar{D}} f \bar{D}^3 \bar{U} d\bar{D} d\bar{U} d\bar{T} = 1 + \overline{s_{mu}} \quad 34$$

$$\int_{\bar{T}} \int_{\bar{U}} \int_{\bar{D}} f ((\bar{D}^3 \bar{U}^2 + B \bar{D}^2)/H) d\bar{D} d\bar{U} d\bar{T} = 1 + \overline{s_e} \quad 35$$

$$\bar{D} = \frac{D_i}{D_{30}}, \bar{U} = \frac{U_j}{U_o}, \bar{T} = \frac{T_k - T_o}{T_\infty - T_o}, B = \frac{12}{We}, We = \frac{\rho U_o^2 D_{30}}{\sigma}$$

The other terms in the integrands in the equations 32 to 35 form the constraint functions $g_r(i)$. Thus, the pdf f can be obtained in the form similar to equation 25.

$$f = 3\bar{D}^2 (\exp(-\lambda_0 - \lambda_1 g_1(i) - \lambda_2 g_2(i) - \lambda_3 g_3(i))) \quad 36$$

Solving 32 to 36 simultaneously produces most likely distribution of the spray.

Preliminary evaluation of the method has shown encouraging results. It should be noted that the above model needs information of D_{30} a priori limiting the application of the method. It is not always possible to experimentally obtain D_{30} data, therefore, improvements are being made to obtain it empirically.

6.4 Improved Euler-Lagrangian Model

The spraying system in TUBS is upgraded to produce bi-modal SLD conditions. Spray size distribution calibration is made with Phase Doppler Interferometer. The results indicated the presence of droplets larger than 400 μm . The Nusselt number for these large droplets is approximately 12.7 that results in Biot number 0.46. Due to the high Biot number there exists a considerable difference in the temperature distribution between the surface and the centre of the droplet. Therefore, the assumption of infinite thermal conductivity inside the droplet in section 6 results in inaccurate heat transfer rate and the droplet temperature, to improve the results a finite thermal conduction has to be considered.

The high deficit in velocity of the large droplets indicate the high shear on the surface droplet. The shear produces an internal circulation of fluid within the droplet. The additional bulk motion inside the droplet improves the mixing and can be considered as a mechanism enhancing the thermal conductivity. Abramzon and Sirignano [44] report that in the asymptotic limits (high Peclet Number Pe) the effective thermal conductivity between the centre and surface of the droplet is 2.72 times higher than the solid sphere. The authors arrived at an expression for increased thermal conductivity as a function of Peclet Number and modelled the complex internal circulation with simple effective thermal conductivity shown in equation 37.

$$k_{eff} = \chi k_l \quad 37$$

$$\chi = \left(1.86 + 0.86 \tanh \left(2.245 \log \frac{Pe}{30} \right) \right), Pe = 0.79 |\mathbf{v}_g - \mathbf{v}_d| \frac{\mu_g}{\mu_l} \frac{Re_d^{3/2}}{1+B_M} \frac{\rho_l R_d C_{pl}}{k_l}, Re_d = \frac{2R_d \rho_g |\mathbf{v}_g - \mathbf{v}_d|}{\mu_g}$$

Although the high relative humidity (> 90 %) inside the wind tunnel limits the rate of evaporation at the surface, any trace of it will reduce the surface temperature creating a higher gradient inside the droplet. Thus, it is essential to include the evaporation, finite thermal conduction and internal circulation inside the droplet.

Sazhin et al. [45] obtained an analytical solution for the temperature distribution inside the droplet with finite thermal conduction after neglecting smaller terms it is shown in equation 38. The instantaneous evaporation is accounted in the formalism through the effective gas temperature $T_{eff}(t)$ and the internal circulation through equation 37. Rybdylova et al. [46] modelled the same model for discrete particles in Euler-Lagrangian approach in *ANSYS Fluent* with UDF, this work meets all the requirements of the present task therefore it will be adopted in the future calculations.

$$T(r, t) = \frac{1}{r} \sum_{n=1}^{\infty} \left[\left(I_n - \frac{R_d \sin \lambda_n}{\lambda_n^2} \zeta(0) \right) \frac{e^{-\kappa \lambda_n^2 t}}{b_n} \right] \sin \left(\lambda_n \frac{r}{R_d} \right) + T_{eff}(t) \quad 38$$

λ_n are the positive roots of the equation taken in ascending order solved using the bisection method.

$$\lambda \cos \lambda + j \sin \lambda = 0$$

$$b_n = \frac{1}{2} \left(1 + \frac{j}{j^2 + \lambda_n^2} \right), I_n = \int_0^{R_d} \frac{r}{R_d} T_o(r) \sin \left(\lambda_n \frac{r}{R_d} \right) dr$$

$$\kappa = \frac{k_{eff}}{\rho_l R_d^2 C_{pl}}, \zeta(t) = \frac{h T_{eff}(t) R_d}{k_{eff}}, T_{eff} = T_g + \frac{m_d L}{2\pi R_d N u k_g}, j = \frac{h R_d}{k_{eff}} - 1, h = \frac{N u k_g}{2 R_d} \quad 39$$

The Spalding mass transfer number B_M is given by

$$B_M = \frac{Y_{vs} - Y_{v\infty}}{1 - Y_{vs}}, Y_{vs} = \frac{X_{vs} M_v}{X_{vs} M_v + (1 - X_{vs}) M_a}, X_{vs} = \frac{P_{sat}}{P}$$

$$Nu = \frac{\ln(1+B_T)}{B_T} \bar{Nu}, \bar{Nu} = 2 + \frac{(1+Re_d Pr)^{0.333} \max(1, Re_d^{0.777}) - 1}{F(B_T)}, \bar{Sh} = 2 + \frac{(1+Re_d Sc)^{0.333} \max(1, Re_d^{0.777}) - 1}{F(B_M)}$$

$$F(B_{T,M}) = (1 + B_{T,M}^{0.7}) \frac{\ln(1+B_{T,M})}{B_{T,M}}, B_T = (1 + B_M)^\Phi - 1, \Phi = \frac{c_{pv} \rho_g Diff}{k_g} \frac{\bar{Sh}}{\bar{Nu}}$$

$$Pr = \frac{c_{pg} \mu_g}{k_g}, Sc = \frac{\mu_g}{\rho_g Diff}$$

$$m_d = 2\pi R_d Diff \rho_g \ln(1 + B_M) \bar{Sh}$$

The droplet size in the Appendix O FZDZ<40, FZDZ>40, FZRA<40 and FZRA>40 can extend to 388 μm , 473 μm , 1553 μm and 2228 μm respectively. During the transit, at high Weber numbers the droplet may undergo deformations and may not follow the spherical drag law thereby influencing the velocity, temperature and the trajectory of the droplet. The degree of deformation of large droplets at high velocities has to be studied. Drag models of Haider and Levenspiel [47] or dynamic drag model of Liu et. al [48] based on Taylor Analogy Breakup (TAB) can be used for improving the trajectory and velocity computations. When the droplets deform, the surface tension causes the droplet to oscillate and the viscosity damps the oscillation. These dynamics induce a motion of fluid within the droplet producing convection that influences the temperature distribution. Dai et al. [49] studied the effect of the droplet oscillation on the heat transfer with a 3D NS solver for free surface flows for deforming droplets. Biot number has shown influence on the temperature homogeneity of the droplet, for Biot number <0.1, the inhomogeneity is minimal at higher Biot number the inhomogeneity is more pronounced for stationary droplets subjected to uniform heat transfer and deforming droplets. Sazhin's review [45] observes the influence oscillations on droplet temperature is negligible when the Weber number is less than 4.

7 Result

7.1 Simplified Eulerian Lagrangian Model Results

A Euler-Lagrangian approach is used to compute the droplet trajectories and the corresponding temperature for different tunnel velocities, droplet injection velocities, droplet injection temperatures and spray bar positions.

To determine the largest droplet distribution that can be attained without a significant deficit in droplet temperatures and velocities, droplet sizes from 20 μm to 360 μm are studied for the tunnel velocities 10 m/s to 40 m/s.

For the maximum tunnel velocity of 40 m/s the droplet injection velocity is found to have a negligible influence on the droplet velocity as they enter the test section as shown in Figure 53. As expected, the inertial influence of the large droplets is found to be carried further downstream than with the small droplets. The droplet velocity slip (relative velocity) is more pronounced above 160 μm , the slip for 160 μm and 360 μm is 10% and 22% respectively. For large particles, reduction in injection velocities have shown improvements in the droplet temperatures.

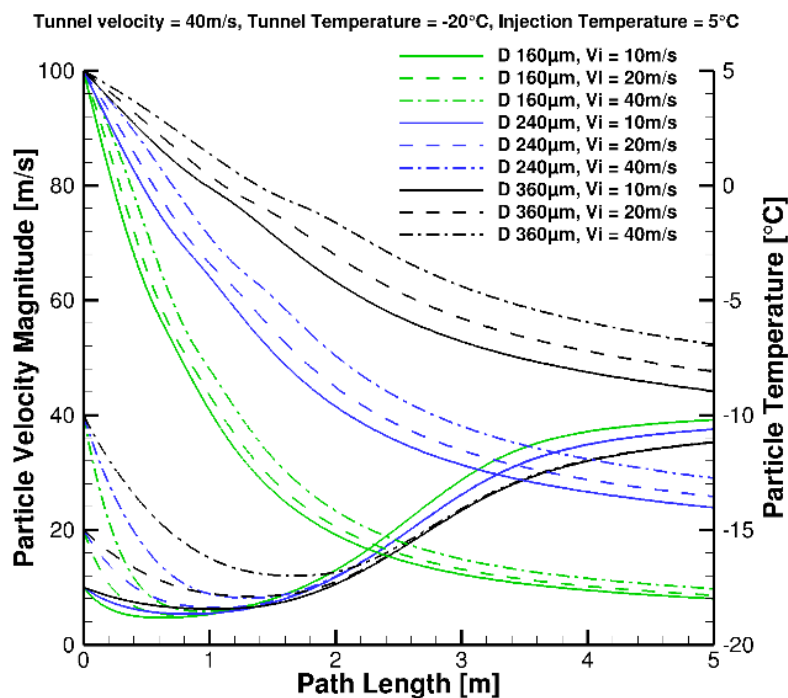


Figure 53: Influence of droplet injection velocity

Droplet temperature distribution evolution from the spray bar exit until the test section is shown in Figure 53. For the range of injection temperatures, droplets smaller than 100 μm could attain the tunnel temperature. However, as the droplet diameter increases the convective heat transfer in the short residence time in the tunnel is not adequate to cool the droplet to the tunnel temperature. A 360 μm droplet injected at 40m/s, 10 °C into the tunnel operating at 40m/s and -20 °C could be cooled only to -2°C, this signifies the need to have more accurate thermal models to predict the droplet's internal, surface and mean temperatures to improve the accuracy of the icing codes being developed for SLD conditions and also to determine the quality of the cloud that can be attained in the IWTs of the consortium. For droplets smaller than 160 μm the influence of droplet injection temperature is negligible, the influence is more pronounced with larger droplets.

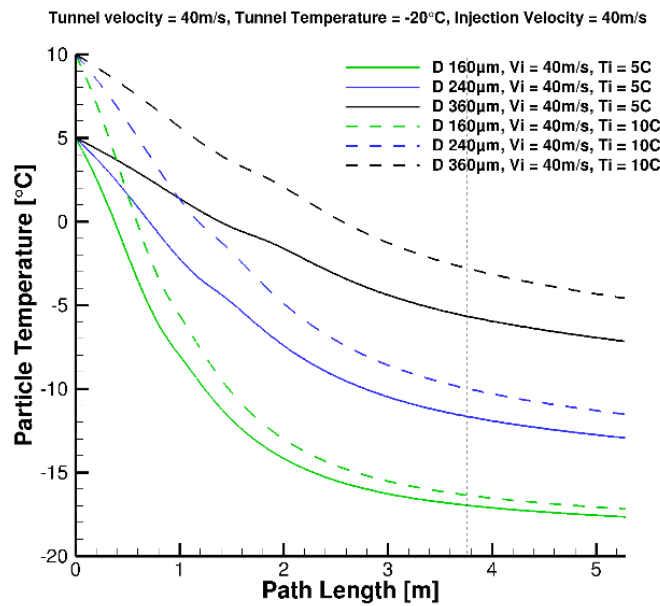


Figure 54: Droplet Temperature for tunnel conditions 40m/s at -20°C

To improve the temperature uniformity of the droplet cloud by increasing the residence time, the spray bars are shifted upstream by 0.5 m and 1 m. The improvements that can be attained with large droplets in the tunnel operating at 40 m/s, -20 °C are shown in Figure 55. The improvements in droplet temperature are accompanied by a marginal increase in the droplet slip.

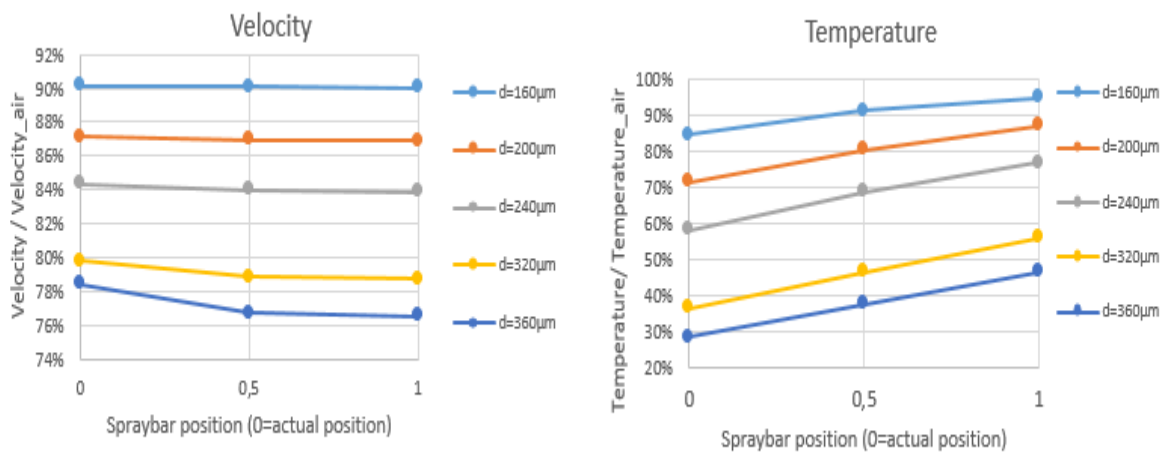


Figure 55: Improvement in droplet temperature by shifting spray bar upstream

7.2 Inverse Heat Conduction Simulated Experiments

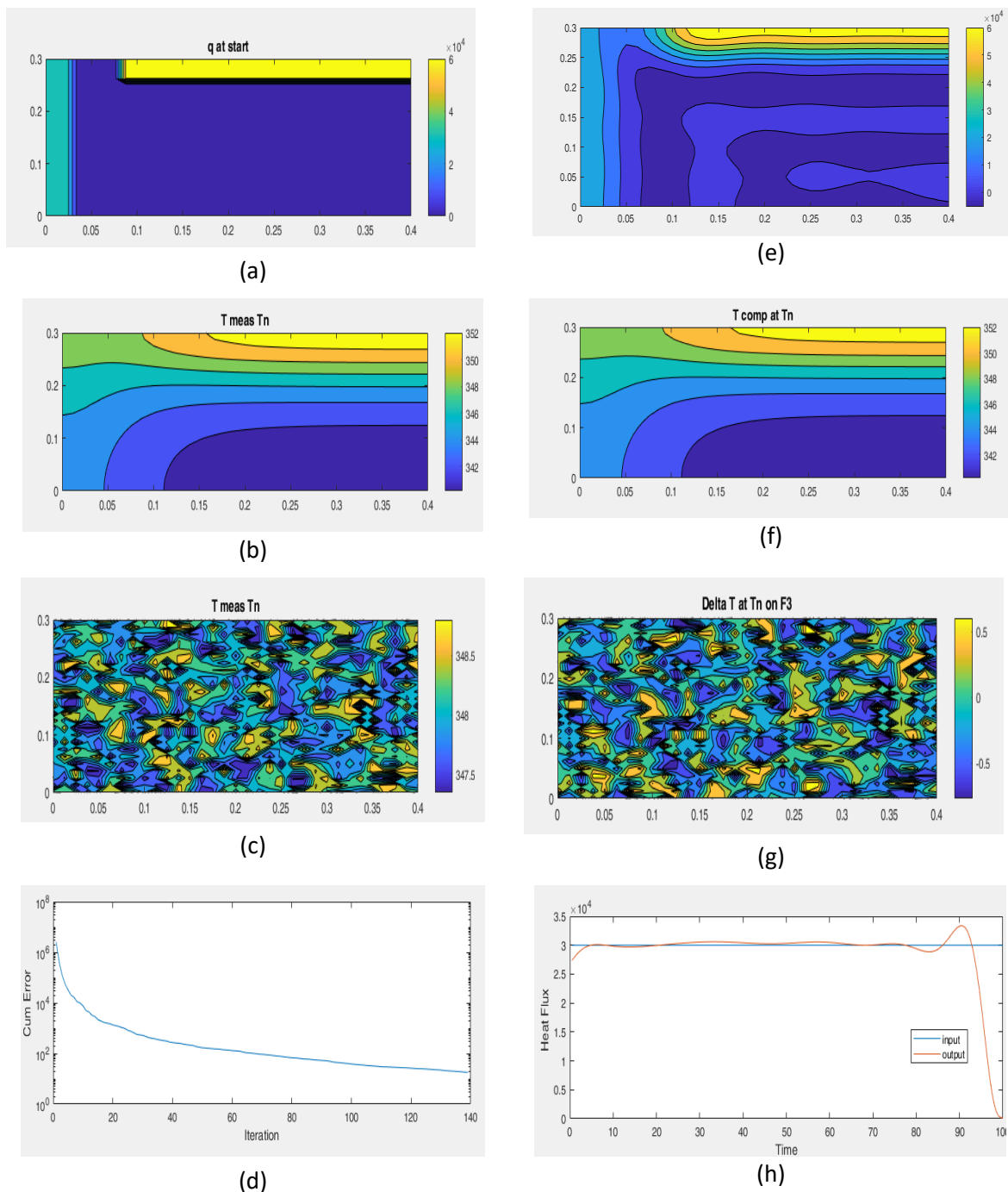


Figure 56: Inverse Heat Conduction applied to case-1

- (a) Input heat Flux, (b) Measured temperature at $t = t_f$ (c) Random noise added to measurement
 (d) Residue of IHCP (e) Inverse estimated heat flux (f) Matched temperatures (g) Delta: $T_{meas} - T_{comp}$
 (h) Temporal evolution of heat flux

Simulated experiments are carried out to check the validity of the inverse code. In the first case, spatially varying heat flux with discontinuities is imposed on face F1. In the second case, transient heat flux as step function is imposed on face F1

A heat flux as shown in (a) is imposed in a direct solver and the evolution is recorded; figure 56(b) shows the temperature on a measurement plane at $t = t_f$. Random noise is added to the measured temperature history and fed to the inverse code, the noisy measurement at t_f is shown in Figure 56

(c). Good agreement is observed between the estimated heat flux and actual heat flux. As t approaches t_f , the Lagrangian multipliers approach 0 as shown in equation 16, consequently, the heat flux estimation deteriorates as shown in (h) in the last 10 % duration of the experiments. To evaluate the performance with transient discontinuous heat flux pulses, simulations are made with arbitrary step functions. The transient performance is found to be satisfactory as shown in Figure 56. The discontinuities in the profile are not well captured due to availability of the gradients.

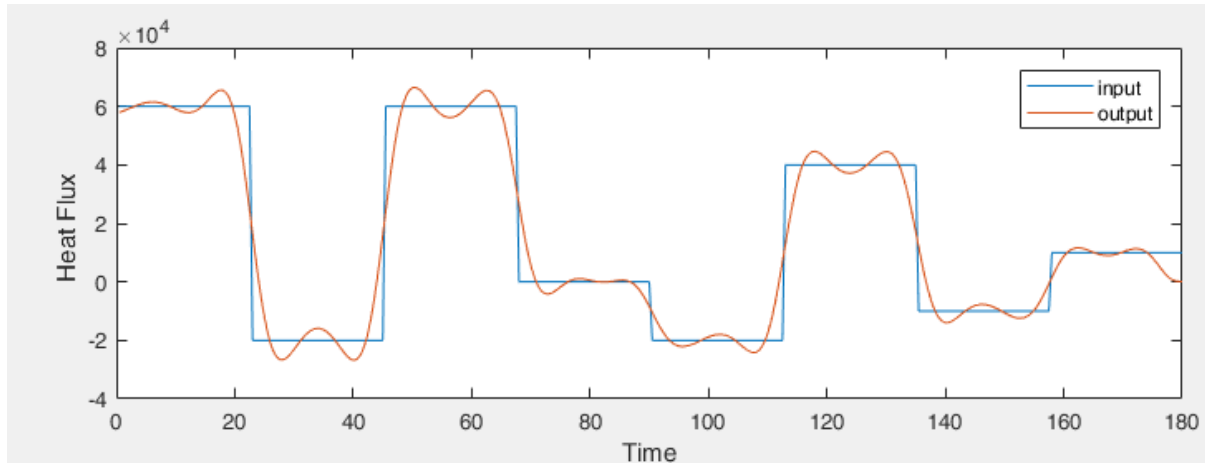


Figure 57: Heat Flux estimation with transient profiles

Simulations made with a coarse temperature measurement input in space and time have also demonstrated promising results in estimating fine resolution of the boundary conditions. With an appropriate selection of filters, the discrete events of dry impact on the surface can be identified and the resultant heat flux can be correlated to droplet temperature.

8 Temperature measurement inside large IWT (at RTA)

RainbowVision provided a GRT-Mini model to measure droplet temperature in the RTA IWT. The GRT-Mini was installed vertically inside the wind tunnel as shown in Figure 58(a). The measurement device is connected with the optical fibre and controlled from the control room at a distance of about 30 meters. A two-days measurement campaign has been carried out at RTA in November 2020. A day to set up the device inside the IWT and a day of measurement for different FZDZ conditions. Accordingly, this time constraint doesn't provide the possibility to completely solve the problem linked to the IWT environment, which are very specific to each wind tunnel.

For a MVD of 180 μm , recording has been carried out for the following conditions.

Condition 1: Air Temperature = -10 °C, Air Velocity = 40 m/s, LWC = 0.5

Condition 2: Air Temperature = -10 °C, Air Velocity = 60 m/s, LWC = 0.65

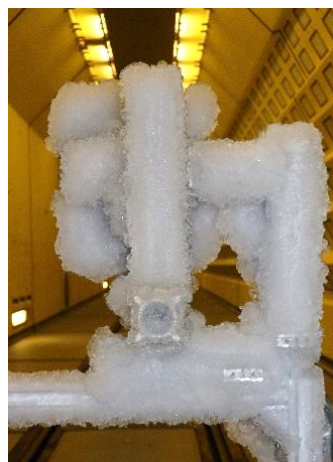
Condition 3: Air Temperature = -5 °C, Air Velocity = 40 m/s, LWC = 0.5

Condition 4: Air Temperature = -5 °C, Air Velocity = 60 m/s, LWC = 0.65

Figure 58 displays the GRT device set up at RTA, before the measurement on the first line and after the measurement on the second line. Each measurement point corresponds to a run of about 15 minutes



a)



b)

Figure 58: GRT-Mini Installation in RTA's IWT a) Before run the measurement b) After run the measurement

During this measurement campaign, the main difficulties are:

1. **Presence of droplets on the emission window.** These droplets reflect very few lights toward the CCD camera but as the exposure time must be important to collect signals from a sufficient number of droplets this effect must be suppressed
2. **Presence of fog on the collecting lens.** As exemplified in Figure 59, at the end of a measurement, fog is located on the inside of the collecting lens. The fog modified the collecting of the scattered light, gradually degrading the GRT measurement quality during a run.
3. **Contribution to GRT images from highly deformed droplets.** The largest droplets can be highly deformed by the airflow; accordingly, the rainbow is both angularly shifted and deformed. Its analysis is no longer possible in the framework of Lorenz-Mie's theory or Nussenzweig's theory, which both assume a spherical shape of the droplet, at least statistically.



Figure 59: Illustration of fog on the collecting lens

Figure 60 compiles some examples of GRT images affected by these effects.

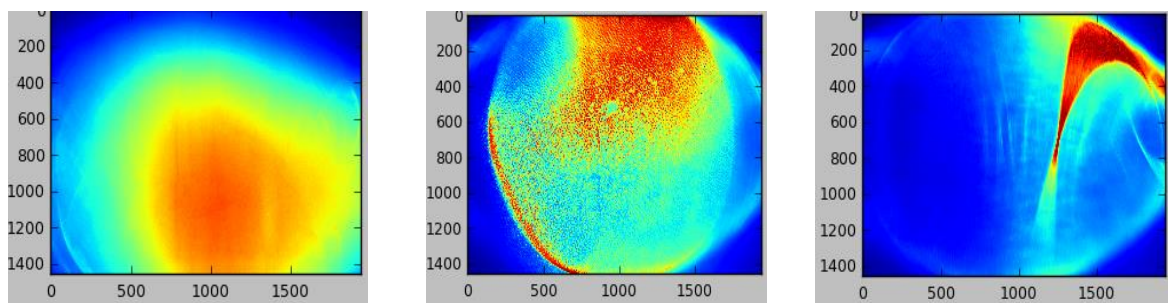


Figure 60: Examples of rejected signals at RTA a) Droplet on the emission window b) Fog on the collecting window c) Scattering diagram including at least one highly deformed droplet

To be able to record GRT images with an acceptable quality under these difficult conditions, the following extra strategies have been applied:

- The presence of droplets on the emission window has been drastically reduced by the use of a special accessory designed to blow air along the glass window. Moreover, screens have been added inside the GRT-mini device to completely suppress the light scattered from the device windows, permitting images with a very long exposure time to be recorded
- The possibility to record images with a very long exposure times, permits statistical smoothing of the effect of non-sphericity on refractive index measurement. Nevertheless, some images (as the last one in Figure 60) are rejected as being too deformed. Complementary, the possibility to sum together a series of rainbow images before carrying out the processing, increases the smoothing effect, improving the extraction of an average temperature and a size distribution.
- The effect of the fog inside the collecting lens is the most problematic. Formerly, this effect had been removed by adding heaters and fans inside the GRT mini device. Nevertheless, the working conditions was different during the last campaign at RTA. The fog formation cannot be suppressed, but only delayed. Accordingly, the fog must be removed at the end of each measurement and only the beginning of a recording can be processed.

Due to the presence of condensation on the collecting lens, a number of validated images is limited. Accordingly, we have been able to have a good statistical analysis only for the condition 4. For the three other cases, the number of validated images was too small to permit a determination of the droplet temperature.

The results corresponding to condition 4 (air temperature: $-5\text{ }^{\circ}\text{C}$, air velocity: 60 m/s , LWC: 0.65 g/m^3) are displayed in Figure 61. The average droplets temperature is measured as equal to about $-4\text{ }^{\circ}\text{C}$, while the size distribution exhibits a consequent contribution of large droplets ($170\text{ }\mu\text{m}$ and $240\text{ }\mu\text{m}$).

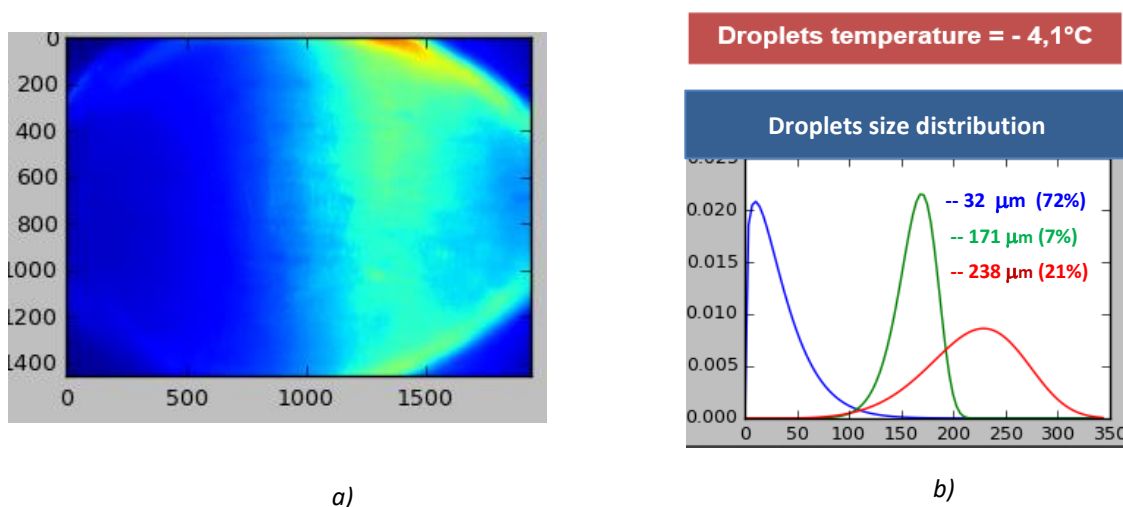


Figure 61: Example of validated measurement at RTA (for air temperature = $-5\text{ }^{\circ}\text{C}$, air velocity = 60 m/s and LWC = 0.65 g/m^3) a) Recorded image b) Associated measured size distribution and temperature

9 Temperature measurement inside large IWT (at CIRA)

In May 2022, an upgraded version of GRT-Mini has been finally tested for the first time at CIRA. The GRT-Mini was installed horizontally inside the wind tunnel as shown in Figure 62. The measurement device is connected with the optical fibre and controlled from the control room at a distance of about 30 meters. A four-days measurement campaign has been carried out at CIRA. One full day for setting up the device inside the IWT and 3 days of measurement for different conditions.



Figure 62: GRT-Mini inside CIRA facility

To validate GRT-Mini operation and adjustment, a calibration experiment has been carried out inside the CIRA IWT, by measuring the temperature and size distribution of a spray created by an ultrasonic nozzle. The temperature of the injected water was equal to the air temperature in the wind tunnel which was equal to about 15.3°C (with an air velocity equal to 0 m/s). Figure 63, is an example of recorded global rainbow signal. In this case, the measured average refractive index was equal to 1.3357 with a standard deviation equal to 0.00019 corresponding to a droplet temperature equal to ~15 °C with the standard deviation of about 2°C.

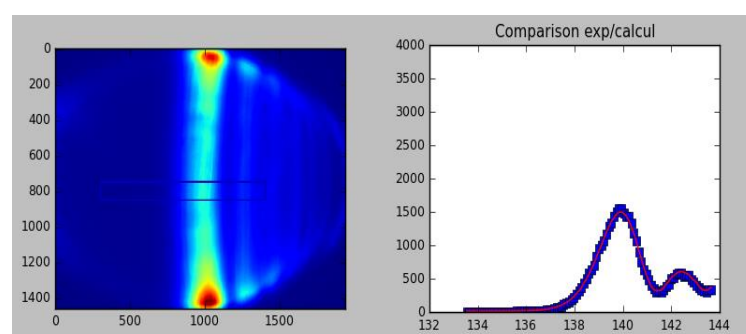


Figure 63: Example of a global rainbow image with the associated angular light distribution for a spray created by an ultrasonic nozzle.

Then, the CIRA wind tunnel was operated with an air velocity equal to 45 m/s and an air temperature equal to -18°C. To eliminate the difficulties due to the deposit of fog on the optical windows and lens encountered during RTA campaign, GRT-Mini has been modified by

- Adding new heating cables from Heatself [50] to increase the heating inside the device
- Adding new ventilators inside the device to increase the hot air flow on the optical accesses
- Adding a flow of dry N₂ to suppress the water deposition on the optical accesses

This new configuration has been successfully operated. The device works continuously inside the CIRA IWT at a temperature of -18°C during more than 6 hours, each day during three days, without fogging or icing of the windows. Figure 64 shows GRT-Mini after finish running the measurements.

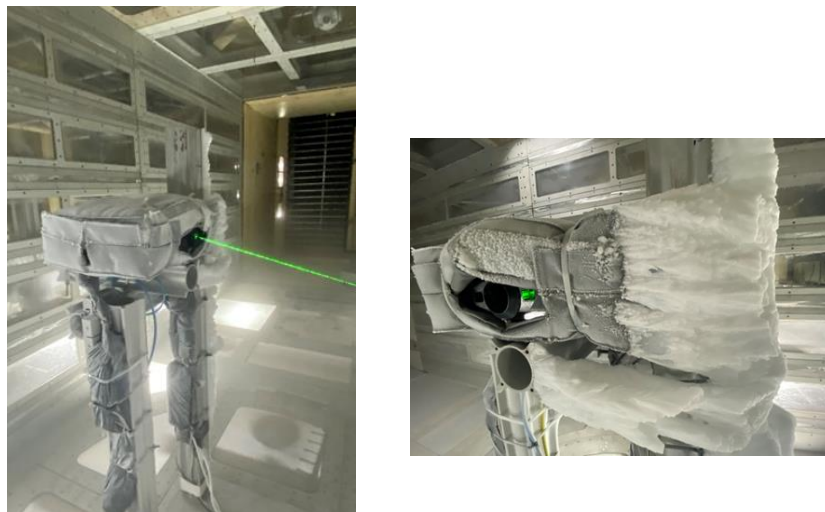


Figure 64: GRT-Mini after run the experiment

Several injection conditions have been selected by CIRA, with very low LWC, about $0.1 - 0.58 \text{ g/m}^3$ shown in table 8. Moreover, two different altitudes have been simulated, 1524 and 6000 m respectively.

A very low liquid water content (LWC) combined with large droplet size reduced dramatically the probability to have a droplet inside the optical control volume during the camera exposure time. Accordingly, it was not possible to directly record a classical global rainbow signal. Therefore, the real-time image processing software to measure the temperature of the drops cannot be directly used.

Consequently, additional steps must be added in the measurement strategy by:

1. Recording a maximum of images with a short exposure time of about 0.2-0.4 second (this exposure time was selected to maximize the probability of a large droplet being present inside the control volume and simultaneously minimize the parasitic light)
2. Selecting the recorded image where the scattered light can be assumed mainly due to a large droplet.
3. Reconstructing a global rainbow by summing these selected images
4. Processing the numerically reconstructed global rainbow as classically with our processing code based on Nussenzveig [21] [22] theory to describe the scattered light, combined with NNLS and minimisation to extract the mean refractive index.

Figure 65 presents some examples of recorded images. Not only the recorded rainbow signals from spherical droplet have been recorded but also the recorded images from deformed droplets, from noise, from the droplet outside of the control volume and etc.,

Then, the first works is to select the images from which an information can be extracted with a sufficient confidence.

Test ID	SPRAY BAR CONFIGURATION								
	Pair	$\Delta P_{\text{Pair odd}}$	P_{wat}	$\Delta P_{\text{wat odd}}$	$P_{\text{a}} - P_{\text{w}}$	$P_{\text{w}}/P_{\text{a even}}$	MVD exp (raw@60 ms ⁻¹)	LWC exp (raw@60 ms ⁻¹)	GRID- Nozzle Type
	[bar]	[bar]	[bar]	[bar]	[bar]		[μm]	[g m ⁻³]	
Altitude = 1524 m									
1	0,50		0,30		0,20	0,60	170,00	0,10	1A2_SLD#2
2	0,50		0,30		0,20	0,60	170,00	0,10	1A2_SLD#2
4	0,50		0,30		0,20	0,60	170,00	0,10	1A3_SLD#6
6	0,20		0,10		0,10	0,50	180,00	0,58	1A3_SLD#6
5	0,60		0,30		0,30	0,50	120,00	0,50	1A2_SLD#2
3	0,20		0,10		0,10	0,50	180,00	0,58	1A2_SLD#2
7	0,70	0,80	0,40	0,40	0,30	0,57	145,00	0,27	1A2_SLD#5
8	0,60		0,30		0,30	0,50	120,00	0,50	1A2_SLD#2
9	0,50	1,40	0,40	0,60	0,10	0,80	400,00	0,58	1A2_SLD#5
9(b)	0,50	1,40	0,30	0,70	0,20	0,60	400,00	0,58	1A2_SLD#5
10	0,60		0,30		0,30	0,50			1A2_SLD#3
12(b)	0,20	0,90	0,30	0,30	-0,10	1,50	450,00	0,50	1A2_SLD#5
Altitude = 6000 m									
11	0,50	0,60	0,30	0,30	0,20	0,60	130,00	0,14	1A2_SLD#5
12	0,20	0,90	0,30	0,30	-0,10	1,50	450,00	0,50	1A2_SLD#5
13	0,60	0,50	0,30	0,30	0,30	0,50	110,00	0,23	1A2_SLD#5
14	0,40	0,70	0,20	0,40	0,20	0,50	130,00	0,26	1A2_SLD#5
15	0,50	0,60	0,40	0,20	0,10	0,80	400,00	0,58	1A2_SLD#5
16	0,20	0,90	0,30	0,30	-0,10	1,50	450,00	0,50	1A2_SLD#5
17	0,70	0,40	0,40	0,20	0,30	0,57	145,00	0,27	1A2_SLD#5
18	0,50	0,60	0,40	0,20	0,10	0,80	400,00	0,58	1A2_SLD#5
19	0,20		0,10		0,10	0,50			1A2_SLD#3
20	0,70		0,40		0,30	0,57			1A2_SLD#3

Table 8: IWT working conditions with wind velocity = 45 m/s, Static Air Temperature = -18°C, Total Air Temperature = -17°C

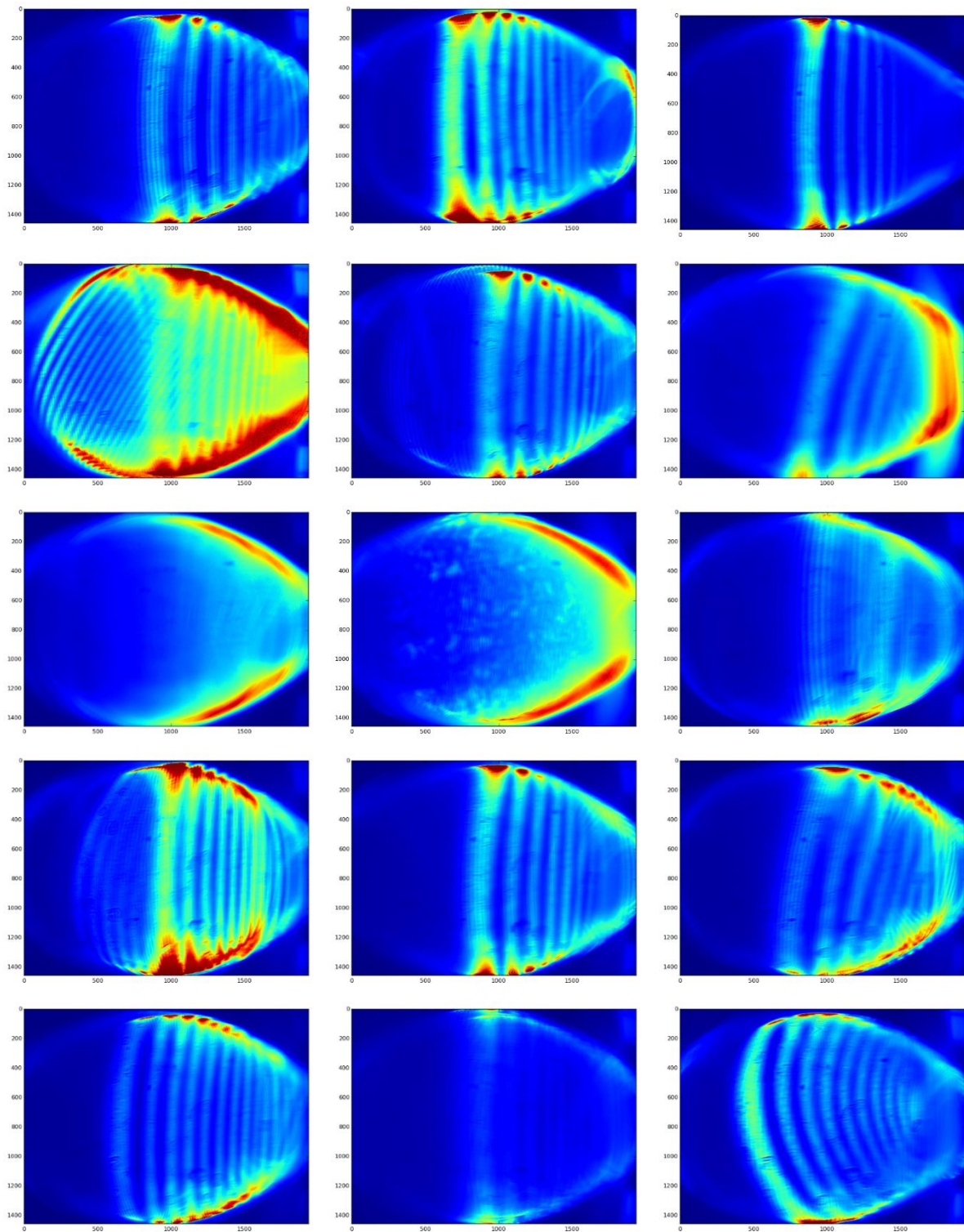
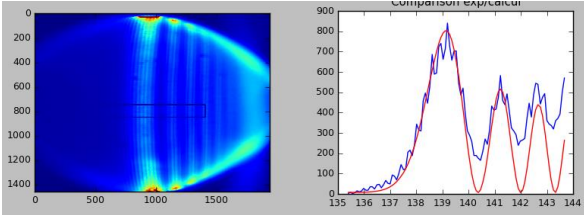
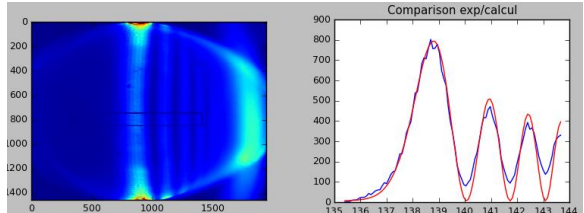
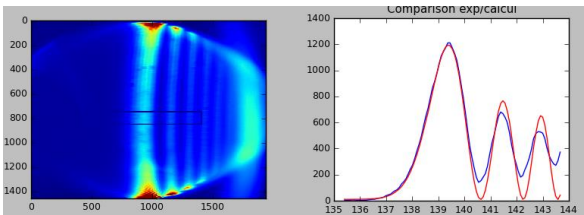
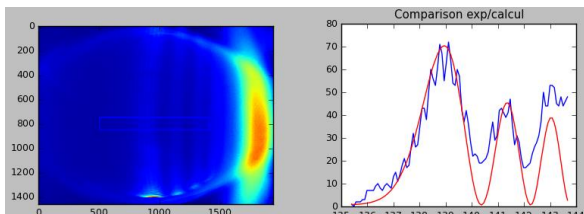
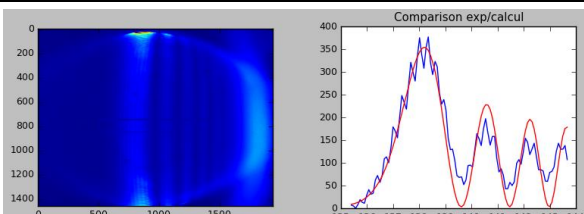
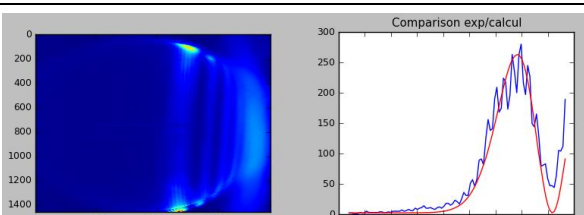


Figure 65: Examples of recorded rainbow images.

9.1 SLD size measurement:

To measure the size distribution by using these recorded rainbow images, the image selection can be based only on the presence of a rainbow shape, as the droplet size information is essentially coded by the peak angular width.

The figure 66 displays exemplifying recorded images with the associated scattering diagram and its best fit by an individual droplet (in the first column) and the associated droplet diameter (in the second column).

Rainbow image and associated rainbow signal	Extracted droplet size
	214 μm
	207 μm
	212 μm
	172 μm
	178 μm
	178 μm

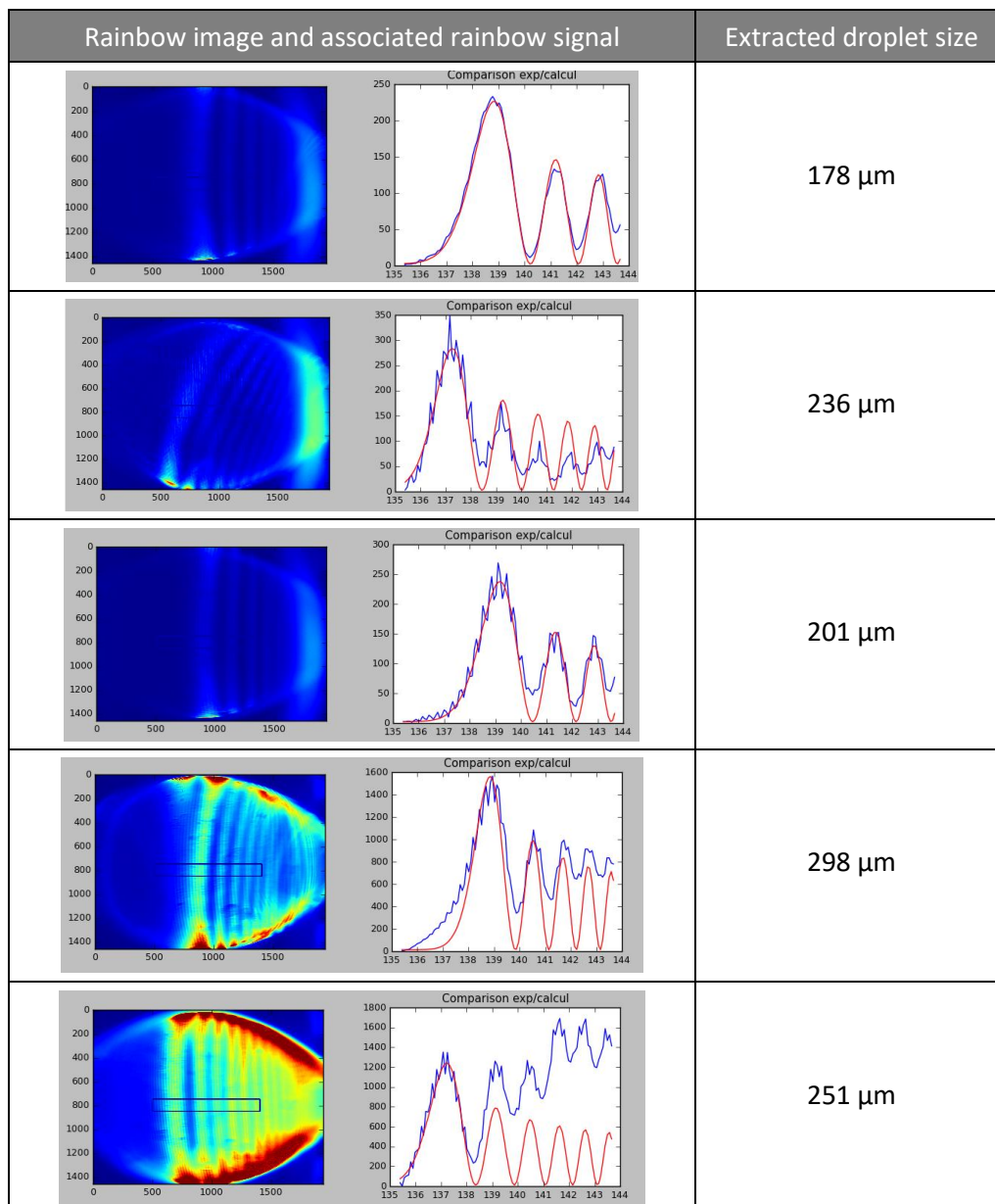


Figure 66: Some examples of images and processing to extract SLD size.

Figure 67 compiles all the measured droplet diameter from individual rainbow signal fitting for different IWT operating conditions. While, table 9 displays the mean droplet size and standard deviation extracted. The smallest measured diameter is equal to about 70 μm while the largest diameter is around 400 μm . The mean size is equal to about 200 μm . The result proved that the measurements have been done under SLD condition.

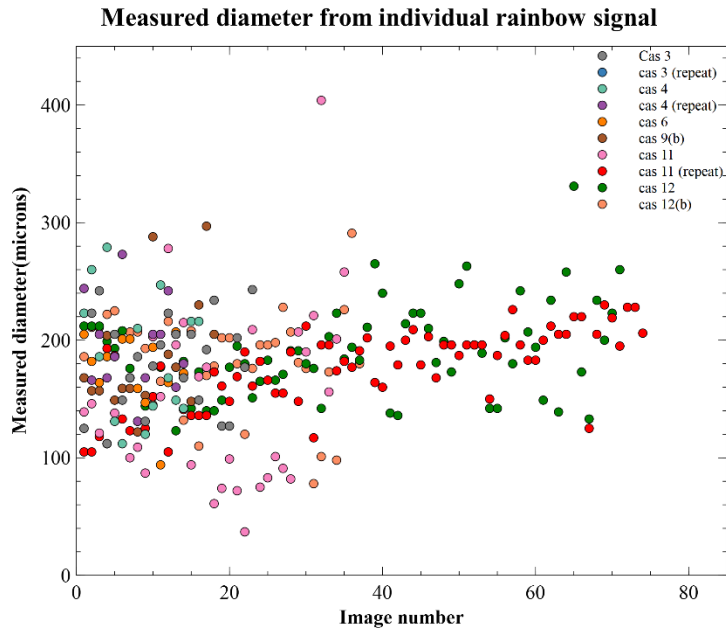


Figure 67: The measured diameter from ‘individual droplet’ versus the image number

Test ID	SPRAY BAR CONFIGURATION									GRT Measurement	
	Pair [bar]	Δ Pair odd [bar]	Pwat [bar]	Δ Pwat odd [bar]	Pa - Pw [bar]	Pw/Pa even	MVD exp (raw @60 ms-1) [μ m]	LWC exp (raw @60 ms-1) [g m-3]	GRID- Nozzle Type	Size [μ m]	STD
Altitude = 1524 m											
4	0,50		0,30		0,20	0,60	170,00	0,10	1A3_SLD#6	201	42
4 (Repeat)	0,50		0,30		0,20	0,60	170,00	0,10	1A3_SLD#6	175	30
6	0,20		0,10		0,10	0,50	180,00	0,58	1A3_SLD#6	179	41
3	0,20		0,10		0,10	0,50	180,00	0,58	1A2_SLD#2	180	45
9(b)	0,50	1,40	0,30	0,70	0,20	0,60	400,00	0,58	1A2_SLD#5	132	57
12(b)	0,20	0,90	0,30	0,30	-0,10	1,50	450,00	0,50	1A2_SLD#5	201	55
Altitude = 6000 m											
11	0,50	0,60	0,30	0,30	0,20	0,60	130,00	0,14	1A2_SLD#5	154	28
11 (Repeat)	0,50	0,60	0,30	0,30	0,20	0,60	130,00	0,14	1A2_SLD#5	173	28
12	0,20	0,90	0,30	0,30	-0,10	1,50	450,00	0,50	1A2_SLD#5	192	26

Table 9: Measured average droplet size and standard deviation

9.2 SLD temperature measurement

The droplet temperature is extracted from the absolute angular position of the rainbow signal, for spherical droplets. Any departure from sphericity affects the rainbow position, therefore droplet temperature. Accordingly, to extract the droplet temperature, a second selection of the images is necessary. Different criteria are used for this second selection (ex. the fringes inclination, the general topology of the images, etc.).

The images corresponding to these criteria are assumed to be created by spherical droplets. Nevertheless, droplets can still be affected by light shape deformation. Accordingly, only average results obtained from several droplet can be used with confidence. Then, the selected rainbow images are summed to recreate artificially a global rainbow signal from which we are able to extract an information on the average temperature of the droplets. An example of such a strategy processing is now describing, corresponding to case 11.

Figure 68 exemplifies the procedure to create a numerical global rainbow:

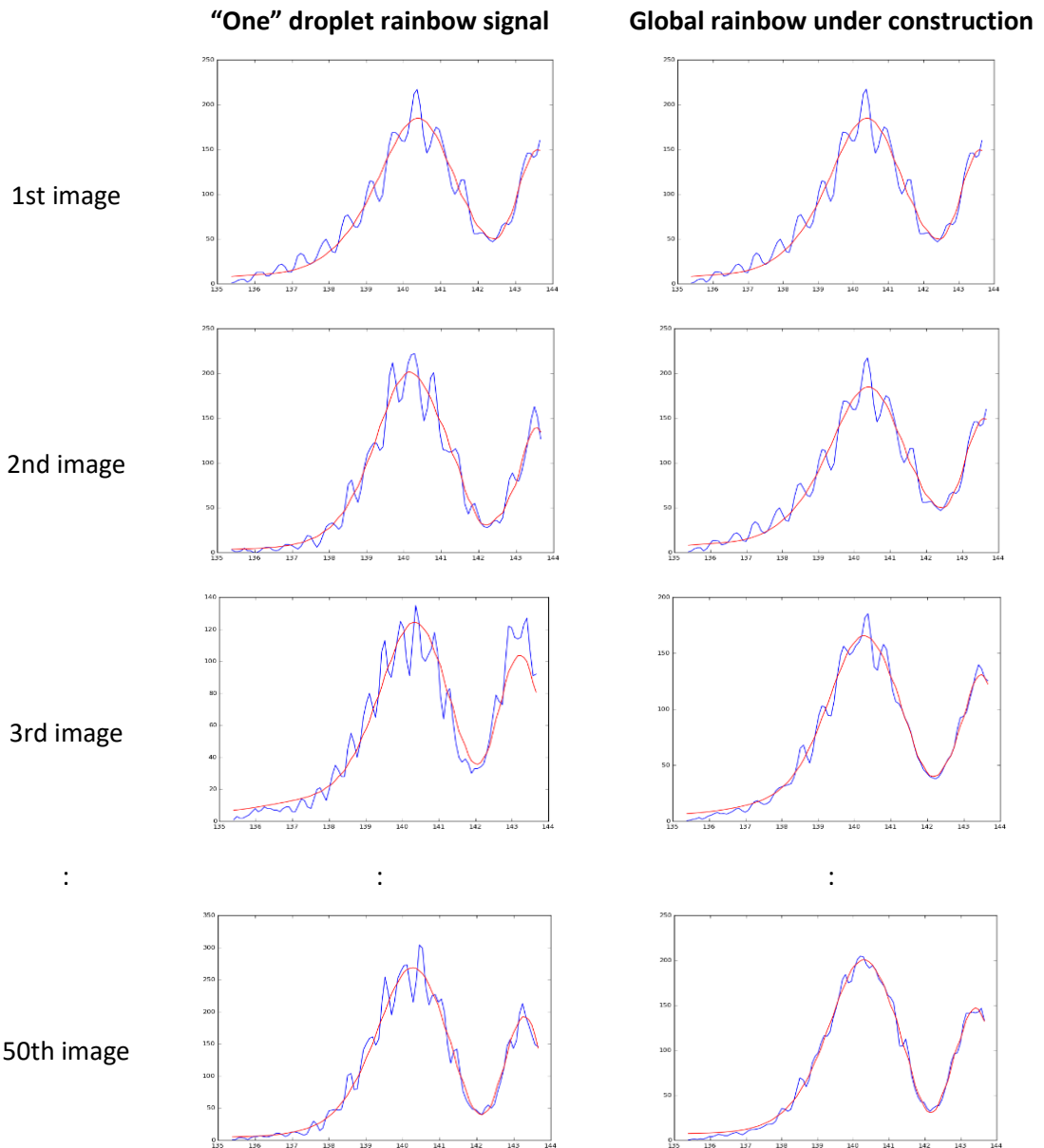


Figure 68: Visual representation of the numerical global rainbow construction from selected individual images

- The second column presents an individual droplet rainbow signal. The extracted scattering diagram is plotted in blue and its best fit computed from the measured size and refractive index values is plotted in red.
- The third column presents the reconstructed global rainbow signal. The reconstructed global rainbow signal obtained by the summation of individual from extracted scattering is plotted in blue and its best fit computed from the measured size and refractive index values is plotted in red.

The individual rainbow signal (second column) displays relatively strong variations: on the presence of ripple, on the homogeneity, on the intensity level, etc. On the contrary, for reconstructed global rainbow signal (third column), the ripple disappears. A stable signal is obtained for which the angular fluctuation of the position of the rainbow gives a background level with the appearance of a stable mean peak. An example of such a reconstructed global rainbow image is displayed in figure 69(a). Finally, the average droplet temperature can be measured.

Figure 69 compares a numerically reconstructed global rainbow from individual droplets 69(a) with a global rainbow image 69(b) recorded from an ultrasonic spray (with a large number of droplets). For the main part (in red square), these two images are very similar in shape and position proving the quality of reconstruction procedure.

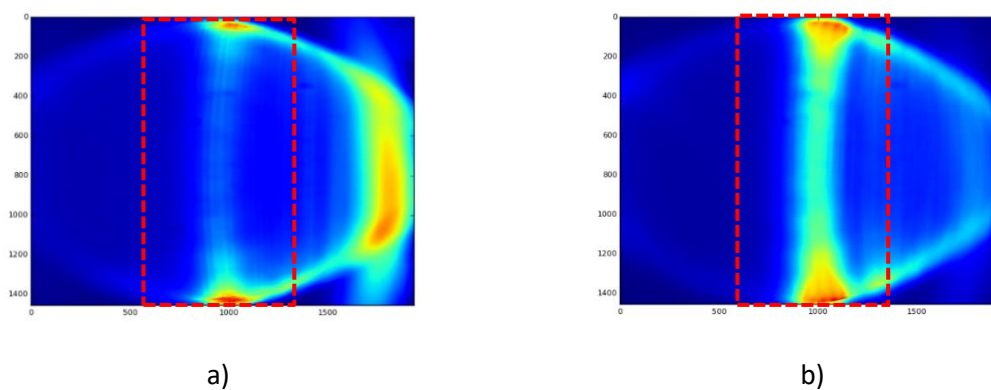


Figure 69: Comparison between the global rainbow directly obtained from a large number of droplet (left) and the numerically reconstructed global rainbow obtained from individual droplets.

Table 10 and figure 70 comply the droplet size and temperature measurements by using GRT-Mini for different spray conditions. The measurements have been carried out inside IWT with air speed equal to 45m/s with a static air temperature equal to -18°C . From the result, it seems that the droplet temperature is slightly higher than air temperature.

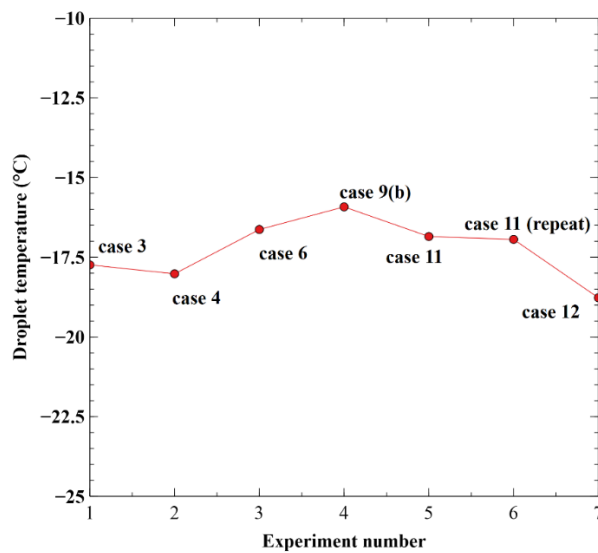
However, to be able to compare the different experiments, it is necessary to have the same large number of validated individual images for each case. Moreover, to confirm the quality of the measurements, experiments at different air temperature must be performed. Unfortunately, these measurements could not be carried out during this first campaign because the effective measurement time was too short due to:

1. the difficulty of a first installation of a GRT-Mini device in CIRA's IWT to have a stable and secure fixing
2. the adjustment of the injections system to obtain a stable spray in the wind tunnel.
3. the consequent deposition of ice on the supports modifying the trajectory of the droplets. As a result, very few droplets pass through the control volume, causing a dramatic reduction in usable images.

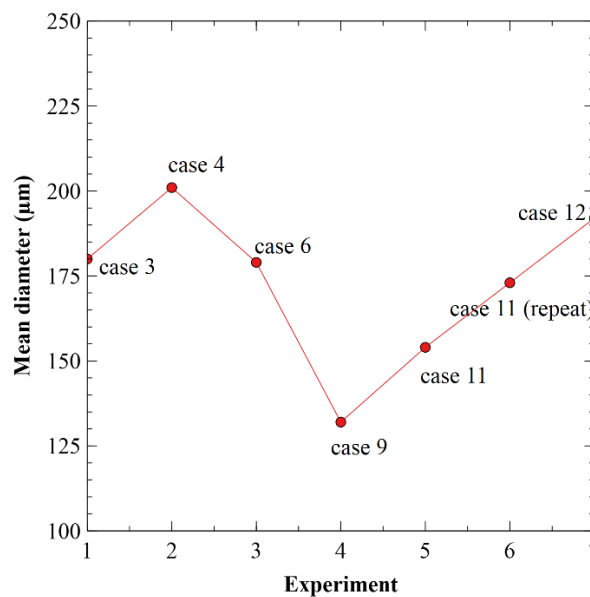
All these difficulties have been solved allowing to be optimized for a next campaign.

Test ID	SPRAY BAR CONFIGURATION									GRT Measurement		
	Pair	ΔP_{Pair} odd	P_{wat}	ΔP_{wat} odd	$P_a - P_w$	P_w/P_a even	MVD exp (raw @60 ms-1)	LWC exp (raw @60 ms-1)	GRID- Nozzle Type	Size	STD	Temperature
	[bar]	[bar]	[bar]	[bar]	[bar]		[μm]	[g m-3]		[μm]		[$^{\circ}C$]
Altitude = 1524 m												
4	0,50		0,30		0,20	0,60	170,00	0,10	1A3_SLD#6	201	42	-18,02
6	0,20		0,10		0,10	0,50	180,00	0,58	1A3_SLD#6	179	41	-16,63
3	0,20		0,10		0,10	0,50	180,00	0,58	1A2_SLD#2	180	45	-17,74
9(b)	0,50	1,40	0,30	0,70	0,20	0,60	400,00	0,58	1A2_SLD#5	132	57	-15,92
12(b)	0,20	0,90	0,30	0,30	-0,10	1,50	450,00	0,50	1A2_SLD#5	201	55	N/A
Altitude = 6000 m												
11	0,50	0,60	0,30	0,30	0,20	0,60	130,00	0,14	1A2_SLD#5	154	28	-16,85
11 (Repeat)	0,50	0,60	0,30	0,30	0,20	0,60	130,00	0,14	1A2_SLD#5	173	28	-16,94
12	0,20	0,90	0,30	0,30	-0,10	1,50	450,00	0,50	1A2_SLD#5	192	26	-18,77

Table 10: Measured average droplet size, standard deviation and average temperature in IWT with Air Velocity = 45m/s, Static Air Temperature = -18°C



a)



b)

Figure 70: SLD characterization by GRT: (a) Average droplet temperature and (b) Average droplet diameter

Conclusions

The global rainbow technique, initially developed to measure droplet temperature for combustion studies, has been used for the first time in Icing Wind Tunnels. To meet the IWT requirements, the measurement devices provided by *RainbowVision SAS* have been upgraded to:

- Be able to measure droplet from outside and inside IWT
- Remote control with real-time measurement
- Measure in a large LWC range 0.1 – 3 g/m³
- Measure in a large range of droplet size 20 – 300 μm
- Quantify multimodal size distribution

In IWTs where the GRT device is located outside of the IWT, pioneering measurements of droplet temperature have been successfully carried out inside the Braunschweig Icing Wind Tunnel (BIWT). The results demonstrate the capability of the GRT to measure the average droplet temperature simultaneously with the size distribution inside a real wind tunnel.

The results show that:

- At -20 °C, measured average droplet temperature is equal to IWT temperature independently of droplet size (for MDV smaller than 60 μm)
- At -15 °C and -10 °C, measured average droplet temperature depends on droplet size
- For larger droplets (MVD >100 μm), the average droplet temperature is higher than the wind tunnel temperature of about 1-2 °C, independently of the liquid injection temperature.
- The size distribution can be poly-dispersed

The accuracy of GRT average temperature measurement has been defined at laboratory scale: of about 1°C (for water). The pioneering results obtained in a real IWT at Braunschweig gives a first estimation of the GRT temperature measurement accuracy in such a difficult environment to be about 2-3 °C

Complementary, the extension of GRT technique to SLD has been developed, the new inversion code has been validated by numerical simulations, laboratory experiments and preliminary tested in IWT at TUBS. The first numerical results demonstrate that very few large droplets with a different temperature have a non-negligible influence on the average temperature: complicating the result analysis. Accordingly, complementary measurement campaigns are necessary to define the statistical accuracy of GRT measurement in real Icing Wind Tunnel.

Complementary, TU Braunschweig is developing a numerical simulation code to predict the droplet temperature behavior inside a wind tunnel. The aim is to compare the GRT measurements to the Braunschweig simulations.

In the large IWT at RTA where the GRT device must be setup inside the IWT, a two-days measurement campaign has been realized. A GRT-Mini device has been directly installed on the center axis inside IWT. Some successful measurements have been realized but the number of validated measurements is too limited to reach a sufficient statistical accuracy. The limited number of validated measurements is due to the presence of fog on the collecting lens created by condensation.

For the measurement at CIRA, the GRT-Mini has been upgraded, permitting to work inside the IWT at -18°C during several hours without fogging and icing. Accordingly, long measurement can be performed. For the first time, temperature measurements of SLD for several spray configurations have been carried out. The preliminary results show the measured droplet temperatures are slightly higher than the air wind tunnel. Nevertheless, the number of validated measurements must be increased to reach a good statistical value of the droplet temperature. Further measurements in the actual IWT are necessary to gain more confidence in the measurement results.

Bibliography

- [1] «Certification Specification and Acceptable Means of compliance for Large Aeroplane CS-25,» *European Aviation Safety Agency*.
- [2] I. Durickovic, R. Claverie, P. Bourson, M. Fontana, M. Marchetti, J. Chassot et M. Fontana, «Water-Ice phase transition probed by Raman spectroscopy,» vol. 42, n° 11408-1412, 2011.
- [3] H. Suzuki, Y. Matsuzaki, A. Muraoka et M. Tachikawa, «Raman spectroscopy of optical levitated supercooled water droplet,» *J. Chem. Phys.*, vol. 136, p. 234508, 2012.
- [4] T. Muller, G. Grunefeld et V. Beushausen, «High precision measurement of the temperature of methanol and ethanol droplets using Raman scattering,» *Appl Phys. B*, vol. 70, pp. 155-158, 2000.
- [5] G. Chen, M. M. Mazumder, R. Chang, J. Swindal et W. Acker, «Laser diagnostics for droplet characterization: application of morphology dependent resonances,» *Prog. Energy Combust. Sci.*, vol. 22, pp. 163-188, 1996.
- [6] P. Lavielle, F. Lemoine, G. Lavergne et M. Lebouche, «Evaporating and combusting droplet temperature measurement using two-color laser-induced fluorescence,» *Experiments in Fluids*, vol. 31, pp. 45-55, 2001.
- [7] A. Labergue, M. Stitti, F. Lemoine et G. Michel, «Caractérisation de gouttes surfondues par fluorescence induite par laser: température et fraction de glace,» chez *Congrès français de thermique*, Pau (France, 2017).
- [8] M. Stitti, A. Labergue, F. Lemoine, S. Leclerc et D. Stemmelen, «Temperature measurement and state determination of supercooled droplets using laser-induced fluorescence,» *Experiments in Fluids*, vol. 60, n° 14, p. 69, 2019.
- [9] L. Dombrovsky, S. Dembele et J. Wen, «An infrared scattering by evaporating droplets at the initial stage of a pool fire suppression by water sprays,» *Infrared Physics & Technology*, vol. 91, pp. 55-62, 2018.
- [10] G. Lamanna, P. Rack, Y. Khanfir, H. Fulge, S. Fasoulas, G. Grehan, S. Saengkaew, B. Weigand et J. Steelant, «Droplet sizing and infrared temperature measurement in superheated spray,» chez *Proc. 8th European symposium on Aerothermodynamics for space vehicles*, Lisbon (Portugal), 2015.
- [11] C. Richards et R. Richards, «Transient temperature measurements in convectively cooled droplets,» *Experiments in Fluids*, vol. 25, pp. 392-400, 1998.
- [12] S. Saengkaew, T. Charinpanikul, C. Laurent, Y. Biscos, G. Lavergne, G. Gouesbet et G. Grehan, «Processing of individual rainbow signal,» *Experiments in Fluids*, vol. 48, pp. 111-119, 2010.
- [13] A. Verdier, J. Santiago, A. Vandel, S. Saengkaew, G. Cabot, G. Grehan et B. Renou, «Experimental study of local flame structures and fuel droplet properties of a spray jet flame,» *Proceedings of the combustion institute*, vol. 36, pp. 2595-2602, 2017.
- [14] J. Promvongsa, P. Vallikul, B. Fungtammasan, A. Garo, G. Grehan et S. Saengkaew, «Multicomponent fuel droplet evaporation using 1D Global rainbow technique,» *Proceedings of the Combustion Institute*, vol. 2, pp. 2401-2408, 2017.

- [15] S. Saengkaew, G. Godard, J. Blaisot et G. Grehan, «Experimental analysis of global rainbow technique: sensitivity of temperature and size distribution measurement to non-spherical droplets,» *Experiments in Fluids*, vol. 47, pp. 839-848, 2009.
- [16] J. Wang, G. Grehan, Y. Han, S. Saengkaew et G. Gouesbet, «Numerical study of global rainbow technique: sensitivity to non-sphericity of droplets,» *Experiments in Fluids*, vol. 51, pp. 149-159, 2011.
- [17] M. Ouboukhlik, G. Godard, S. Saengkaew, M.-C. Fournier-Salaun, L. Estel et G. Grehan, «Mass transfer evolution in a reactive spray during carbon dioxide capture,» *Chemical engineering technology*, vol. 38, pp. 1-12, 2015.
- [18] M. Ouboukhlik, S. Saengkaew, M. Fournier-Salaun, L. Estel et G. Grehan, «Local measurement of mass transfer in a reactive spray for CO₂ capture,» *Canadian Journal of Chemical Engineering*, vol. 93, n° 12, pp. 419-426, 2015.
- [19] C. Kanjanasakul, F. Grisch, S. Saengkaew et G. Grehan, «Optical characterization of ethane droplets in the vicinity of critical pressure,» *OGST*, 2020.
- [20] J. van Beeck, D. Giannoulis, L. Zimmler et M. Riethmuller, «Global rainbow thermometry for droplet-temperature measurement,» *Optics Letters*, vol. 24, n° 123, pp. 1696-1698, 1999.
- [21] H. Nussenzveig, «High-frequency scattering by a transparent sphere. I. Direct reflection and transmission,» *Journal of mathematical physics*, pp. 82-124, 1969.
- [22] H. Nussenzveig, «High-frequency scattering by a transparent sphere. II. Theory of the rainbow and the glory,» *Journal of mathematical physics*, pp. 125-176, 1969.
- [23] J. Adam, «The mathematical physics of rainbows and glories,» *Physics Reports*, vol. 356, pp. 229-365, 2002.
- [24] S. Saengkaew, T. Charinpanikul, H. Vanisri, W. Tanthapanichakoon, L. Mess, G. Gouesbet et G. Grehan, «Rainbow refractometry: on the validity domain of Airy's and Nussenzveig's theories,» *Optics Communications*, vol. 259, pp. 7-13, 2006.
- [25] S. Saengkaew, *Study of spray heat up: on the development of global rainbow technique*, Rouen: PhD of Rouen University, 2005.
- [26] C. Letty, B. Renou, J. Reveillon, S. Saengkaew et G. Grehan, «Experimental study of droplet temperature in a two-phase heptane/air V-flame,» *Combustion and Flame*, vol. 160, pp. 1803-1811, 2013.
- [27] A. Lawson et B. Hanson, *Solving Least Squares problems*, SIAM, 1987.
- [28] *ATAGO*.
- [29] S. Saengkaew, G. Godard et G. Grehan, «Global Rainbow Technique: Temperature evolution measurements of super-cold droplets,» chez *ICLASS, 14th Triennial International Conference on Liquid Atomization and Spray Systems*, Chicago, USA, 2018.
- [30] Y. Haito, F. Xu et C. Tropea, «Spheroidal droplet measurements based on generalized rainbow patterns,» *Journal of Quantitative Spectroscopy and Radiative Transfer*, vol. 126, pp. 105-112, 2013.
- [31] Y. Haito, F. Xu et C. Tropea, «Optical caustics associated with primary rainbow of oblate droplets: simulation and application in non-sphericity measurement,» *Optics express*, vol. 22, pp. 25761-25771, 2013.

- [32] S. Bansmer, A. Baumert, S. Sattler, S. Knop, D. Leroy, A. Schwarzenboeck, T. Jurkat-Witschas, C. Voigt, H. Pervier et B. Esposito, «Design, construction and commissioning of the Braunschweig Icing Wind Tunnel,» *Atmos. Meas Tech*, vol. 11, pp. 3221-3249, 2018.
- [33] S. Alexander et A. Morsi, «An investigation of particle trajectories in two phase flow systems,» *J. Fluid Mechanics*, vol. 55, n° 102, pp. 193-208, 1972.
- [34] W. Marshall et W. Ranz, «Evaporation from drops, Part 1,» *Chemical Engineering Progress*, vol. 48, n° 13, pp. 141-146, 1952.
- [35] M. Ozisik et H. Orlande, *Inverse Heat Transfer: Fundamentals and Application*, Taylor and Francis Publications, 2000.
- [36] J. Taler et D. P., *Solving direct and inverse heat conduction problems*, Springer, 2006.
- [37] Y. Jarny et M. Ozisik, «A general optimization method using adjoint equation for solving multidimensional inverse heat conduction,» *IJHMT*, vol. 34, n° 111, pp. 2911-2919, 1991.
- [38] I. Roisman, «Fast forced liquid film spreading on a substrate: flow, heat transfer and phase transition,» *J Fluid Mech*, vol. 47, pp. 839-848, 2009.
- [39] M. Schremb, *Hydrodynamics and Thermodynamics of ice accretion through impact of supercooled large droplets: experiments, simulations and theory*, Ph. D Thesis, TU Darmstadt, 2018.
- [40] J. Breitenbach, I. Roisman et C. Tropea, «From drop impact physics to spray cooling models: a critical review,» *Experiments in Fluids*, vol. 59, n° 155, 2018.
- [41] R. Sellens et T. Brzustowski, «A simplified prediction of droplet velocity distribution in a spray,» *Combustion and Flame*, vol. 3, n° 165, pp. 273-279, 1986.
- [42] L. Chin et R. Tankin, «Theoretical prediction of droplet distribution in spray based on maximum entropy theory,» *HTD, Heat and Mass Transfer in spray, ASME*, vol. 187, 1991.
- [43] B. Hsing et R. Tankin, «Theoretical derivation of a spray system based on generalized maximum entropy principle,» chez *98-ICE-128, ICE-vol 31-1, Fall Technical conference, ASME*, 1998.
- [44] B. Abramzon et W. Sirignano, «Droplet vaporization model for spray combustion calculation,» *IJHMT*, vol. 32, n° 19, pp. 1605-1618, 1989.
- [45] S. Sazhin, «Advanced models of fuel droplet heating and evaporation,» *Energy and combustion science*, vol. 32, pp. 162-214, 2006.
- [46] O. Rybdylova, M. Qubesissi, M. Braun, C. Crua, J. Manin, L. Pickett, G. de Sercey, E. Sazhina, S. Sazhin et M. Heikal, «A model for droplet heating and its implementation into ANSYS Fluent,» *Int Communications in heat and mass transfer*, vol. 76, pp. 265-270, 2016.
- [47] A. Haider et O. Levenspiel, «Drag coefficient and terminal velocity of spherical and nonspherical particles,» *Powder technology*, pp. 63-7058, 1989.
- [48] A. Liu, D. Mather et R. Reitz, «Modelling the effects of drop drag and breakup on fuel sprays,» chez *SAE Technical paper series, 930072*, 1993.
- [49] M. Dai, J. Perot et D. Schmidt, «Heat transfer within deforming droplets,» chez *Proceedings of ASME ICED*, 2002.
- [50] Heatself, «<https://www.heatself.com/spip.php?page=home>,» [En ligne].
- [51] IAPWS, «<https://chemicals.readthedocs.io/chemicals.iapws.html>,» [En ligne].

- [52] IAPWS-exemple,
«<https://github.com/jjgomera/iapws/commit/1fb919c49af13022673f64f4614b496ec136d8ea>,»
[En ligne].
- [53] I.-c. source,
«https://iapws.readthedocs.io/en/latest/_modules/iapws/_iapws.html#_Refractive,» [En ligne].